Global Dynamics of the Earth's Magnetosphere During Northward IMF Conditions in the Era of the Heliophysics System Observatory

by

Sergio Esteban Vidal Luengo

A dissertation submitted in partial fulfillment
of the requirements for the degree of
Doctor of Philosophy
(Atmospheric, Oceanic and Space Sciences)
in The University of Michigan
2021

Doctoral Committee:

Professor Mark B. Moldwin, Chair
Professor Yue Ying Lau
Professor Michael W. Liemohn
Professor James A. Slavin
Associate Professor Shasha Zou

svidal@umich.edu
ORCID iD: 0000-0002-1756-545X

To all the astronauts and cosmonauts whose work at the edge of the world inspired me to follow this path.

ACKNOWLEDGEMENTS

This thesis could not have been completed without the support of a large number of people. I would like to express my gratitude and recognize their contribution here.

In the first place I would like to express my sincere gratitude to my advisor Professor Mark Moldwin who accepted me to work in his laboratory and gave me the opportunity to pursue scientific research as a career. Mark has guided and supported me through the challenging journey of the doctoral program. His patience and optimism have been fundamental for me to reach this point of my career. Thank you Mark.

I am deeply thankful for Professor Alberto Foppiano as my first mentor and advisor who introduced me to space physics during my undergraduate studies in geophysics at the Universidad de Concepción. I am thankful for his support and contribution to my development as a scientist in all the ways he could possibly imagine.

I also want to deeply thank Professor Marina Stepanova for her support during and after my undergraduate and all the opportunities she kindly gave me that contributed to my growth as a scientist.

I would also like to thanks Dr. Yash Sarkango, Dr. Garima Malhotra, Dr. Bea Gallardo-Lacourt, Dr. Victor Pinto, Dr. Nicholas Perlongo, Dr. Charles Bussy-Virat, Dr. Manuel Bravo, Dishi Li, Joong Hyun In, and Pía Sáez Berríos for their the friendship during this time.

Finally, but very important, I would also like to thank my mom, dad, and brother for their unconditional love, support, and constant encouragement during all the

stages of my education.

TABLE OF CONTENTS

LIST OF FIGURES

Figure

LIST OF TABLES

Table

LIST OF ABBREVIATIONS

AACGM Altitude Adjusted Corrected Geomagnetic

ACE Advanced Composition Explorer

AU Astronomical Unit

CfA Center for Astrophysics

CIR Corotating Interaction Region

CME Coronal Mass Ejection

CRRES Combined Release and Radiation Effects

DE Dynamic Explorer

DONKI Space Weather Database Of Notifications, Knowledge, Information

DPP dynamic pressure pulse

DST Disturbance Storm-Time

EMFISIS Electric and Magnetic Field Instrument Suite and Integrated Science

EMIC electromagnetic ion cyclotron

ESA European Space Agency

EUV Extreme Ultraviolet

FAC Field Aligned Current

FFT Fast Fourier Transform

FGM Fluxgate Magnetometer

FTE flux transfer event

GOES Geostationary Operational Environmental Satellite

GSE Geocentric Solar Ecliptic

GSM Geocentric Solar Magnetospheric

HOPE Helium, Oxygen, Proton, and Electron

HSO Heliophysics System Observatory

IAGA International Association of Geomagnetism and Aeronomy

ICME Interplanetary Coronal Mass Ejection

IGRF International Geomagnetic Reference Field

IMAGE Imager for Magnetopause-to-Aurora Global Exploration

IMF Interplanetary Magnetic Field

IMP-8 Interplanetary Monitoring Platform 8

ISAS Institute of Space and Astronautical Science of Japan

ISEE-1 International Sun-Earth Explorer 1

MHD magnetohydrodynamics

MIE Magnetic Impulse Event

MMS Magnetospheric Multiscale

NEZ North-East-Zenith

PSD power spectral density

Re Earth radius

RH08 Rankine-Hugoniot with 8 Equations

RH09 Rankine-Hugoniot with 9 Equations

RH10 Rankine-Hugoniot with 10 Equations

RMSD root-mean-square-deviation

RPI Radio Plasma Imager

SEM Space Environment Monitor

SI sudden impulse

SPDF Space Physics Data Facility

SSC sudden storm commencement

SYM-H Symmetric-Horizontal

TCV Traveling Convection Vortex

THEMIS Time History of Events and Macroscale Interactions during Substorms

TOF Time-Of-Flight

ULF Ultra Low Frequency

ABSTRACT

The dynamics of the Earth's magnetosphere is strongly influenced by the solar wind. Sudden changes in the solar wind such as dynamic pressure pulses or interplanetary shocks impacting the magnetosphere are ideal for the study of magnetohydrodynamics (MHD) wave energy transfer from the solar wind to the magnetosphere. In this thesis, I analyzed the magnetospheric global response to dynamic pressure pulses (DPPs) using the Heliophysics System Observatory (HSO) and ground magnetometers. During northward Interplanetary Magnetic Field (IMF) Bz conditions, the magnetosphere acts as a closed "cavity" and reacts to solar wind DPPs more simply than during southward IMF. I used solar wind data collected by Advanced Composition Explorer (ACE) and WIND together with magnetic field observations of Geotail, Cluster, Time History of Events and Macroscale Interactions during Substorms (THEMIS), Magnetospheric Multiscale (MMS), Van Allen Probes, Geostationary Operational Environmental Satellite (GOES) missions, and ground magnetometer arrays to observe the magnetosphere (dayside, nightside, inner magnetosphere, magnetotail, magnetosheath, etc.) and ionosphere response simultaneously in several local time sectors and regions. I examine the global response of each event and identify systematic behavior of the magnetosphere due to DPPs' compression, such as MHD wave propagation, sudden impulses, and Ultra Low Frequency waves (ULF) in the Pc5 range. Our results confirm statistical studies with a more limited coverage that have been performed at different sectors and/or regions of the magnetosphere. I present observations of the different signatures generated in different regions that propagate through the magnetosphere. The signature of the tailward traveling DPP is observed

to move at the same solar wind speed, and in superposition of other known magnetospheric perturbations. It is observed that the DPP also generates or increases the amplitude of Pc4-5 waves observed in the inner magnetosphere, while similar waves are observed on the ground. I also analyze the influence of the shock inclination relative to the dayside magnetosphere on the propagation of the preliminary impulse, whose travel-time from the dayside is important in magnetoseismology for the plasma density estimation on the magnetosphere. Finding that the arrival of the preliminary impulse at different latitudes depends on the relative angle between the shock and the dayside magnetosphere. The last study in this thesis consists of an analysis of the density profile of the magnetosphere using the preliminary reverse impulse observed by ground-based magnetometers and magnetic and electron density observation made by the HSO on the dayside magnetosphere.

This thesis addresses the challenges of the systematic use of the HSO to study different aspects of the global dynamics of the magnetosphere. In Chapter IV, this thesis presents the first and large sample and simultaneous spacecraft and ground observations in multiple regions and local time sectors and confirmed previous studies limited in space and time samples. In Chapter V this thesis also found that North-South inclination of shock has a measurable effect on arrival time of signals as a function of latitude similar to previous work that found importance of East-West/Local time effect. The implication is that ground-based observations can help determine in situ shock orientation methods. Chapter VI shows the first use of magnetoseismology using both in situ and ground-based observations to obtain an exact solution for the plasma mass density radial profile in the dayside magnetosphere.

CHAPTER I

Introduction

1.1 Motivation

Prior to the Space Age it was theorized that the near-Earth space environment contained plasma based on observations made at high latitudes. In the 1930s, Hannes Alfvén (1908-1995) formulated the MHD equations that governed the still unexplored at the time magnetosphere and interplanetary space environment. In the late 1950s and early 1960s space exploration allowed in situ observations of plasma in different regions of the magnetosphere and also in the solar wind. It was noted that the magnetosphere is constantly interacting with the solar wind and the IMF. Scientists observed that spacecraft orbiting in the magnetosphere suddenly changed of regimen, meaning that spacecraft were crossing from one region to another. However, using only single spacecraft observations it was impossible to determine if the crossing were the result of time or spatial variations. For this reason, statistical studies were developed using data from multiple boundary crossings made by the few spacecraft available (*Berchem and Russell*, 1982; *Howe Jr and Binsack*, 1972; *Kaymaz et al.*, 1994; *Paschmann et al.*, 1978, 1979). These studies were fundamental to understand the basic structure and dynamics of the magnetosphere during its interaction with the IMF.

In the early stages of space exploration, spacecraft were sent into space mainly

for scientific purposes. Their technology and capabilities rapidly improved and spacecraft started to be used for multiple military and civil applications. Parallel to the boom of spacecraft technology, the study of the magnetosphere became an important field, necessary to keep the spacecraft in operation for the maximum time possible. However, the understanding of the dynamics of the magnetosphere was not possible with only single-spacecraft missions and theoretical models.

The next stage in magnetosphere exploration were the multi-spacecraft missions. They allowed the identification of boundaries and linked their dynamics with processes in the solar wind. In the 1990s, a collaboration between NASA, the European Space Agency (ESA), the Institute of Space and Astronautical Science of Japan (ISAS), and the Russian Space Agency (now Roscosmos) created the International Solar-Terrestrial (ISTP) initiative to simultaneously observe the Sun-Earth environment (*Peredo et al.*, 1997). From the 2000s, missions such as Cluster, THEMIS, and Magnetospheric Multiscale (MMS) mission are still providing compelling observations about how the transfer of energy from the solar wind into the magnetosphere occurs. These missions were designed to answer questions about the dynamics of the magnetosphere, e.g. THEMIS observed where and when substorms are generated, and MMS observed magnetic reconnection on scales similar to the found in the electron diffusion region.

In analogy to how MMS is able to explore magnetic reconnection by observing across a very small region (*Burch et al.*, 2016), the combination of many spacecraft simultaneously in orbit can help us to understand the dynamics of the magnetosphere in a larger scale than using only single mission observations (*Angelopoulos*, 2010). One of the best demonstrations of the contribution of large spatial scale observations was performed by the THEMIS mission. The THEMIS spacecraft aligned at different distances from 12 to 30 Earth radius (Re) on the tail magnetosphere. Using the three inner probes they monitor the current disruption onset while the two outermost

spacecraft track the plasma acceleration resulting from magnetic reconnection. This tracking made it possible to determine which process occurs first, and also link phenomena in the ionosphere with the observations in the tail (*Angelopoulos*, 2009; *Frey et al.*, 2008).

This combination of multiple spacecraft in the heliosphere is called the Heliophysics System Observatory (HSO). The HSO can be seen as a single instrument able to perform simultaneous observations of distant regions of the solar wind and magnetosphere, whose capabilities can be added to ground-based magnetometer observations. Since new spacecraft missions are constantly being launched while others are being deactivated, the capabilities of the HSO are also in constant evolution presenting a challenge from the point of view of systematic study of the dynamics of the magnetosphere, but also an opportunity to study different processes in the magnetosphere.

In this work, the combined observations performed by ground-based magnetometers and the HSO are used to study the following aspects of the dynamics of the magnetosphere. The main science questions investigated are as follows:

1. How does the magnetosphere respond to solar wind DPPs during northward IMF?, and What are the effects of the traveling disturbances compressing the tail of the magnetosphere?

2. What are the effects of inclined interplanetary shocks in the propagation of the preliminary impulse through the magnetosphere to the ground?

3. What is the radial profile of the magnetospheric plasma mass density? How does the profile affect the propagation of the preliminary reverse impulse?

The response of the Earth's magnetosphere to solar wind DPPs have been widely studied from multiple perspectives. Previous analysis have consisted in spacecraft

observations and also numerical simulations. These studies have covered different kinds of DPPs, under southward and northward IMF.

DPPs can be generated by multiple mechanisms in the solar wind, and sudden increases in the dynamic pressure can be the result of changes in the solar wind speed, density or both. From the experimental perspective, the impact on the magnetosphere dynamics of these different kinds of DPPs have been addressed using ground-based, and spacecraft observations. Such studies have been limited by the availability of observations, and sampling has been limited to specific events, or statistical analysis of specific regions of the magnetosphere. The first research question is designed to address this limitation by taking the advantage of the HSO to perform simultaneous observations at multiple regions and local time sectors, and obtain a global view of the magnetospheric dynamics.

Under southward IMF the magnetospheric response to DPPs is dominated by the outcomes of the equatorial magnetic reconnection in both dayside and nightside sectors. The magnetic reconnection triggers an important change in the magnetospheric topology. In the dayside the magnetic field breaks and convects towards the nightside, and in the nightside flux ropes convects towards Earth. In general, during southward IMF the magnetosphere enters in a turbulent state where multiple kinds of plasma waves and magnetospheric oscillation modes superpose to each other. Meanwhile, during northward IMF the magnetosphere is in a steady state with little magnetospheric convection and small turbulence and waves other than the generated by the impact of solar wind disturbances.

For many years ground-based magnetometer projects developed their own methodologies, standards, and formats for their data. This led to constant problems to perform global studies of the response as combining arrays from different projects presented a challenge. However, recently 1 second resolution ground-based magnetometers have been available through collaborative projects as SuperMag and In-

termagnet, the cooperation between the projects have allowed the standardization of data from multiple arrays. These new data in combination with the HSO allow a finer study of wave propagation than have been ever possible in the past. In the dayside magnetosphere, precise information about the shock inclination could be obtained with a deeper knowledge of how the fast and Alfvén mode waves propagate through the dayside magnetosphere. The second and third research questions are designed to investigate the impact of interplanetary shock inclination and magnetosphere plasma mass density in the propagation of waves in the dayside magnetosphere with the objective of understanding the observations made on ground.

This dissertation is organized as follows: the next section presents the general description of the magnetosphere, MHD theory, Ultra Low Frequency (ULF) waves, and the solar wind. Chapter II explains the characteristics of the spacecraft missions, their orbit, data characteristics, and data formats. In Chapter III, I explain in detail the methodology used for the detection of events of interest for this study. Chapters IV to VI consist of investigations of the questions previously mentioned. Finally, Chapter VII contains the summary of the results and relevance for future work.

1.2 Theoretical Background

1.2.1 The MHD Theory

A plasma is low density and ionized gas composed of charged particles that interact with each other and with magnetic fields. The study of the magnetic properties and behavior of plasmas is known as MHD theory and consists of a framework of equations that explains the behavior of magnetic fields in conductive fluids. The MHD theory consists of macroscopic transport equations for gasses of hydrodynamics combined with Maxwell's equations of electromagnetism and is the base of the current knowledge in magnetized plasma found in planetary magnetospheres, stars and interplanetary

environments. The MHD macroscopic theory is derived under the principle that the length scale of the perturbations in the plasma are much larger than the Debye length, and the gyroradius of constituent charged particles in the plasma. The Debye length is the distance where the electric potential will decrease by $1/e$ as result of the screening of electrons over ions, and the gyroradius is the radius of the circular motion of a charged particle in an uniform magnetic field. Analogously in time, the MHD approximation is valid in time scales much longer than the inverse of the plasma frequency and charged particle cyclotron frequencies. Since the MHD theory is a low-frequency approximation, it is effective for describing ULF waves. In the context of this work, the MHD theory is used to understand the propagation of waves in the magnetosphere, such as their speed, propagation direction, and as an indirect method to estimate magnetospheric plasma density.

The behavior of the magnetized plasma found in the Earth's magnetosphere and the interplanetary space environment can be explained by a set of simplified equations from the MHD theory under the following assumptions:

- The plasma is close to thermodynamic equilibrium.
- Heat flow can be neglected.
- The plasma is quasi-neutral.
- The high-frequency oscillations of the electric field are neglected, this means the displacement current of the Maxwell equations is not considered.
- Ohm's law for ideal MHD assumes infinite conductivity: the magnetic field is frozen-in the plasma.

Using these assumptions, the MHD transport equations become the ideal MHD equations. The equations for a collisionless single fluid m are:

$$
\begin{aligned}
\frac{\partial \rho_m}{\partial t} + \nabla \cdot (\rho_m \mathbf{u}) &= 0 \\
\rho_m \frac{\partial \mathbf{u}}{\partial t} + \rho_m (\mathbf{u} \cdot \nabla)\mathbf{u} + \nabla p - \rho_m \mathbf{g} - \mathbf{j} \times \mathbf{B} &= 0 \\
\frac{3}{2}\frac{\partial p}{\partial t} + \frac{3}{2}(\mathbf{u} \cdot \nabla)p + \frac{5}{2}p(\nabla \cdot \mathbf{u}) &= 0 \\
\frac{\partial \mathbf{B}}{\partial t} - \nabla \times (\mathbf{u} \times \mathbf{B}) &= -\eta_m \nabla^2 \mathbf{B}
\end{aligned}
\tag{1.1}
$$

The linearized ideal MHD equations are obtained by linearization of the MHD variables, by considering the plasma is affected only by small amplitude disturbances: $\rho_m = \rho_{m_0} + \rho_{m_1}$, $\mathbf{u} = \mathbf{u}_1$, $p = p_0 + p_1$, and $\mathbf{B} = \mathbf{B}_0 + \mathbf{B}_1$. The linear ideal MHD equations are:

$$
\begin{aligned}
\frac{\partial \rho_{m_1}}{\partial t} + \rho_{m_0}(\nabla \cdot \mathbf{u}_1) + (\mathbf{u}_1 \cdot \nabla)\rho_{m_0} &= 0 \\
\rho_{m_0}\frac{\partial \mathbf{u}_1}{\partial t} + \nabla(p_0 + p_1) + \nabla\frac{\mathbf{B}_0 \cdot \mathbf{B}_1}{\mu_0} - \nabla \cdot \left(\frac{\mathbf{B}_0\mathbf{B}_1 + \mathbf{B}_1\mathbf{B}_0}{\mu_0}\right) &= (\rho_{m_0} + \rho_{m_1})\mathbf{g} \\
\frac{3}{2}\frac{\partial p_1}{\partial t} + \frac{3}{2}(\mathbf{u}_1 \cdot \nabla)p_0 + \frac{5}{2}p_0(\nabla \cdot \mathbf{u}_1) &= 0 \\
\frac{\partial \mathbf{B}_1}{\partial t} - \nabla \times (\mathbf{u}_1 \times \mathbf{B}_0) &= -\eta_m \nabla^2 \mathbf{B}_1
\end{aligned}
\tag{1.2}
$$

1.2.2 MHD Waves

These set of equations are the base of the study of ULF waves in cold plasmas in the heliosphere. Further assumptions about the associated perturbations in a plasma allow the identification of different types of plasma waves.

In any compressible fluid the simplest waves are the sound waves. If external forces such as magnetic field and gravity are neglected, and there is a constant density and pressure background, it can be shown that equations (1.2) become the wave equation for compressional plasma:

$$\begin{aligned} \frac{\partial^2 \rho_{m_1}}{\partial t^2} &= \frac{5}{3}\frac{p_0}{\rho_{m_0}}\nabla^2 \rho_{m_1} \\ \frac{\partial^2 \mathbf{u}_1}{\partial t^2} &= \frac{5}{3}\frac{p_0}{\rho_{m_0}}\nabla^2 \mathbf{u}_1 \end{aligned} \tag{1.3}$$

where $a_s = \sqrt{\frac{5}{3}\frac{p_0}{\rho_{m_0}}}$ is the acoustic wave or sound wave speed. In plasma the total gas pressure is the sum of electron and ion pressure ($p_0 = p_e + p_{ion}$). Since the ion mass is much larger than the electron mass ($m_{ion} \gg m_e$), and the electron temperature is much larger than the ion temperature ($T_e \gg T_{ion}$), the electron mass can be neglected. This wave is also called the *ion-acoustic* wave and the wave speed is written as $a_{ion-acoustic} = \sqrt{\frac{5}{3}\frac{k(T_e+T_{ion})}{m_{ion}}}$.

1.2.3 Ideal MHD Waves

Alfvén waves are one of the most fundamental waves in magnetized plasmas. They are the result of the restoring force after an external force disturbs a magnetic field. The Alfvén waves are non-compressional and they propagate parallel to the magnetic field. If we consider a cold plasma (i.e. gas pressure is negligible), a non-compressive disturbance ($\nabla \cdot \mathbf{u}_1 = 0$) in a constant background density ($\rho_{m_1} = const$) and with an infinite conductivity, the perpendicular perturbation to the background field would be described by the following wave equations:

$$\begin{aligned} \frac{\partial^2 \mathbf{u}_1}{\partial t^2} &= \frac{B_0^2}{\mu_0 \rho_{m_0}}\nabla^2 \mathbf{u}_1 \\ \frac{\partial^2 \mathbf{B}_1}{\partial t^2} &= \frac{B_0^2}{\mu_0 \rho_{m_0}}\nabla^2 \mathbf{B}_1 \end{aligned} \tag{1.4}$$

Then the non-compressive waves propagate at the Alfvén speed $v_A = \frac{B_0}{\sqrt{\mu_0 \rho_{m_0}}}$. However, in general the assumption of incompressibility is not always true. The solutions for the compressional waves are found assuming a plane wave solution in

a uniform background magnetic field for small perturbations in density, pressure, and magnetic field using the ideal MHD equations. These assumptions lead to the dispersion relation for MHD waves:

$$\omega(\omega^2 - k^2 v_A^2 cos^2\theta)[\omega^4 - \omega^2 k^2(a_s^2 + v_A^2) + a_s^2 v_A^2 k^4 cos^2\theta] = 0 \tag{1.5}$$

where θ is the angle between the background magnetic field and the wave vector $\mathbf{k}$. This dispersion relation describes several different type of waves, from which we identify two special cases:

- The first case is obtained from the solution of the first parentheses of equation (1.5). This wave only propagates parallel to the background magnetic field ($\mathbf{k} \parallel \mathbf{B}_0$).

$$\frac{\omega^2}{k_z^2} = v_A^2 cos^2\theta \tag{1.6}$$

  This is the Alfvén or intermediate wave.

- The second case is the solution of the second parentheses:

$$\frac{\omega^2}{k^2} = \frac{1}{2}\left[(a_s^2 + v_A^2) \pm \sqrt{(a_s^2 + v_A^2)^2 - 4a_s^2 v_A cos^2\theta}\right] \tag{1.7}$$

  The positive and negative sign correspond to the *fast* and *slow magnetosonic* waves.

The polar representation of the speed of these waves with respect to the background magnetic field is shown in Figure 1.1.

As their name indicate the fast magnetosonic wave is the fastest, followed by the Alfvén wave, and then the slow magnetosonic wave ($v_{ph_f}^2 \geq v_{ph_A}^2 \geq v_{ph_s}^2$). As a consequence, when the magnetic field is perturbed by an external force, the fast magnetosonic wave is the fastest of all and the first that would reach a distant observer (such a ground-based magnetometer) as it travels perpendicularly to the magnetic

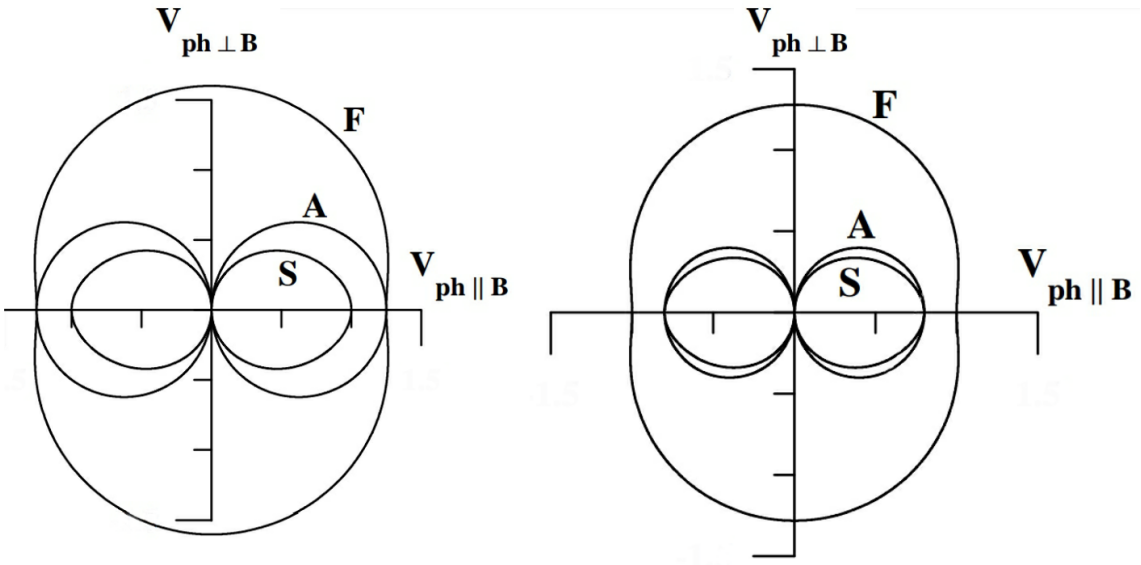

Figure 1.1: Phase speed polar diagram for MHD waves relative to a constant magnetic field background. (Left) The Alfvén speed is smaller than the sound speed. (Right) The Alfvén speed is greater than the sound speed. Modified from *Lubchich and Despirak* (2005).

field. Meanwhile, the Alfvén wave takes a longer path by following the magnetic field path line.

1.3 The Earth's Magnetosphere

1.3.1 General Structure

The magnetosphere is the external portion of the Earth's magnetic field that interacts with the solar wind. The most accepted explanation for the generation of the Earth's magnetic field is the dynamo theory, this theory states the Earth's magnetic field is generated by the rotation and convection of conductive fluids in the outer core. As shown in Figure 1.2, the magnetosphere forms a cavity around Earth composed of magnetic field and low density plasma that protects Earth from the direct impact of high energy charged particles in the solar wind. The plasma in the magnetosphere is highly conductive which allows the propagation of MHD waves and

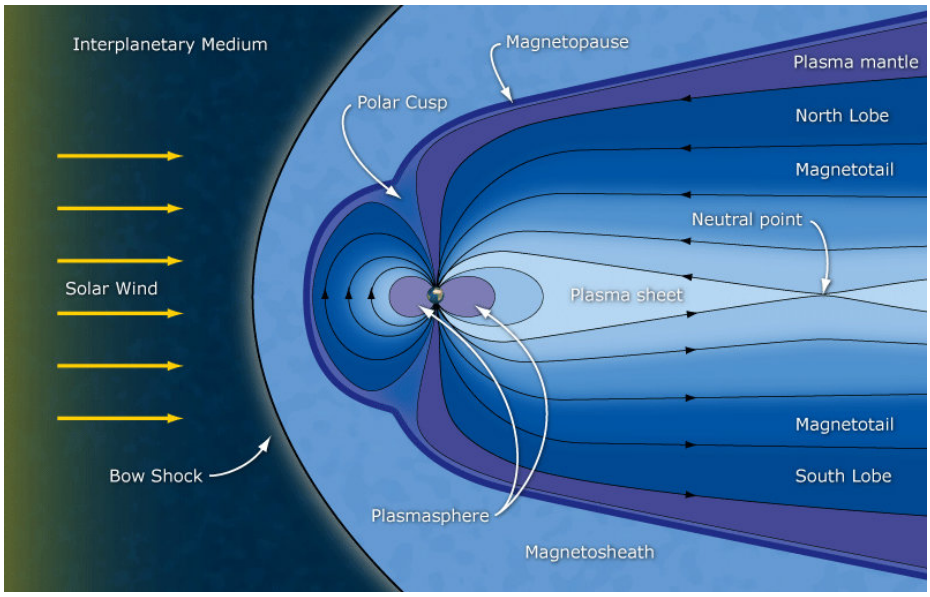

Figure 1.2: Diagram of the Earth's magnetosphere. Image credit:ESA/C. T. Russell.

electric currents that induce their own magnetic field, the superposition of magnetic field and currents and their dependence with the solar wind makes the magnetosphere a highly dynamic environment.

The dayside magnetosphere is constantly compressed by the solar wind, the dynamic and magnetic pressure keeps the dayside magnetosphere confined at about 10 Re from Earth. However, the dayside magnetosphere is continuously contracting and expanding due to sudden changes in the solar wind dynamic pressure. Meanwhile, in the night sector the situation is the opposite, the magnetosphere is stretched out hundreds of Earth radii in antisunward direction, giving origin to the magnetotail. The night side of the magnetosphere has been observed more than 200 Re away from Earth (*Slavin et al.*, 1983).

The solar wind is a supersonic plasma since its speed is larger than the fast magnetosonic speed, when the solar wind reaches Earth, the magnetosphere acts as an obstacle and induces a bow shock in front of it. In the bow shock the solar wind slows down and gets compressed. The region between the bow shock and the magnetosphere is called the magnetosheath and is composed of subsonic solar wind

that flows around the magnetosphere. The boundary between the solar wind and the magnetosphere is the magnetopause. The magnetopause is also the boundary between the magnetosphere and the shocked solar wind. The location of the magnetopause is determined by the equilibrium between the magnetic and dynamic pressure of the solar wind with the magnetic pressure exerted by the magnetosphere. Since the source of the magnetic pressure of the magnetosphere is stable over long periods of time, it is the solar wind which finally controls the location of the magnetopause. *Chapman and Ferraro* (1930) suggested that the solar wind can be seen as a moving conductive surface. Since the magnetic field cannot penetrate conductive surfaces, the solar wind flows around the magnetosphere creating a current that acts as a shield that opposes the solar wind and separates it from entering directly into the magnetosphere. Their theory was later confirmed and this current is now known as the Chapman-Ferraro current and gives origin to the concept of the magnetopause.

The inner region of the magnetosphere is known as the plasmasphere. The plasmasphere has a toroidal shape and is formed by closed magnetic field lines. The plasma inside the plasmasphere is composed of electrons and ions of ionospheric origin. These charged particles are trapped by magnetic field lines and form a cold plasma around the Earth up to 4-5 Earth radii. The plasmasphere is coupled to the ionosphere which delimits its inner edge. In the boundary of the plasmasphere with the ionosphere the plasma density is maximum. Then, the plasma density decreases until it reaches the outer edge. The outer edge of the plasmasphere is called plasmapause and is defined by a sudden drop of the plasma density (*Carpenter*, 1963; *Chi and Russell*, 2005; *Lee and Lysak*, 1989), however there are also studies showing evidence of a smooth density transition between the plasmasphere and subauroral regions (*Tu et al.*, 2007).

The magnetotail is the region in the nightside of the magnetosphere. The magnetotail is constantly stretched by the flow of the solar wind and consists of two tail lobes separated by the plasma sheet. The tail lobes have a low plasma density ($\sim$0.01

cm^{-3}) and a magnetic field magnitude of around 20 nT that maps into the polar cap of each Earth's magnetic hemisphere. The plasma sheet is the region in between the two lobes. In the plasma sheet the magnetic field is weak ($\sim$10 nT) and the density is around 30 times larger than in the lobes ($\sim$0.3 cm^{-3}). In the tail lobe the magnetic pressure is larger than the plasma pressure, while in the plasma sheet it is the opposite. As a result of the low magnetic field and high density in the plasma sheet, the plasma sheet is the region where magnetic reconnection occurs in the nightside magnetosphere and the source of energy for substorms.

1.3.2 Dungey Cycle

It is well known that in reality the magnetosphere is not completely shielded from the solar wind. In the 1960s, Dungey observed ionospheric convection patterns and proposed convection pattern models for the convection in the magnetosphere. Dungey's model suggested that the dynamics of the magnetosphere and the interaction between the solar wind and the magnetosphere coupled through magnetic reconnection, this phenomenon is currently known as the Dungey cycle. The Dungey cycle (shown in Figure 1.3) start when a southward IMF impacts the subsolar point of the dayside magnetopause, the IMF reconnects with the magnetosphere and split the magnetic field line allowing the solar wind plasma to enter into the magnetospheric cavity. As the magnetic field is frozen-in the solar wind plasma, the open magnetic field lines are carried in tailward direction from the dayside to the nightside. In the night side a similar process involving magnetic reconnection occurs. The boundary of the magnetotail is compressed by the solar wind and the IMF, making the magnetic field of the plasma sheet even weaker up to the point the magnetic field from the opposite lobes reconnect. The reconnection process heats and energizes the plasma and is the source of substorms observed at high latitudes.

During the times the IMF is northward, the magnetic field from the solar wind

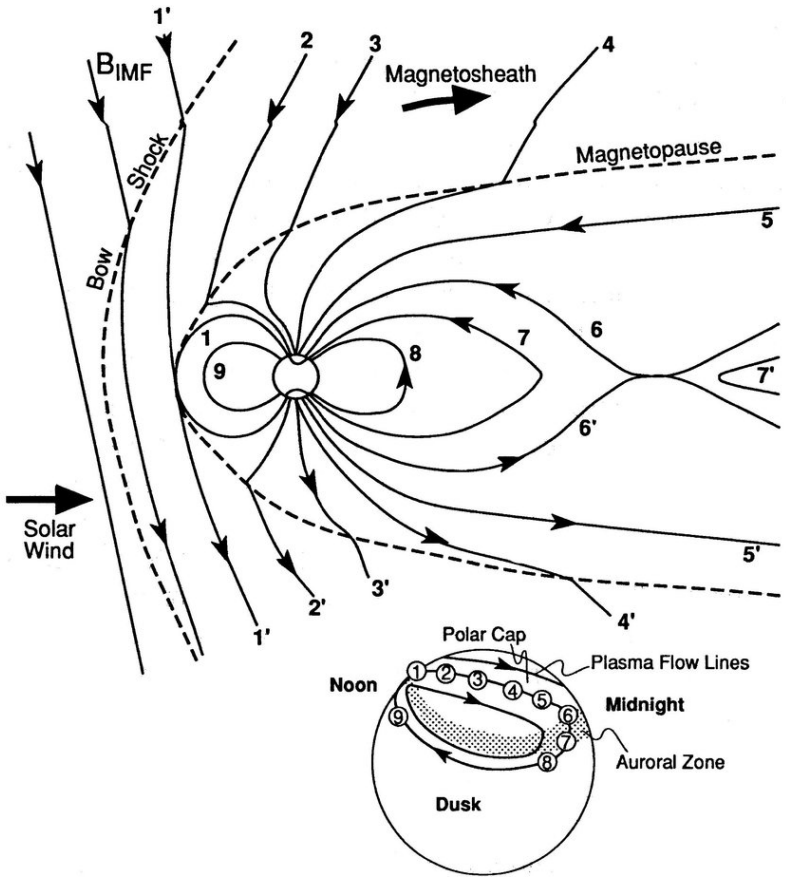

Figure 1.3: Diagram of Dungey's cycle. (1) Magnetic reconnection in the dayside. (2-4) The frozen-in flux magnetic field is carried tailward. (6) magnetic reconnection in the nightside. Figure obtained from *Kivelson et al.* (1995).

strengthens the dayside magnetosphere magnetic field. This intensifies the shielding capacity of the magnetosphere and reduces the plasma density in the magnetosphere. However, the magnetosphere is still not completely shielded, as high-latitude reconnection still occurs near the dayside cusp. Despite that, events during northward IMF conditions are still ideal for wave propagation studies as the magnetic disturbances from magnetic reconnection have smaller amplitudes during these circumstances.

1.3.3 Ring Current

The ring current consists of charged particles that longitudinally drift around Earth at distances between 2 and 7 Re. The drift is the result of the radial magnetic field strength gradient. As charged particles have a larger gyroradius in a weaker magnetic field than in a strong magnetic field, the charged particles drift every time they are moving away from Earth, and stay anchored in the stronger magnetic field when moving closer to Earth. The electrons drift eastward while the ions (mainly H^+, He^+,O^+) drift westwards. The charge separation creates the ring current which reduces the global strength of the Earth's magnetic field. The intensity of the ring current is monitored by ground-based magnetometer stations as an indicator of geomagnetic activity.

1.3.4 Disturbance Storm-Time and Symmetric-Horizontal Indices

The Disturbance Storm-Time (DST) index is a measure of the horizontal equatorial magnetic field variation as a result of the magnetic field induced by the ring current. Since its value is computed in base of a magnetic quiet curve, the DST index is also able to detect the magnetic compression generated by solar wind DPPs on the magnetosphere that increase the magnetic field magnitude observed by ground-based magnetometers. The DST index has been calculated by the World Data Center for Geomagnetism in Kyoto Japan since 1957. For its calculation, four low-latitude

ground-based magnetometers are used to obtain one value each hour. During the last decades the increase in number, spatial coverage, and time sampling resolution of ground-based magnetometer stations, new alternatives to the DST index are being developed such as the Symmetric-Horizontal (SYM-H) index. The SYM-H index also computes the magnetic field strength variation due to the magnetic field generated by the ring current. This index is computed using 11 ground-based magnetometer stations around the world. The base magnetic field curve for SYM-H index is computed with a different methodology than for DST index. This means the SYM-H index is not a higher resolution DST index, but rather an equivalent with higher resolution than the storm time index (*Wanliss and Showalter*, 2006).

1.4 The Solar Wind

The solar wind is a low density magnetized plasma composed of electrons and ions released from the solar corona with a variable plasma density around 5 cm^{-3}. The speed of the solar wind generally ranges between 300-500 km/s, but on occasions have reached above 1000 km/s. The IMF magnetic field strength is around 10 nT, and the B_z component in general ranges between -5 and 5 nT. Since the solar wind is expelled in all directions, at Earth's orbit the solar wind flow is mainly along the Sun-Earth direction. The solar wind is the source of energy that drives the processes in the magnetosphere and its interaction with the magnetosphere is a fundamental problem in space physics (*Lopez et al.*, 2004). Energy from the solar wind transfers as magnetic waves and injection of energetic particles into the magnetospheric cavity through magnetic reconnection (*Allen et al.*, 2016; *Lee et al.*, 1982). The solar wind plasma exerts dynamic and magnetic pressure against the magnetosphere. The dynamic pressure is a function of the plasma density and speed (ρv^2), while the magnetic pressure is only a function of the magnetic field magnitude ($B^2/2\mu$). These kinds of pressure control the location of the magnetopause and the global dynamics of the

magnetosphere though the dynamic pressure dominates the IMF magnetic pressure.

The flow of solar wind and magnetic field is constantly compressing the magnetosphere, but sudden changes are common. These disturbances have origin in the solar corona where the magnetized plasma is expelled. The ICMEs, and CIRs are the most common source of disturbances observed in the solar wind. In both cases a fast cloud of solar wind plasma flow runs into slower plasma generating a region of enhanced density and magnetic field strength. However, since ICMEs are very energetic their speed is often large enough to generate interplanetary shocks while CIRs usually do not develop shocks at 1 Astronomical Unit (AU). Both solar wind disturbances have fronts where the conditions such as density, speed, and magnetic field drastically change even though their origin is different.

1.4.1 Interplanetary Coronal Mass Ejections

Coronal Mass Ejections (CMEs) are transient high energy releases of plasma and magnetic fields with origin in the solar corona. The majority of CMEs originate in regions of closed magnetic field lines that are strong enough to constrain the plasma from expanding outwards, but are later suddenly released by magnetic reconnection. Their propagating counterparts in the interplanetary environment are the ICMEs. In the solar wind they form large-scale structures with larger magnetic field, and plasma density than surrounding solar wind. ICMEs often form helicoidal structures (as shown in Figure 1.4) that expand during their propagation through the space environment. The relative speed of propagation of ICMEs with respect to the preceding solar wind is often larger than the fast mode (or fast magnetosonic) speed, generating a propagating shock in front of the ICME. ICMEs are the main source of interplanetary shocks observed in the heliosphere, and responsible for the largest geomagnetic storms observed on Earth.

Fast forward shocks are the most common type of shocks (*Echer et al.*, 2005). All

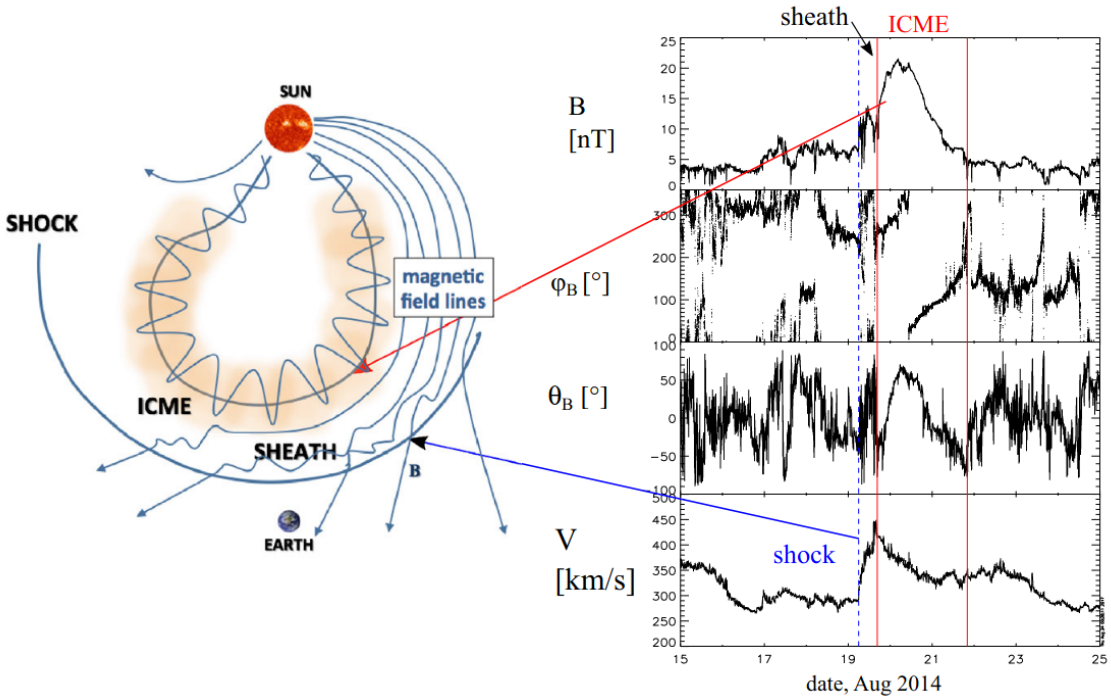

Figure 1.4: (Left) Scheme of an ICME. (Right) Solar wind observations during a ICME made by ACE at the Lagrangian L_1 point. From top to bottom: Magnetic field strength, longitude and latitude of the magnetic field in GSM coordinates, and solar wind speed. Figure obtained from *Kilpua et al.* (2017).

the events analyzed in Chapter V are fast forward shocks. The diagram on Figure 1.4 shows the main structure of an ICME with an helicoidal structure and a sheath of shocked plasma behind the shock front. In the right side panel are shown the magnetic field strength and solar wind speed in a ICME observed by ACE spacecraft at the Lagrangian point L_1. The magnetic field strength suddenly increases, and also the velocity of the solar wind, which is one of the factors that increases the solar wind dynamic pressure that triggers disturbances in the magnetosphere.

1.4.2 Corotating Interaction Regions

Corotating Interaction Regions are large-scale plasma compressing structures that form as result of fast solar wind stream interacting with slow solar wind. This is result

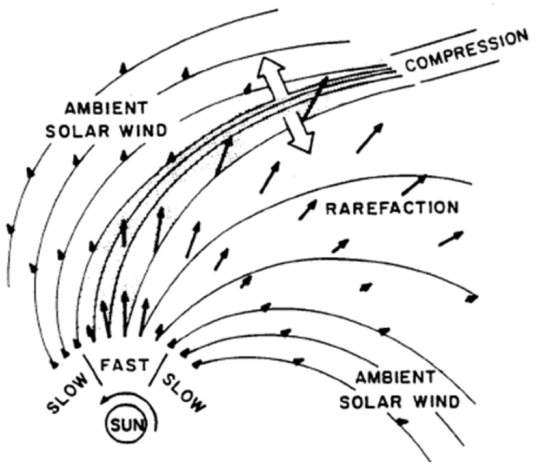

Figure 1.5: Scheme of a CIR. Fast solar wind generates a compression region behind the slow solar wind. Figure obtained from *Pizzo* (1978).

of the radial alignment of solar wind flows with large speed differences. The fast solar wind has a speed around ∼800 km/s and is associated with regions where coronal holes are observed. Meanwhile, slow solar wind has an average speed of ∼400 km/s and comes from regions with regular solar magnetic closed field regions. Since, the Sun has a rotation (see Figure 1.5) with respect to Earth of approximately 27 days, an observer at Earth's orbit would measure intermittent streams of fast and slow solar wind. In some cases, the fast runs into the slow solar wind creating a compression region in the middle of fast and slow solar wind streams. The solar wind DPPs from CIRs often have a smaller magnitude and rarely develop an interplanetary shock at 1 AU.

Inside the CIR there there is at least one stream interface that separates the hot, low density, and fast solar wind that departed from coronal holes, and the cold, more dense, and slow solar wind from the streamer belt (*Gosling et al.*, 1978, 1981). The interface is important as defines the structure inside the CIR. In the interface often are found changes in density, temperature, wave amplitude, and the H/He abundance ratio that on average suddenly increase at the interface.

1.5 Discontinuities and Shocks

In the lower atmosphere shocks are the result of a disturbance that propagates faster than the speed of sound. In general, discontinuities and shocks are transition layers where the fluid equilibrium state changes from one to a different one as sudden changes in pressure, temperature, and density of the medium. They can be generated by supersonic airplanes, bomb explosions, and explosive volcanic eruptions.

In the solar wind, ICMEs and CIRs can form discontinuities in the plasma. If we consider a steady, planar and infinitesimal discontinuity where all quantities change only in the perpendicular to the discontinuity, the conservation equations of mass, energy, and momentum can be rewritten as the *Rankine-Hugoniot jump conditions* for ideal MHD.

$$\begin{aligned}
&[\rho_m u_n] = 0 \\
&\left[\rho_m u_n \mathbf{u}_t - \frac{B_n \mathbf{B}_t}{\mu_0}\right] = 0 \\
&\left[\rho_m u_n^2 + p + \frac{B_t^2 - B_n^2}{2\mu_0}\right] = 0 \\
&\left[\frac{1}{2}\rho_m (u_n^2 + u_t^2) u_n + \frac{\gamma}{\gamma - 1} p u_n + \frac{B_t^2}{\mu_0} u_n - \frac{B_n}{\mu_0}(\mathbf{B}_t \cdot \mathbf{u}_t)\right] = 0
\end{aligned} \tag{1.8}$$

The n and t subscripts refer to the normal and tangential component vectors in the discontinuity reference frame. The bracket notation refers to the jump across the discontinuity between upstream (1) and (2) downstream conditions:

$$[F] = F_2 - F_1 \tag{1.9}$$

This set of equations describe several types of MHD discontinuities and shocks. If there is not particle flux between across the transition layer ($u_{1n} = u_{2n} = 0$), the transition layer is called a discontinuity and the two possible solution to the equations

1.8 define the *tangential discontinuity* and *contact discontinuity*. The derivation of equations 1.8 for not flux across the discontinuity simplify to the following:

$$\begin{aligned}
&[B_n \mathbf{B}_t] = 0 \\
&\left[p + \frac{B_t^2 - B_n^2}{2\mu_0}\right] = 0 \\
&[B_n(\mathbf{B}_t \cdot \mathbf{u}_t)] = 0 \\
&[B_n \mathbf{u}_t] = 0 \\
&[B_n] = 0
\end{aligned} \tag{1.10}$$

In the case of the tangential discontinuity the magnetic field does not cross the discontinuity, and the normal magnetic field are zero in both sides of the transition ($B_{n1} = B_{n2} = 0$), then the only jump condition left is the conservation of momentum:

$$\left[p + \frac{B_t^2}{2\mu_0}\right] \tag{1.11}$$

The second solution for equations 1.8 describes the contact discontinuity. In this case ($B_{n1} = B_{n2} \neq 0$) which leads to the following jump conditions:

$$\begin{aligned}
&[\mathbf{B}_t] = 0 \\
&[p] = 0 \\
&[\mathbf{u}_t] = 0
\end{aligned} \tag{1.12}$$

In a contact discontinuity there is not flux through the transition, but all the other quantities remain continuous across the transition.

In the case there is transport across the transition layer, the discontinuities are referred to as shocks instead. There are three types of shocks: *Alfvén shocks* or

rotational discontinuities, slow shocks, and fast shocks.

Alfvén shocks are non-compressive, the velocity across the shock is continuous, but different than zero ($u_{n1} = u_{n2} = u_n \neq 0$) while the plasma mass density remains constant ($\rho_m 1 = \rho_{m2} = \rho_m$). Under these conditions, the jump conditions become the following:

$$\begin{aligned}
&\rho_m u_n[\mathbf{u}_t] - \frac{B_n}{\mu_0}[\mathbf{B}_t] = 0 \\
&\left[p + \frac{B_t^2}{2\mu_0}\right] = 0 \\
&\frac{1}{2}\rho_m u_n[u_t^2] + \frac{\gamma}{\gamma - 1}u_n[p] + u_n\left[\frac{B_t^2}{\mu_0}\right] - \frac{B_n}{\mu_0}[(\mathbf{B}_t \cdot \mathbf{u}_t)] = 0 \\
&u_n[\mathbf{B}_t] - B_n[\mathbf{u}_t] = 0
\end{aligned} \tag{1.13}$$

Combining the first and last equations form the jump conditions equations 1.13 we can obtain:

$$\left(u_n^2 - \frac{B_n^2}{\rho_m \mu_0}\right)[\mathbf{B}_t] = 0 \tag{1.14}$$

which means, if $[\mathbf{B}_t] \neq 0$, the speed of the plasma across the transition can only be the Alfvén speed,

$$u_n = \pm\frac{B_n}{\sqrt{\rho_m \mu_0}} = \pm V_{An} \tag{1.15}$$

which means the Alfvén shock propagates at Alfvén speed with respect to the plasma.

The other types of shock are called compressive shocks. In these shocks the plasma mass flux is conserved through the shock ($\Phi_m = \rho_{m1} u_{n1} = \rho_{m2} u_{n2}$). In this case the jump conditions equations become:

$$
\begin{aligned}
&\Phi_m[u_n] + [p] + \left[\frac{B_t^2}{2\mu_0}\right] = 0 \\
&[u_n B_t] - \frac{B_n^2}{\Phi_m \mu_0}[B_t] = 0 \\
&[u_t] - \frac{B_n}{\Phi_m \mu_0}[B_t] = 0 \\
&\frac{1}{2}\Phi_m[u_n^2] + \frac{\gamma}{\gamma - 1}[p u_n] + \left[\frac{B_t^2}{\mu_0} u_n\right] - \frac{B_n^2}{2\mu_0^2 \Phi_2}[\mathbf{B}_t] = 0
\end{aligned}
\tag{1.16}
$$

This set equations have two nontrivial solutions that represent two compressive shocks cases. The first solution represents the slow shocks where the plasma flows through the transition layer at the slow wave mode speed. A slow shock is characterized for a decrease in the tangential component of the magnetic field across the shock. The second solution represents the case when the flow moves at the fast mode wave speed through the shock. Fast shocks are characterized by an increase in the tangential component of the magnetic field across the shock.

$$
a_{slow}^2 = \frac{1}{2}\left[(a_s^2 + V_A^2) - \sqrt{(a_s^2 + V_A^2)^2 - 4a_s^2 V_{A_n}^2}\right] \tag{1.17}
$$

$$
a_{fast}^2 = \frac{1}{2}\left[(a_s^2 + V_A^2) + \sqrt{(a_s^2 + V_A^2)^2 - 4a_s^2 V_{A_n}^2}\right] \tag{1.18}
$$

Slow shocks are characterized for a decrease in the tangential magnetic field across the shock while fast shocks are characterized by an increase of the magnetic field

CHAPTER II

Data

The HSO spacecraft constellation consists of several missions operating simultaneously to understand the dynamics of the heliosphere. Each mission has their own compelling science objectives, and carry different payload on-board, but it is well known that combinations of missions allow larger scale investigations. For this reason, the HSO missions have worked together to coordinate their orbits to achieve a cross-scale constellation for the magnetosphere (*Frey et al.*, 2014). In order to compare distant observations, I focused on the analysis of magnetometer data from all the spacecraft that carry a fluxgate magnetometer as part of their payload. Additionally, the missions selected correspond to the spacecraft located in the solar wind, or inside the Earth's magnetosphere. The period of time was selected to maximize the availability of simultaneous observations between spacecraft and also ground-based magnetometer stations. The timeline of the missions is shown in Figure 2.1.

2.1 The Fluxgate Magnetometer

The spacecraft missions of the HSO are focused to study different regions and processes in the magnetosphere and the solar wind. In effect, their payload design is focused on plasma and field observations with special characteristics depending on the region they aim to explore. However, the single instrument that is present in all the

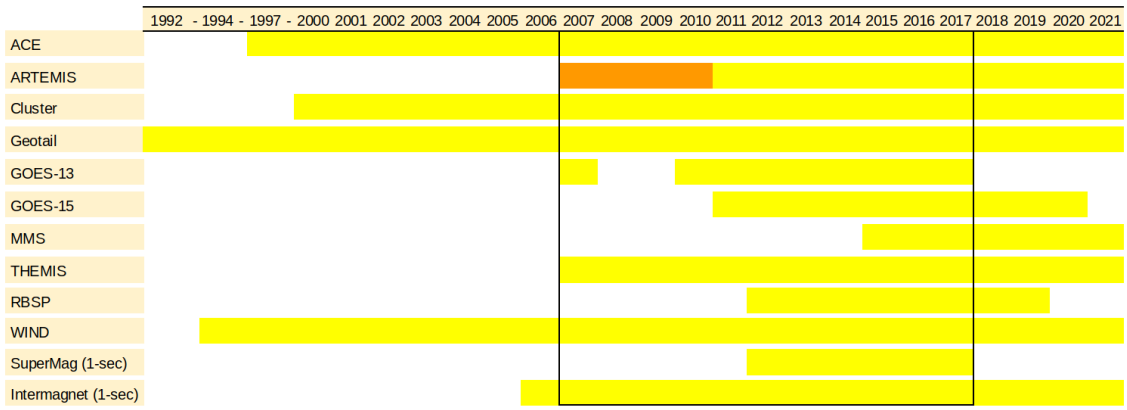

Figure 2.1: Time table of spacecraft operation. Black rectangle indicates years analyzed in this thesis. Orange represents the time Artemis spacecraft operated as part of the THEMIS mission.

spacecraft used in this thesis is the fluxgate magnetometer. Fluxgate magnetometers are common in space exploration because of their stability and high sampling resolution, which is necessary for long-lasting missions measuring highly variably magnetic fields in the heliosphere.

The basic concept of a fluxgate magnetometer is shown in Figure 2.2 and consists of a ring core made of a highly magnetically permeable alloy. The core is surrounded by two conductive windings: the drive winding and the measurement (or sense) winding. A known current is applied to the drive winding. Since the core has the shape of a ring, if the magnetometer is immersed in an external magnetic field, half of the drive coil will generate a field in the direction of the external field and half in the opposite direction to the external field. As the induced and external magnetic fields do not cancel each other a voltage is induced in the sense winding. The portion of the core that is generating the field in the same direction as the external field goes into saturation sooner, the phase between the field generated by each side of the core creates a wave signal that is read by the electronics of the magnetometer.

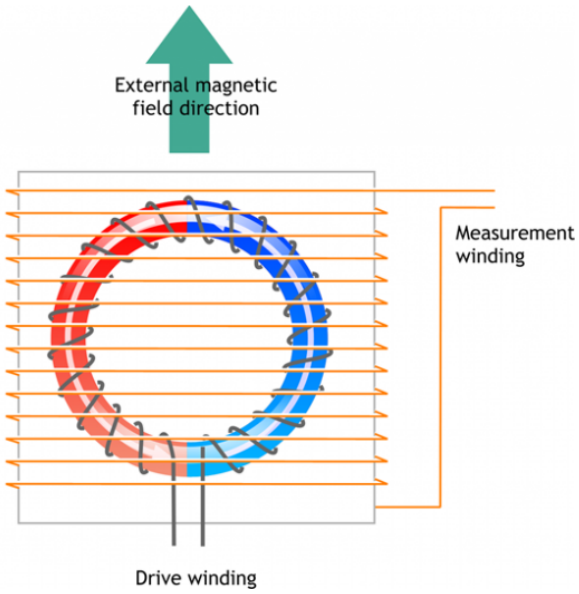

Figure 2.2: Scheme of a fluxgate magnetometer sensor to transform the magnetic field observed into voltage. Courtesy of CARISMA website.

2.2 Solar Wind Data

The main source for solar wind observations in the space physics field are data products resulting from the combination of the ACE and WIND spacecraft, Interplanetary Monitoring Platform 8 (IMP-8), and Geotail. However, during the period 2007-2017, only ACE and WIND spacecraft were available to perform solar wind observations. ACE was launched in 1997 and is expected to continue operating until 2024. ACE is located in the Sun-Earth L_1 Lagrange point, at around 200 Re from Earth. Similarly to ACE, the main scientific objective of WIND is to measure the properties of the solar wind observed from L_1 Lagrange point.

The Space Physics Data Facility (SPDF) uses both spacecraft to create OMNI data. OMNI data consist of combined observations of ACE and WIND that are propagated to the bow shock using the solar wind speed. The OMNI data used in this thesis have a time resolution of 1 minute. The data consist of solar wind plasma density, velocity, and IMF.

2.3 The Geostationary Operational Environmental Satellite (GOES) Mission

The main mission of the Geostationary Operational Environmental Satellite (GOES) spacecraft is to provide observations of the meteorological conditions from a fixed location above the Earth and send the data to ground for operational forecasting (*Lombardi and Hanson*, 2005). However, the GOES spacecraft additionally include fluxgate magnetometers as part of the Space Environment Monitor (SEM). The on-board magnetometer allows the study of the solar wind DPPs, substorms, field-aligned currents and magnetic field reconfigurations, magnetopause crossing and shocks (*Singer et al.*, 1996). The resolution of the magnetometer is ± 0.3 nT, and the highest sampling time resolution of the magnetic field observations is 0.512 seconds.

During the period of time of analysis covered by this thesis, only GOES-13 and GOES-15 has data available for download. As their names indicate GOES-13 is located at geostationary orbit at 6.6 Re from the center of Earth, between 2007 and 2018 it was located at 75° West longitude. GOES-15 was launched in 2006, it is also at 6.6 Re and between 2011 and 2018 was located at 135° West longitude.

2.4 Geotail Mission

Geotail spacecraft was launched in July of 1992 as part of a project between the United States and Japan and by April 28, 2021 was still operational. The main mission of this spacecraft is to understand the processes of acceleration and heating of high temperature plasma, and also to study the dynamics and structure of the magnetotail. The initial orbit of Geotail was planned to cover a range between 8 and 210 Re from Earth (*Nishida*, 1994), but currently the orbit is closer to Earth with a perigee of 8 Re and an apogee of 30 Re. The time resolution available in the CDAWeb is only 1-minute, and in the cases it was required a higher time resolution the data

was manually downloaded from Data ARchives and Transmission System (DARTS) website (www.darts.isas.jaxa.jp).

2.5 Cluster Mission

The Cluster mission was launched in July and August of 2000 and by April 28, 2021 was still operational. Its main science objective is to study the interaction of the solar wind with the magnetosphere. Cluster mission is composed of four identical spacecraft flying in a tetrahedral formation that allows the collection of three-dimensional data. The four spacecraft are FM5 (RUMBA), FM6 (SALSA), FM7 (SAMBA), and FM8 (TANGO) initially had a perigee of 4 Re and apogee of 19 Re, their orbit has changed in time, but not significantly for the purpose of this study. Their orbit drift in time allowing Cluster to observe the magnetotail, but also the dayside magnetosphere boundaries and solar wind.

Among several instruments, each Cluster spacecraft carries a Fluxgate Magnetometer (FGM), a high resolution ion spectrometer (CIS), and an electrostatic electron analyzer (PEACE). In the -1024 to +1023.9 nT range, the FGM instrument has a resolution of $\pm$ 0.125 nT, the sampling resolution is the spin resolution (4.2 seconds). The CIS instrument observes the composition and three-dimensional distribution of ions between 0.002 to 40 keV in plasma, and the electrostatic electron analyzer designed to measure three-dimensional electron velocity distribution in the range of 0.7 to 32 keV (*Georgescu et al.*, 2005).

2.6 The Time History of Events and Macroscale Interactions during Substorms (THEMIS) Mission

The Time History of Events and Macroscale Interactions during Substorms (THEMIS) is a five-spacecraft mission with highly elliptical orbits with the objective to study

where and when substorms are generated in the magnetotail. The five spacecraft are identified by the first five letters of the alphabet. The initial orbits were designed to line up at apogee every four days, the three inner spacecraft (THEMIS-A, THEMIS-D, and THEMIS-E) had apogee around 10 Re, while THEMIS-C had an apogee of 20 Re and THEMIS-B had a apogee of 30 Re. The orbits of the spacecraft drift with an approximated period of 1 year which covers four phases. The phases are named after the location of the apogee of the spacecraft during each phase. The phases are dayside, dusk, tail, and dawn. The three inner spacecraft have maintained their orbits during the entire mission (*Frey et al.*, 2008; *Angelopoulos*, 2009). In July of 2011, THEMIS-B and THEMIS-C performed an insertion into lunar orbit. From that date they follow the Moon at around 60 Re from Earth, moving together in and out of the tail magnetosphere. The name of the new mission performed by these two spacecraft is Artemis (*Angelopoulos*, 2010).

These five identical spacecraft carry three instruments of special interest for this thesis. The fluxgate magnetometer has a resolution of ± 0.01 nT, while the time resolution is variable depending on the sampling mode being used at time of the observations. The low-resolution mode has a time resolution of 0.25 seconds, this mode is the most common. However, in some circumstances only the 3 second spin time resolution is available. The THEMIS spacecraft also carry both ion and electron electrostatic analyzers (iESA and eESA) to measure plasma from 0.003 eV to 30 keV. The observations of iESA and eESA are complemented with a Solid State Telescope (SST) that can measure ions and electrons within the energy range from 25 keV to 6 MeV.

2.7 The Van Allen (RBSP) Mission

The Van Allen Mission consists of two Radiation Belt Storm Probes (RBSP-A and RBSP-B) designed to study the Van Allen radiation belts with elliptic orbits with

apogee around 6 Re (*Spence et al.*, 2013). The spacecraft were launched on August 30, 2012 and were deactivated in 2019. The spacecraft had a highly elliptical orbit with a perigee of only 614 km, an apogee of 4.7 Re, and an inclination of 10.2°. In this thesis the spacecraft are used to observe the inner magnetosphere response to DPP. The instrument payload consisted of several instruments to measure waves, field, and plasma. The instruments used in this thesis for this mission are the EMFISIS, and HOPE. EMFISIS measures magnetic field with a resolution of ± 0.1 nT, and is also used to compute electron density with an error estimated in a 10% (*Fox and Burch*, 2014). The data from this instrument can be downloaded in three sampling time resolutions (0.016, 1, 4 seconds), the 1 second resolution was selected for use in this thesis. HOPE measures the ion and electron partial densities, H^+/He^+, and O^+/He^+ ratios for energies higher than 1 eV (*Funsten et al.*, 2013; *Nosé et al.*, 2020).

2.8 The Magnetospheric Multiscale (MMS) Mission

The Magnetospheric Multiscale (MMS) mission consists of four satellites orbiting Earth in a very close formation. The mission is designed to investigate equatorial magnetic reconnection. The main objective of the mission is to determine what causes reconnection in a collisionless plasma (*Burch et al.*, 2016). The constellation orbits in very close formation, then for large scale studies we consider the constellation as a single observation except when used for multi-spacecraft timing of a perturbation. The mission also has a very elliptical orbit that allows observations around 12 Re in the dayside and 25 Re in the nightside. The MMS orbit was designed to mutually complement with THEMIS mission, both missions orbits were planned to have apogees on opposite sides of Earth. This orbit configuration provides a large spatial scale by performing observations on opposite sides of the magnetosphere.

2.9 Global Ground-Based Magnetometer Network

The ground-based magnetometer data are collected independently by SuperMag (*Gjerloev*, 2012) and Intermagnet (*Kerridge*, 2001) projects. Both projects collaborate with multiple other projects of single and also arrays of ground-based magnetometer stations and standardize the data into a common coordinated system. The SuperMag data are given in North-East-Zenith (NEZ) magnetic coordinates. The time resolution available in SuperMag was improved to 1 second during the writing of this thesis. In effect, the magnetometer data used in Chapter IV has 1 minute as sampling time resolution during the whole period covered by this thesis. Meanwhile, the ground-based magnetometer data used in Chapter V and VI have 1 second sampling time resolution from 2012 to 2017. The Intermagnet data are given in Horizontal-Declination-Zenith coordinates and the data with 1 second resolution are available for the whole period under study. The data from Intermagnet are transformed into NEZ coordinates to match with the coordinate system used by SuperMag. Both projects use the International Association of Geomagnetism and Aeronomy (IAGA) which allows the identification of overlapping in terms of stations between the two projects, in which case the SuperMag data is prioritized.

The spatial density of the ground-based stations is larger in North America and Europe than in the rest of the world as it is shown in Figure 2.3. This has the effect of limiting the local time coverage of ground-signatures.

The technique used for the processing of the data is described in (*Gjerloev*, 2012). The data consist of the anomaly magnetic field after the removal of a baseline. The baseline is determined from a three step process that considers a daily baseline, a yearly trend, and a residual offset, eliminating the requirement of *quiet curves*.

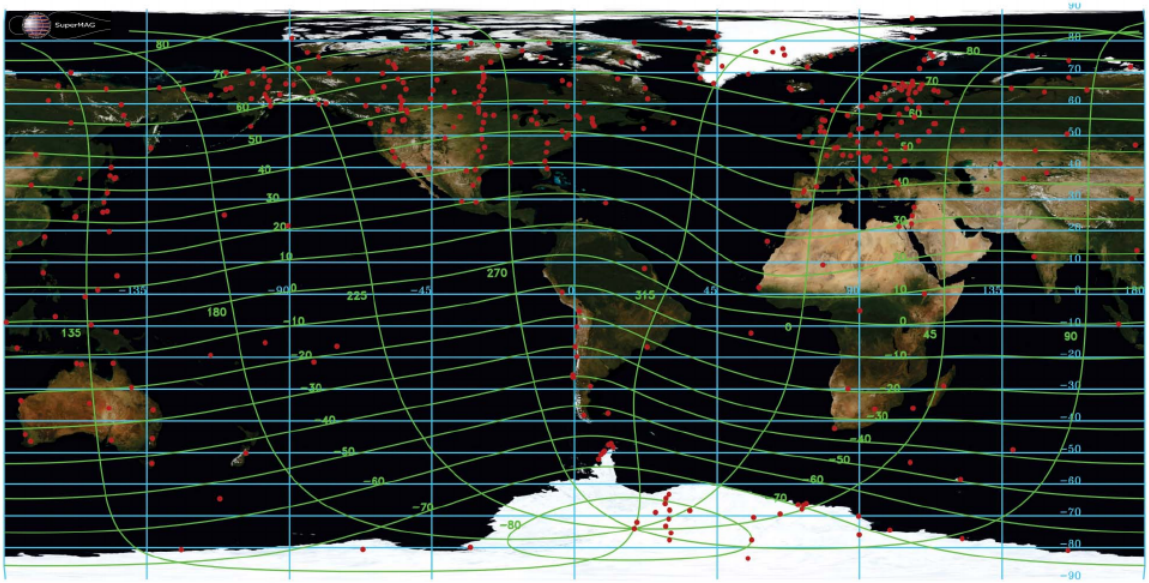

Figure 2.3: (Red) Location of ground-based magnetometer stations. (Green) grid of geomagnetic coordinates. (Cyan) grid of geographical coordinates. Some of the stations have only 1 minute time resolution, while other ones have 1 second time resolution. This is an approximate map as some of the stations may be out of service. Figure obtained from *Gjerloev* (2012).

2.10 Interplanetary Shock Database

The shock data are obtained from the Center for Astrophysics (CfA) catalogue website. The CfA catalogue provides shock parameters computed by eight different methods. These methods are developed under the assumption of a planar shock, in which case the Rankine-Hugoniot conservation relations are defined across the shock ramp. The methods are Magnetic Coplanarity, Velocity Coplanarity, Mixed Mode Normal 1, Mixed Mode Normal 2, Mixed Mode Normal 3, Rankine-Hugoniot with 8 Equations (RH08), Rankine-Hugoniot with 9 Equations (RH09), and Rankine-Hugoniot with 10 Equations (RH10) (*Wilson III et al.*, 2017).

The shock normals for the first five methods are given by:

Magnetic Coplanarity:

$$\hat{\mathbf{n}} = \pm \frac{(\langle \mathbf{B}_0 \rangle_{up} \times \langle \mathbf{B}_0 \rangle_{dn}) \times (-\Delta \mathbf{B}_0)}{|(\langle \mathbf{B}_0 \rangle_{up} \times \langle \mathbf{B}_0 \rangle_{dn}) \times (-\Delta \mathbf{B}_0)|} \tag{2.1}$$

Velocity Coplanarity:

$$\hat{\mathbf{n}} = \pm \frac{\Delta \mathbf{V}_{bulk}}{|\Delta \mathbf{V}_{bulk}|} \tag{2.2}$$

Mixed Mode Normal 1:

$$\hat{\mathbf{n}} = \pm \frac{(\Delta \mathbf{V}_{bulk} \times \langle \mathbf{B}_0 \rangle_{up}) \times \Delta \mathbf{B}_0}{|(\Delta \mathbf{V}_{bulk} \times \langle \mathbf{B}_0 \rangle_{up}) \times \Delta \mathbf{B}_0|} \tag{2.3}$$

Mixed Mode Normal 2:

$$\hat{\mathbf{n}} = \pm \frac{(\Delta \mathbf{V}_{bulk} \times \langle \mathbf{B}_0 \rangle_{dn}) \times \Delta \mathbf{B}_0}{|(\Delta \mathbf{V}_{bulk} \times \langle \mathbf{B}_0 \rangle_{dn}) \times \Delta \mathbf{B}_0|} \tag{2.4}$$

Mixed Mode Normal 3:

$$\hat{\mathbf{n}} = \pm \frac{-\Delta \mathbf{B}_0 \times (\Delta \mathbf{V}_{bulk} \times \Delta \mathbf{B}_0)}{|\Delta \mathbf{B}_0 \times (\Delta \mathbf{V}_{bulk} \times \Delta \mathbf{B}_0)|} \tag{2.5}$$

While these methods have been constantly improving during the last decades, they still face challenges to accurately compute the shock inclination angles in some circumstances. The accuracy of the shock speed, and the distribution of density points on both sides of the shock can generate important differences in the calculation of the shock parameters. In some of the events analyzed in this thesis we observed important differences in the shock parameters even when they are computed with similar methodologies such as RH08, RH09, and RH10.

Currently the most popular methods are based on the solution of RH08, RH09, and RH10 that minimizes the χ^2 merit function (*Viñas and Scudder*, 1986; *Szabo*, 1994; *Koval and Szabo*, 2008). *Viñas and Scudder* (1986) developed a method that use a reduced set of 8 Rankine-Hugoniot conservation equations. The variables that

represent the conservation constant correspond to the mass flux (G_n), normal magnetic field (B_n), tangential momentum flux ($\mathbf{S}_t$), and tangential electric field ($\mathbf{E}_t$). Years later, *Szabo* (1994) extended the method in order to use conservation of normal momentum flux (S_n), and energy density (ϵ), taking advantage of the currently more common plasma temperature observations performed by spacecraft located in the solar wind. This method uses equation (2.6) to obtain a expression of the shock bulk speed that can be substituted in other jump condition, removing this unknown quantity from the system. *Koval and Szabo* (2008) introduces a modification of the technique of *Viñas and Scudder* (1986) with a simultaneous determination of the shock normal direction, and uses the 10 ideal MHD Rankine-Hugoniot conservation equations. These equations in a spacecraft frame of reference are

$$\Delta[G_n] \equiv \Delta[\rho(V_n - V_S)] = 0 \tag{2.6}$$

$$\Delta[B_n] \equiv \Delta[\mathbf{B} \cdot \hat{\mathbf{n}}] = 0 \tag{2.7}$$

$$\Delta[\mathbf{S}_t] \equiv \Delta\left[\rho(V_n - V_S)\mathbf{V}_t - \frac{B_n}{\mu_0}\mathbf{B}_t\right] \tag{2.8}$$

$$\Delta[\mathbf{E}_t] \equiv \Delta[(\hat{\mathbf{n}} \times \mathbf{V}_t)B_n - (V_n - V_S)(\hat{\mathbf{n}} \times \mathbf{B}_t)] = 0 \tag{2.9}$$

$$\Delta[S_n] \equiv \Delta\left[P + \frac{B_t^2}{2\mu_0} + \rho(V_n - V_S)^2\right] = 0 \tag{2.10}$$

$$\Delta[\epsilon] \equiv \Delta\left[\rho(V_n - V_S)\left(\frac{(\mathbf{V} - V_S\hat{\mathbf{n}})^2}{2} + \frac{\gamma}{\gamma - 1}\frac{P}{\rho} + \frac{B^2}{\mu_0\rho}\right) - \frac{B_n(\mathbf{V} - V_S\hat{\mathbf{n}}) \cdot \mathbf{B}}{\mu_0}\right] = 0. \tag{2.11}$$

2.11 Data Source and Format

The data are obtained in Common Data Format (CDF; https://cdf.gsfc.nasa.gov/), Network Common Data Form (NetCDF; *Rew and Davis* (1990)) and ASCII files. All the satellite data except GOES mission data were obtained from the CDAWeb (http://www.cdaweb.sci.gsfc.nasa.gov). The CDAWeb also provides 1 minute resolution OMNI data, which includes combined solar wind data parameters collected by ACE and WIND spacecraft. The SYM-H index is also obtained from OMNI. Most of the magnetosphere observations come from the GOES satellites. GOES magnetic data are found in the National Center for Environmental Information database (https://ngdc.noaa.gov/), whose files are in NetCDF format. The ground-based magnetometer observations come from a variety of observatories accessed through SuperMag (http://supermag.jhuapl.edu/) and Intermagnet (http://www.intermagnet.org) available in ASCII format. All the data used and created (including data found in every figure) for this thesis are included in a package of data deposited in the Deep Blue Data repository from the University of Michigan as an effort to improve reproducibility of our results. The DOI number from each package of data is located in the Data section of their respective chapter.

2.12 Data Retrieval and Management

The large time period covered and the amount of spacecraft used are convenient for systematic studies in the magnetosphere, but presents a challenge from the perspective of data retrieval and management.

For this thesis I developed an extensive MatLab library with the objective of automatically downloading and pre-process the solar wind and spacecraft data. First, *get_data.m* function retrieves directly from the CDAWeb solar wind data from ACE and WIND spacecraft in a combined data product called *OMNI*. Then, the code reads

these files using the CDF MatLab libraries provided by the SPDF from the Goddard Space Flight Center. The methodology described in the following chapter is applied to the solar wind in order to detect events of interest. After the identification of the event of interest is finished, the same *get_data.m* function is used to search and extract the highest quality level data products and the highest time resolution available for each one of the spacecraft.

The data files obtained are stored in a local directory with the same structure used in the CDAWeb, this provides flexibility to add new instruments to the library without adding complications in the managing of the data.

As every mission has their own data characteristics, all of them have the *read_???.m* (where "???" is a mission and spacecraft identifier). These functions pre-process and standardize the data so the returned values have all the same format and can be compared between them. The functions automatically manage several common issues related to the collection of data, such as removing the wrong values, detect gaps, and fill short length gaps with simple linear interpolation or cubic splines methods, or merge files when the event occurred near midnight.

The ground-based magnetometers are processed in a similar manner. During the time of collection of data, only the Intermagnet mission allowed automatic downloads while the data from SuperMag had to be downloaded manually for each event. Fortunately, at the time of writing of this thesis, new tools in the SuperMag website allow automatic download through Python, MatLab, and IDL. The SuperMag, and Intermagnet data are broadly standardized. The data for each event was stored in its original format, but new *.mat* (from MatLab) files were also generated for each event. Every ground-based event file includes the event identification number, universal time, station IAGA code, geographic coordinates, magnetic coordinates, local time, and the magnetic field data. The pre-proccessing consisted in verification, gap filling, and rotation of coordinates of some of the InterMagnet stations.

Every station and ground-based magnetometer station was plotted and saved automatically for verification and analysis. In both cases (space, and ground), the verification process consisted in the random selection of multiple spacecraft and ground-based stations figures and compare them with the survey plots provided by CDAWeb, SuperMag, and Intermagnet websites.

CHAPTER III

Methodology

3.1 Introduction

The HSO consists of independent missions orbiting multiple regions of the magnetosphere that have been operative for different periods of time. With the exception of ACE and WIND spacecraft that are permanently located in the L_1 Lagrange point and monitor the solar wind, all the spacecraft are in constant movement between regions of the magnetosphere and the solar wind. In effect, the configuration of the spacecraft location changes in time that are more favorable for the study of certain regions over others. Similarly, the spatial density of ground-based magnetometers is higher in North American and Europe than in the other continents.

The methodology of this thesis is designed to detect solar wind DPPs and analyze the magnetic waves and disturbances in the magnetosphere using the HSO and ground-based magnetometers. One of the major benefits of the HSO for the study of the magnetosphere is the large amount of data available for analysis. However, the employment of the HSO as a single observatory presents two major challenges: (1) the events of interest are function of the solar wind conditions, but also function of the spatial distribution of the constantly moving spacecraft around the magnetosphere, and Earth's rotation; this introduces an observational bias because we can only observe in the locations where spacecraft are located; (2) the magnetometer is

the only instrument shared by all spacecraft, limiting the capacity to compare similar solar wind DPPs events when a different mission is located in the same region to only magnetic field vector observations.

If we consider that average solar wind travels at 450 km/s it would take ∼16 minutes from the dayside magnetosphere to reach 60 Re in the tail, which is the distance of the current most distant spacecraft (ARTEMIS). Meanwhile, the travel time of a disturbance in the magnetopause takes 1-2 minutes to reach the Earth's surface. Then we can safely say the time scale of events of interest for this study is shorter than 20 minutes. In consequence, the methodology for detection of events of interest must be in the place identify solar wind DPPs during times where the number and spatial distribution of the spacecraft allows the study of different aspects of the dynamics of the magnetosphere.

3.2 Detection of Solar Wind Dynamic Pressure Pulses

I developed and applied an algorithm to automatically detect potential DPP events during the interval of time between 2007 and 2017. The algorithm searched for DPPs that occur during northward IMF and the set of conditions defined are focused on detection of clear, large amplitude events. False positive events are removed by visual inspection of the events. This is necessary as the modeled propagation time for ACE and WIND data is not always accurate, and also data gaps can make it difficult to set conditions that apply correctly to all the data. The conditions are: (1) the increase of the SYM-H index must be larger than 6 nT; (2) the rise time must be in less than 3 minutes; (3) the SYM-H index increase must occur during northward IMF that lasts for at least 3 minutes (this identified 198 events); (4) DPPs occurrence confirmation in each event by visually inspecting the SYM-H index, solar wind dynamic pressure, interplanetary magnetic field, solar wind flow speed, and the magnetic field for each satellite.

Additional conditions are added in Chapters IV, V and VI to focus on the propagation of the dynamic pressure pulse, and dayside wave propagation. These additional conditions are respectively explained in the methodology section of each chapter.

The IMF orientation is the most important condition implemented in the methodology of this thesis. The magnetospheric response to DPPs under southward Bz IMF conditions differs from the response under northward Bz IMF (*Dungey*, 1961; *Trattner et al.*, 2007). During southward Bz IMF, the DPPs compress the dayside magnetosphere in addition to enhancing low latitude magnetic reconnection, increasing the influence of flux transfer events (FTEs) and substorms on the topology of the magnetosphere. FTE signatures at the magnetopause and ground are similar to the signatures generated by DPPs (*Sibeck*, 1990). However, during northward Bz IMF the magnetosphere reacts more simply to DPPs, majors storms are unlikely, the magnetosphere is commonly compressed at all local time sectors (*Zuo et al.*, 2015), and the electromagnetic energy coupling between the solar wind and the magnetosphere during northward IMF is only about 20% than for southward IMF (*Lu et al.*, 2013). An example of this difference is shown in Figure 3.1 where are shown the magnetic field horizontal component for two different events measured by the same ground-based magnetometer located at Sanikiluaq station(T31, MLAT: 66.3, MLON:-1.9). The figure on the top correspond to the observations made on May 21, 2012 after the impact of a DPP during northward IMF. The figure on the bottom correspond to the observations made on September 7, 2017 after the impact of a DPP during southward IMF. In both cases the observations are made in the afternoon local time sector. It is noticeable how the magnetic disturbance generated by the DPP's compression is easily distinguishable due to the calm magnetospheric conditions previous and during the event, in contrast with the response observed by the same station to a DPP during southward IMF where the large magnetospheric disturbances make impossible the identification of the first wave resulting from the compression.

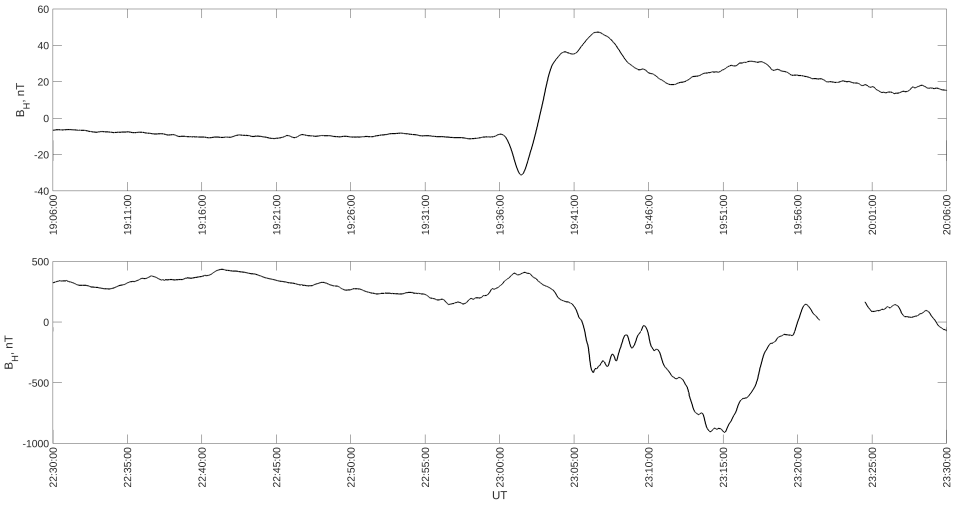

Figure 3.1: Local magnetic field horizontal component at Sanikiluaq (MLAT: 66.3, MLON:-1.9) ground-based magnetometer station. (Top) Magnetic response on May 21, 2012 during northward IMF at the afternoon local time sector. The signature of the preliminary reverse impulse is easily recognizable as the decrease followed by an increase of the horizontal component. (Bottom) Magnetic response on September 7, 2017 during southward IMF at the afternoon local time sector. The preliminary reverse impulse nor the main impulse can be recognized due to the high variability resulting from the magnetospheric complex dynamics under southward IMF.

3.3 Multi-Spacecraft Timing

This technique can be used when the same boundary or perturbation crosses four or more spacecraft. If the disturbance crosses four spacecraft the solution is unique. If the boundary crosses more than four spacecraft the system is overdetermined and can be solved by least-squares method. If these conditions are accomplished the normal to the boundary can be determined by timing the disturbance crossed by each spacecraft. Since,

$$(\mathbf{V}_b t_{\alpha\beta}) \cdot \hat{\mathbf{n}} = \mathbf{r}_{\alpha\beta} \cdot \hat{\mathbf{n}} \tag{3.1}$$

where $r_{\alpha\beta}$ is the vector distance and $t_{\alpha\beta}$ the time difference taken by the boundary to reach from α to β. If we consider 4 spacecraft, the solution for the normal to the boundary is found by obtaining the solution to the following system:

$$\begin{pmatrix} \mathbf{r}_{12} \\ \mathbf{r}_{13} \\ \mathbf{r}_{14} \end{pmatrix} \cdot \frac{1}{V_b} \begin{pmatrix} \mathbf{n}_x \\ \mathbf{n}_y \\ \mathbf{n}_z \end{pmatrix} = \begin{pmatrix} \mathbf{t}_{12} \\ \mathbf{t}_{13} \\ \mathbf{t}_{14} \end{pmatrix} \tag{3.2}$$

This method assumes that the spacecraft are not coplanar, then if the spacecraft are too far away from each other that condition may break down. This method would also fail with non-stationary coordinate systems, like GSE. However, the speed of the disturbances analyzed in this thesis are much faster than the speed of the spacecraft meaning that the coordinate system can be considered as stationary.

3.4 Coordinate Systems

The standard coordinate system used in this thesis is the GSE. This system has the X coordinate centered in the Earth and positive direction points to the Sun. The Z axis is perpendicular to the ecliptic plane of the Earth's orbit around the

Sun (towards geographic north at equinox). The Y axis is perpendicular to both to complete the system. All the spacecraft locations and observations were transformed into this coordinates system.

The other coordinated system used in this thesis are the Altitude Adjusted Corrected Geomagnetic (AACGM) coordinates. The AACGM coordinates were designed for comparison of magnetically conjugated ground-based observations in both hemispheres. The magnetic ground coordinates are determined using the International Geomagnetic Reference Field (IGRF) and numerically traced to the equator. However, this coordinate system is only valid up to 2000 km above the surface and cannot be used to find the conjugated points at ground for the spacecraft from the HSO (*Shepherd*, 2014). In Chapters IV and V these coordinates are used only to determine the magnetic location of the magnetometer stations at Earth's surface, and determine latitudinal and local time arrays of ground-based magnetometers that could help to characterize the magnetic response at ground. Nevertheless, the methodology applied in Chapter VI requires the tracing from one spacecraft to ground. In that situation, I use Tsyganenko T96 magnetospheric model to trace the magnetic field from the spacecraft to ground.

Tsyganenko models (e.g. T89, T96, TS01, TS05, TA15) are semi-empirical magnetospheric models. These models have been under constant review and improve with every addition of newer spacecraft magnetospheric observations. In this thesis these models are implemented using the GEOPACK library for IDL and Python 3. These libraries are adaptations from the original Fortran codes written by Dr. Nikolai Tsyganenko, that combine the IGRF and Tsyganenko models to trace the observations between conjugated observations in space and ground (*Tsyganenko*, 1987).

The magnetic field vector data from the ground-based magnetometers stations are transformed to the local NEZ coordinate system when necessary. The origin of this coordinate system is centered in each magnetometer station. The North coordinate is

horizontally towards the AACGM north. The Zenith coordinate as its name indicates is perpendicular to the surface towards the zenith. The East coordinates completes the system.

CHAPTER IV

Global Magnetosphere Response to Solar Wind Dynamic Pressure Pulses

4.1 Introduction

The solar wind is the main driver of Earth's magnetospheric structure and activity and determines the shape, location and dynamics of the magnetopause. Disturbances such as solar wind DPPs, modify the size of the magnetosphere, while the IMF strength and orientation determine how the solar wind disturbances affect the state of the magnetosphere (*Nishida*, 1983; *Sibeck et al.*, 1991; *Yu and Ridley*, 2009). DPPs are characterized by an abrupt and large change of the solar wind density and/or velocity. These changes can be due to interplanetary discontinuities or shocks due to CMEs, CIRs or local perturbations in the solar wind. These disturbances generate a compression that is recorded by ground-based magnetometers as sudden impulses (SIs), or sudden storm commencements (SSCs) if they are followed by a geomagnetic storm. SIs and SSCs have been widely studied from multiple perspectives (*Araki*, 1977; *Kokubun*, 1983; *Taylor*, 1969; *Huttunen et al.*, 2005). The magnetospheric

Parts of this chapter were published in: Vidal-Luengo, S. E., & Moldwin, M. B. (2021). Global magnetosphere response to solar wind dynamic pressure pulses during northward IMF using the heliophysics system observatory. Journal of Geophysical Research: Space Physics, 126, e2020JA028587.

response to DPPs under southward Bz IMF conditions differs from the response under northward Bz IMF (*Dungey*, 1961; *Trattner et al.*, 2007). During southward Bz IMF, the DPPs compress the dayside magnetosphere in addition to enhancing low latitude magnetic reconnection, increasing the influence of FTEs and substorms on the topology of the magnetosphere. FTE signatures at the magnetopause and ground are similar to the signatures generated by DPPs (*Sibeck*, 1990). However, during northward Bz IMF the magnetosphere reacts more simply to DPPs, majors storms are unlikely, and the magnetosphere is commonly compressed at all local time sectors (*Zuo et al.*, 2015). The DPPs' compression generate fast-mode compressional waves that propagate through the magnetosphere faster than the magnetosheath flow, creating a bulge outward just before the compression associated with the DPP (*Sibeck*, 1990).

The response of the magnetosphere to DPPs has been studied in different local time sectors and regions. *Borodkova et al.* (2005) analyzed more than 300 events comparing solar wind observations by INTERBALL-1 and geosynchronous GOES satellites. They found that increases (decreases) in the dynamic pressure always result in increase/compression (decrease/decompression) in the geosynchronous magnetic field. Later, *Borodkova et al.* (2008) compared different events with three dimensional MHDs simulations, obtaining congruent results. Similarly, *Lee and Lyons* (2004) and *Sanny et al.* (2002) studied the geosynchronous magnetic response to DPPs during conditions of southward and northward Bz IMF. *Lee and Lyons* (2004) found that an increase in the dynamic pressure always leads to compression on the dayside. However, the nightside response shows a dependency on the IMF Bz direction. The nightside sometimes shows a dipolarization-like magnetic signature, but during northward IMF most of the cases show a compression. *Sanny et al.* (2002) found similar results, but also recognized that compression amplitudes are greater for northward IMF than for southward IMF.

The disturbances carried by the solar wind can also excite different types of ULF wave activity in the magnetosphere, such as Pc5 (periods between 150-600 seconds) and electromagnetic ion cyclotron (EMIC) waves (*Claudepierre et al.*, 2010; *Takahashi and Ukhorskiy*, 2007; *Usanova et al.*, 2012; *Zhang et al.*, 2010). In other cases, the magnetosphere can act as a low-pass filter for the disturbances. *Archer et al.* (2013) show how sharp magnetosheath DPPs can induce compressional and toroidal modes and because each L-shell has their own oscillation mode in the ULF range, each L-shell partially filters high frequencies, in this way the whole magnetosphere acts as a low-pass filter. ULF waves play an important role for the magnetosphere-ionosphere coupling through particle-wave interactions (*Elkington et al.*, 1999), and are also a mechanism to remotely study the magnetosphere (*Ables and Fraser*, 2005; *Chi and Russell*, 2005; *Troitskaya and Bolshakova*, 1988).

The study of the magnetotail is more complex due to the high apogee orbits of most of the missions available to perform in situ observations. In order to traverse the magnetotail, satellites need to be placed in very high and often very eccentric orbits, which allow them to perform only a few months of magnetotail observations each year. Despite this, there are several studies of the impact of DPPs in the tail. *Petrinec and Russell* (1993) developed an empirical model for the near-Earth magnetotail, using simultaneous observations of IMP-8 in the solar wind and magnetotail measurements performed by International Sun-Earth Explorer 1 (ISEE-1). Similarly, *Collier et al.* (1998) used IMP-8 and *Yao et al.* (2010) used one of the Double Star mission satellite, TC-1 to observe the tail response to DPPs during northward and weak southward IMF, showing a direct relationship between the solar wind dynamic pressure and tail magnetic compressions. *Huttunen et al.* (2005) used observations made by Cluster to study tail lobe SIs, finding that the disturbances were moving at speeds of order of the solar wind rather than Alfvén speed, which implies that the tail lobe SIs are generated by a compression of the magnetotail due to magnetosheath compression, instead of the

transfer of magnetic flux from day-side through MHD waves. Similarly, *Moldwin et al.* (2001), used IMP-8 to show that DPPs can also generate a tailward moving South-then-North compression region signature, which are usually thought of as signatures of earthward propagating flux ropes (*Moldwin and Hughes*, 1994). The magnetospheric impact of DPPs can also be observed from ground magnetometer stations. *Russell and Ginskey* (1993, 1995) and *Russell et al.* (1994) showed the response to SIs at different latitudes, while *Slinker et al.* (1999) and *Kataoka et al.* (2002) showed that magnetic signatures resulting from Traveling Convection Vortexs (TCVs) resulting from Field Aligned Currents (FACs) intensified by the magnetospheric compression due to DPPs. Similarly, Magnetic Impulse Events (MIEs) identified by *Lanzerotti et al.* (1991) as possibly intensification of FACs were studied with ground-based observations. Other studies showed the relationship between MIEs occurrence and perturbations in the solar wind such as changes in the IMF and dynamic pressure (*Konik et al.*, 1994; *Lanzerotti et al.*, 1990).

Due to the lack of studies that observed multiple events that had simultaneous observations in different local time sectors and regions of the magnetosphere, previous studies were unable to observe the global magnetosphere response during DPPs. In this chapter we use eight different satellite missions and scores of ground-based magnetometers from middle to high latitudes in order to examine the global magnetosphere response to DPPs during northward IMF Bz conditions. Under these conditions, the magnetosphere acts as a closed "cavity" and reacts to solar wind DPPs more simply than during southward IMF conditions (*Tsurutani and Gonzalez*, 1995). The simultaneous observations of GOES, Geotail, Cluster, THEMIS, Van Allen Probes and MMS missions as part of the HSO make possible the identification and tracking of propagating or traveling signatures, such as compression regions and waves, which can travel at different speeds and through different paths. Simultaneous ground magnetometer data are used to identify the ionospheric and field-aligned

current response and signatures to DPPs.

The second section contains the main characteristics of the data used in this chapter. The third section contains the methodology, where the criteria for the selection of events and identification of signatures are explained. It also describes the sources of data and the main characteristics of the missions used for this chapter. In the fourth section some statistical results are presented in order to set a context for the events shown in section four. The fifth section contains an extensive review of an example event. The final sections contains the Results, Discussion and Conclusion sections respectively.

4.2 Data

The major part of the data consists of spacecraft and ground magnetic field vector measurements from February 2007 to December 2017. However, depending on the availability, plasma observations from spacecraft are also used to support the interpretation behind each signature observed. The characteristics of the instrumentation and the digital source and format are described in Chapter II. The data used and generated for this chapter was deposited in the University of Michigan Deep Blue database (DOI: https://doi.org/10.7302/keks-rg16).

4.2.1 Satellite Overview

The HSO satellite constellation consists of several missions. GOES-13 and GOES-15 provide observations of perturbation generated by the DPP in the inner magnetosphere (*Singer et al.*, 1996). Van Allen Mission consist of two Radiation Belt Storm Probes (RBSP-A and RBSP-B) that study the Van Allen radiation belts with elliptic orbits with apogee around 6 Re (*Spence et al.*, 2013). The Cluster II (hereafter just Cluster) mission consists of four spacecraft that as a result of their relative small spatial separation among them, are usually considered a single observation (however,

we make use of the constellation to determine front orientations for several events when Cluster was in the solar wind). Cluster satellite have highly elliptical nearly polar orbits with an apogee around 20 Re. The THEMIS is a five-satellite mission with highly elliptical orbits to study magnetic reconnection in the magnetotail. Two of the satellites broke the formation and were inserted into Lunar orbit (*Angelopoulos*, 2009) are now called THEMIS-ARTEMIS. The MMS Mission consists of four satellites orbiting Earth in a very close formation, we consider the constellation as a single observation except when used for multi-spacecraft timing of a perturbation. The mission has a very elliptical orbit that allows observations around 12 Re in the dayside and 25 Re in the nightside. The combination of THEMIS and MMS orbits are used to explore day and night side simultaneously.

4.2.2 Ground Magnetometers Overview

The ground-based magnetometers correspond to multiple arrays of magnetometers around the world. The data are standardized by SuperMag to improve the access to the data. The data have 1-minute resolution. For this chapter, we selected all station above 60° of magnetic latitude. The spatial density of the ground-based stations are larger in the Americas and Europe than in the rest of the world. This has the effect of limiting the local time coverage of ground-signatures.

4.3 Methodology

We developed and applied an algorithm to automatically detect potential DPP events. The algorithm searched for DPPs that occur during northward IMF and the set of conditions defined are focused on detection of clear, large amplitude events. False positive events are removed by visual inspection of the events. This is necessary as the time shifting done to ACE and WIND data in the OMNI database, and also data gaps can make it difficult to set conditions that apply correctly to all the data.

The conditions are: (1) the increase of the SYM-H index must be larger than 6 nT; (2) the rise time must be in less than 3 minutes; (3) the SYM-H increase must occur during northward IMF that stay for at least 3 minutes (this identified 198 events) ; (4) DPPs occurrence confirmation in each event by visually inspecting the SYM-H index, solar wind dynamic pressure, IMF, solar wind flow speed, and the magnetic field for each satellite. During this final inspection, events with $\frac{\Delta P}{P} > 1$ (reducing the number of events to 104) and five or more satellites in the magnetosphere (previous to the DPP) that observe a clear signal that can be associated to the DPP (usually but not necessarily, due to previous calm conditions) were selected for final analysis. This signal could be an increase in the total magnetic field, sudden magnetic field rotation, or increase in wave the activity. The $\frac{\Delta P}{P}$ ratio is computed by dividing the difference between the maximum dynamic pressure after the DPP and the dynamic pressure immediately before the DPP, by the dynamic pressure immediately before the DPP. The main reason we use SYM-H index as indicator of possible DPP occurrence is because this index is obtained from ground-based magnetometers, which allow us to narrow down to a minute the interval where the DPP hits the magnetosphere, for any of the propagation modes proposed in literature (*Chi et al.*, 2001). Using these conditions a total of 37 events were identified, this event collection allows the identification of global magnetospheric patterns due to DPP propagation that could not be identified by using single observations and enables examination of conclusions made by statistical studies with simultaneous observations throughout magnetosphere. The conditions set favored the detection of events with large DPP during quiet conditions. Figure 4.1 shows the location of all satellites for the 37 events, using *Shue et al.* (1998) as reference for the magnetopause under nominal solar wind conditions. The list of the events is shown in Table 4.1. The locations of the satellite are mainly in the inner magnetosphere, but several spacecraft are in the solar wind, magnetosheath and the tail lobes, including THEMIS-B, C that made measurements of the far tail.

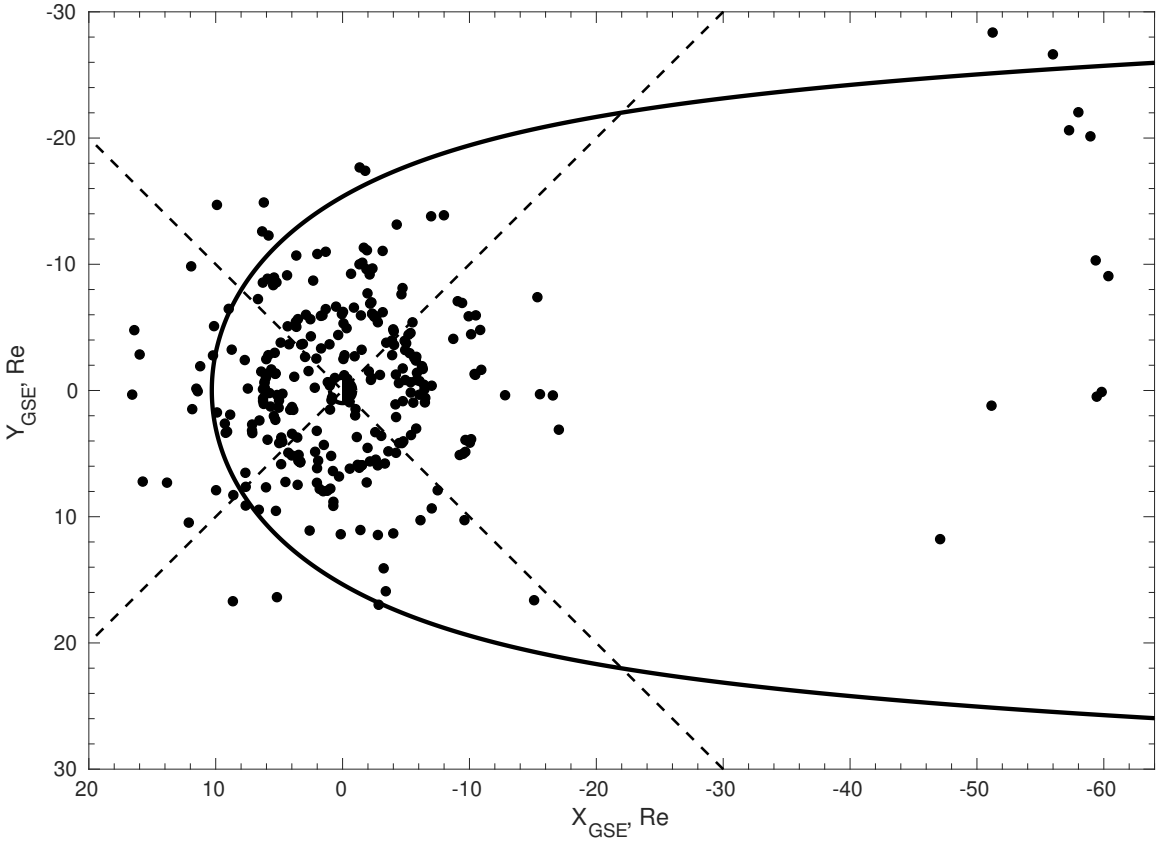

Figure 4.1: Satellite location during all the events. The dashed lines indicate four local times: midnight (21-03) LT, dawn (03-09) LT, noon (09-15) LT, dusk (15-21) LT. The magnetopause is drawn as reference using the model provided by (*Shue et al.*, 1998).

We examined the impact of the selection criteria with respect to the angle between the Earth's magnetic dipole axis and IMF of the selected events. We built histograms for the angle between IMF projected to the ZY (GSE) plane and the dipole axis. No major differences are found in the distribution of the angle between selected and non-selected events. This is probably due that our main selection criteria are events where the dynamic pressure change is large ($dP/P > 1$). As the effect of the dynamic pressure is likely larger than the angle between the dipole and the IMF, the potential influence of this angle was not captured.

The observations collected by satellites and ground-based magnetometer were classified by local time: dayside (9-15 LT), dusk (15-21 LT), midnight (21-3 LT), dawn (3-9 LT). Additionally the satellites were also classified by radial distance and region (inner magnetosphere, magnetosheath, solar wind, tail lobe). We group all the observations together in order to improve the spatial coverage and to have a better view of the global magnetospheric response. Simultaneously, we individually analyzed the events to directly track the DPP response at different regions in space and ground. We then determined the Time-Of-Flight (TOF) difference between the DPP hitting the dayside magnetosphere and each of the satellites to estimate speed of propagation of the perturbation through the magnetosphere. We then determined arrival time differences between the DPP hitting the dayside magnetosphere and each of the satellites to estimate the propagation speed. The arrival of the DPP to the dayside magnetosphere is determined by the satellite located in the dayside with the largest X_{GSE} coordinate, or by time where SYM-H index suddenly increases in case there are no satellites located on the dayside. The main uncertainty of this method results from the events where the DPP arrival to the magnetosphere is computed with the SYM-H (1-min resolution), also the direction and inclination of the DPP plays an important role in the computed TOF. The speed of propagation in the antisunward direction can tell us if the signature observed is directly due to the DPP traveling at

Event ID	Event date	IMF By	IMF Bz	IMF Bt	DPP speed	$\frac{\Delta P}{P}$	SI or SSC?
1	2011/02/18 01:30:00	0.9	4.0	5.7	-448	10.6	SSC
2	2011/06/05 05:55:00	-6.5	15.6	16.9	-544	2.8	N/A
3	2011/06/11 09:13:00	-4.5	6.0	7.6	-401	2.6	N/A
4	2011/08/04 21:53:20	-2.9	2.3	4.3	-398	4.0	SI
5	2011/10/05 07:36:37	3.8	3.4	5.2	-445	2.6	SI
6	2011/11/30 01:42:30	-3.2	5.8	6.9	-458	3.3	N/A
7	2012/01/24 15:00:05	-22.0	15.8	27.6	-625	7.6	SSC
8	2012/03/08 11:02:40	-0.3	9.2	10.4	-790	5.9	SSC
9	2012/04/23 03:20:20	5.8	1.3	5.9	-387	4.6	SSC
10	2012/05/21 19:35:35	-0.7	1.2	1.8	-388	3.2	SI
11	2013/01/19 17:32:00	2.3	2.9	4.6	-430	2.1	SI
12	2013/02/16 12:08:15	9.4	4.0	10.2	-388	2.0	SI
13	2013/03/18 06:12:00	-1.9	5.7	8.0	-572	1.6	N/A
14	2013/04/14 09:16:10	7.2	6.9	11.0	-520	1.3	N/A
15	2013/05/16 15:45:00	2.0	1.1	3.5	-410	1.4	N/A
16	2013/07/09 20:51:50	5.5	8.6	10.2	-415	3.4	SI
17	2013/12/01 13:07:20	1.8	7.2	8.2	-479	2.7	N/A
18	2013/12/13 13:23:00	-2.5	0.4	2.7	-320	2.8	SI
19	2014/01/09 20:10:20	-5.4	4.0	7.5	-460	3.2	SI
20	2014/03/20 10:16:30	-7.7	3.1	8.7	-347	1.6	N/A
21	2014/04/20 10:54:50	-0.6	8.2	8.3	-554	5.7	SSC
22	2014/05/03 17:47:15	-2.3	2.1	3.4	-330	1.4	SI
23	2014/06/07 16:51:45	-6.1	5.6	10.3	-420	4.7	SSC
24	2014/07/14 14:31:05	-1.9	8.3	8.9	-365	1.3	SI
25	2014/09/12 15:54:00	7.6	3.0	8.2	-600	9.1	SSC
26	2014/12/23 11:15:33	-11.5	3.3	13.5	-410	4.7	SI
27	2015/01/06 20:22:15	-3.8	7.7	8.6	-485	1.9	N/A
28	2015/01/07 06:16:00	1.8	7.4	7.9	-480	1.7	SSC
29	2015/03/17 04:44:00	10.7	15.6	19.0	-551	3.5	SSC
30	2015/03/31 08:32:10	-5.8	2.1	7.2	-360	2.3	SI
31	2015/06/25 05:30:00	-1.3	4.9	6.6	-652	1.4	N/A
32	2015/08/15 08:28:00	7.7	4.9	10.5	-450	2.2	SSC
33	2015/09/20 06:03:30	8.7	3.4	9.5	-498	2.3	SSC
34	2015/11/20 06:50:00	-4.6	2.2	5.3	-382	4.6	N/A
35	2017/07/02 20:53:30	-2.1	3.9	6.7	-435	1.1	N/A
36	2017/09/06 23:43:30	-3.4	2.5	4.7	-590	6.9	SSC
37	2017/11/25 00:33:55	2.5	4.4	5.4	-440	1.9	SI

Table 4.1: Events found between 2007 and 2017 (inclusive) that meet the criteria described in the methodology section. IMF values are in nanoTesla and DPP speed in km/s.

solar wind speed or if it is due to the propagation of MHD waves.

During each event, several individual satellite observations are made. In some cases we group all the events in order to have a bigger number of single observations. In 82% of the individual satellite observations the arrival of the DPP compression to the satellite is observed as a step-like function. These step-like signals are the main indicator used in this chapter to establish the arrival of the magnetic compression to each satellite, which is used to compute the propagation speed in the antisunward direction. We also performed wavelet, and Fourier power spectral density (PSD) analysis of all satellite and ground-based observations. In order to make this possible we applied a high-pass filter to the magnetic field to try to reduce the impact of the step-like function component in the analysis. In the case of the PSD, we also divided the signal into two parts (before and after disturbance arrival) to detect ULF waves that are generated by the DPP. In both cases, the analysis was performed to detect waves in the Pc5 range.

In the case of the ground-based magnetometers, the 1-min resolution of the data limits the analysis capabilities of PSD. In addition, we divided each one of the magnetometer observations in two parts, one before the DPP arrival and one after the DPP arrival. We adjusted a third degree polynomial to each part and used it as reference to compute the root-mean-square-deviation (RMSD) which gives an estimation for the total amount of variability observed by the magnetometer as result of the DPP.

4.4 Event Characterization

The solar wind and IMF conditions for the 37 DPP events are similar due to our selection criteria. All the events occur during northward IMF Bz, and all generate a compression in ground magnetometer data observed as an increase in SYM-H index over an average rise time of 6 minutes. Figure 4.2 summarizes the main characteristics

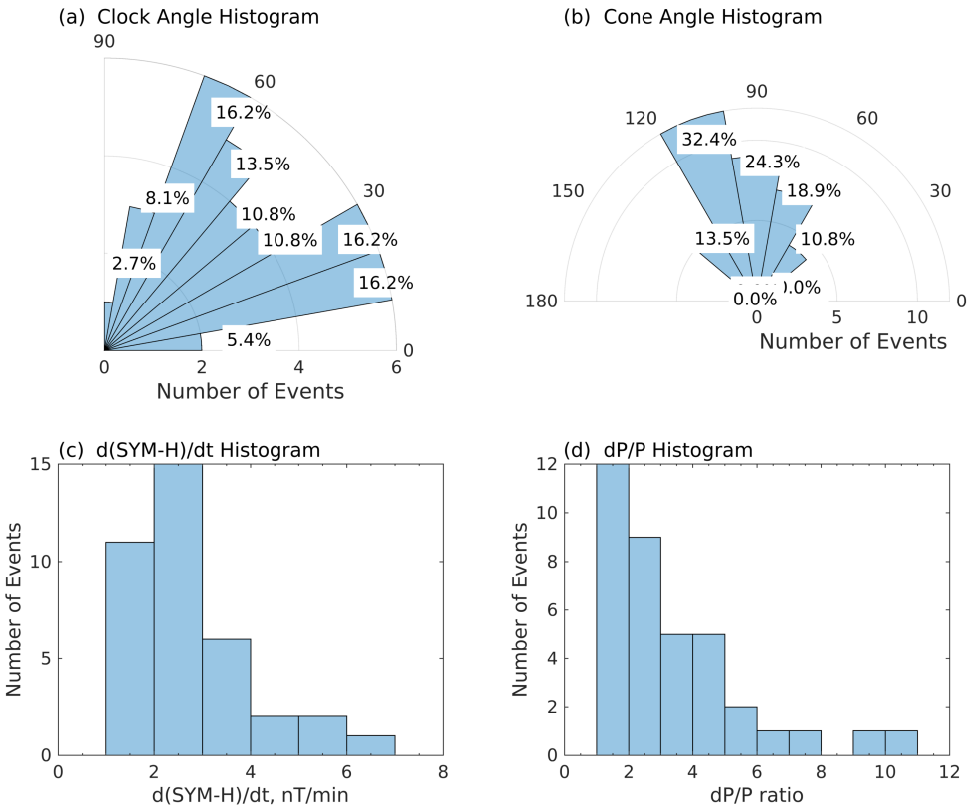

Figure 4.2: Event summary histograms. (a) Clock Angle. (b) Cone Angle. (c) d(SYM-H)/dt. (d) $\frac{\Delta P}{P}$.

of the events. The clock angle ($arcos\left(\frac{B_y}{\sqrt{B_y^2+B_z^2}}\right)$) is always between 0° and 90°, the cone angle ($arcos(\frac{B_x}{B})$) is always between 40° and 140°.

The events are classified by the $\frac{\Delta P}{P}$ ratio and the events that had large pressure ratios also had large increases in SYM-H. The d(Sym-H)/dt mean is 2.7 nT/min and the median is 2.3 nT/min. This indicates that all large solar wind DPP during northward IMF have large compression signatures on the ground and are therefore ideal candidates to study the non-storm-time magnetospheric response to rapid and large solar wind drivers. We compared our list of events with the Space Weather Database Of Notifications, Knowledge, Information (DONKI) catalogue (https://ccmc.gsfc.nasa.gov/donki/) and found that 18 of the events are CMEs impacting the Earth's magnetosphere.

Based in "Observatori de l'Ebre" catalogue (http://www.obsebre.es/en/), 13 of the events were SIs, and 12 SSCs. However, the capability to take advantage of the big events finally depends on the amount and distribution of HSO satellites throughout the magnetosphere. The next section presents one of the 37 events as "typical" best case example that highlights signatures seen in all the cases. The other events differ due to the location of the satellites and the size (dP/P) of the DPP, with smaller amplitude events have smaller magnetosphere and ionosphere signatures.

4.5 Event on September 6, 2017

In this section we show one event as example of the 37 events analyzed. This event occurs at the beginning of a very active period of the Sun (*Scolini et al.*, 2020), that developed geomagnetic storms and their effects in different regions of the magnetosphere. However, the immediate hours before this event were calm with northward IMF. At 23:43 UT an interplanetary shock driven by an ICME compressed the magnetosphere and generated magnetic perturbations which propagation we were able to track at different sectors and regions of the magnetosphere. Other events, especially the events with large dP/P ratios are very similar and therefore are not presented. However, figures are available in the dataset deposited in Deep Blue which DOI number given in the data section of this chapter.

For this event there are a total of six satellite missions (consisting of 12 satellites), 62 ground-based magnetometer stations (above 60° of magnetic latitude) with available data. For many of the events, Cluster, MMS and some of the THEMIS spacecraft travel very close to each other and therefore are treated as single observation points. However, in these circumstance the close spacecraft formations are used to assess propagation velocity. In this particular event, the spacecraft configuration allows the study of the global scale and also the small scale using Cluster and MMS. Figure 4.3a shows the location of the spacecraft constellation during this event. The magne-

tosphere structure is obtained with Tsyganenko T89 model, and the magnetopause is drawn using *Shue et al.* (1998) model. The solar wind OMNI data correspond to ACE and WIND data propagated to the bow shock and the propagation uncertainty depends of the solar wind conditions. In order to improve the estimation for the DPP arrival to the magnetopause, it was determined using the SYM-H index, the accuracy of the SYM-H for the arrival estimation of the DPP is higher than the OMNI data. Figure 4.3b-f shows that the solar wind conditions previous to the DPP arrival are steady, the IMF Bz is constantly positive but low amplitude, and the solar wind flow speed is 480 km/s.

The propagation of the disturbance was tracked using the magnetic field instruments of each one of the spacecraft. Figure 4.4 shows the magnetic field magnitude of 11 spacecraft and the compression observed by each of them due to the propagation of the traveling magnetic cloud. The first plot shows the closest spacecraft to the Sun, while the last one shows the furthest spacecraft to the Sun. Note that a compression signature is observed at all spacecraft (except Cluster, explained below) and the timing of the observations are consistent with a signature propagation from the dayside magnetopause through the magnetosphere.

The first sign of the DPP arrival is given by the magnetospheric compression and wave activity observed by THEMIS-D $(11.5, 0, -1.0)_{GSE}$ at 23:43:30 UT (shown in Figure 4.5), located at the dayside of the outer magnetosphere. The solar wind dynamic pressure before the DPP was around 0.9 nPa and the peak in the DPP was around 7.5 nPa $\frac{\Delta P}{P} \simeq 6.9$ and the IMF is $(2.0, -5.9, 4.1)_{GSE} nT$, the solar wind flow speed observed by ACE is around 600 km/s, while WIND detects a flow speed of 580 km/s. The DPP induces an increase in SYM-H of 26 nT.

Dayside: The dayside response to the solar wind pressure pulse is observed by THEMIS-A, THEMIS-D, THEMIS-E, GOES-15, and Van Allen Probes. All of them observe the magnetic compression generated by the solar wind pressure pulse.

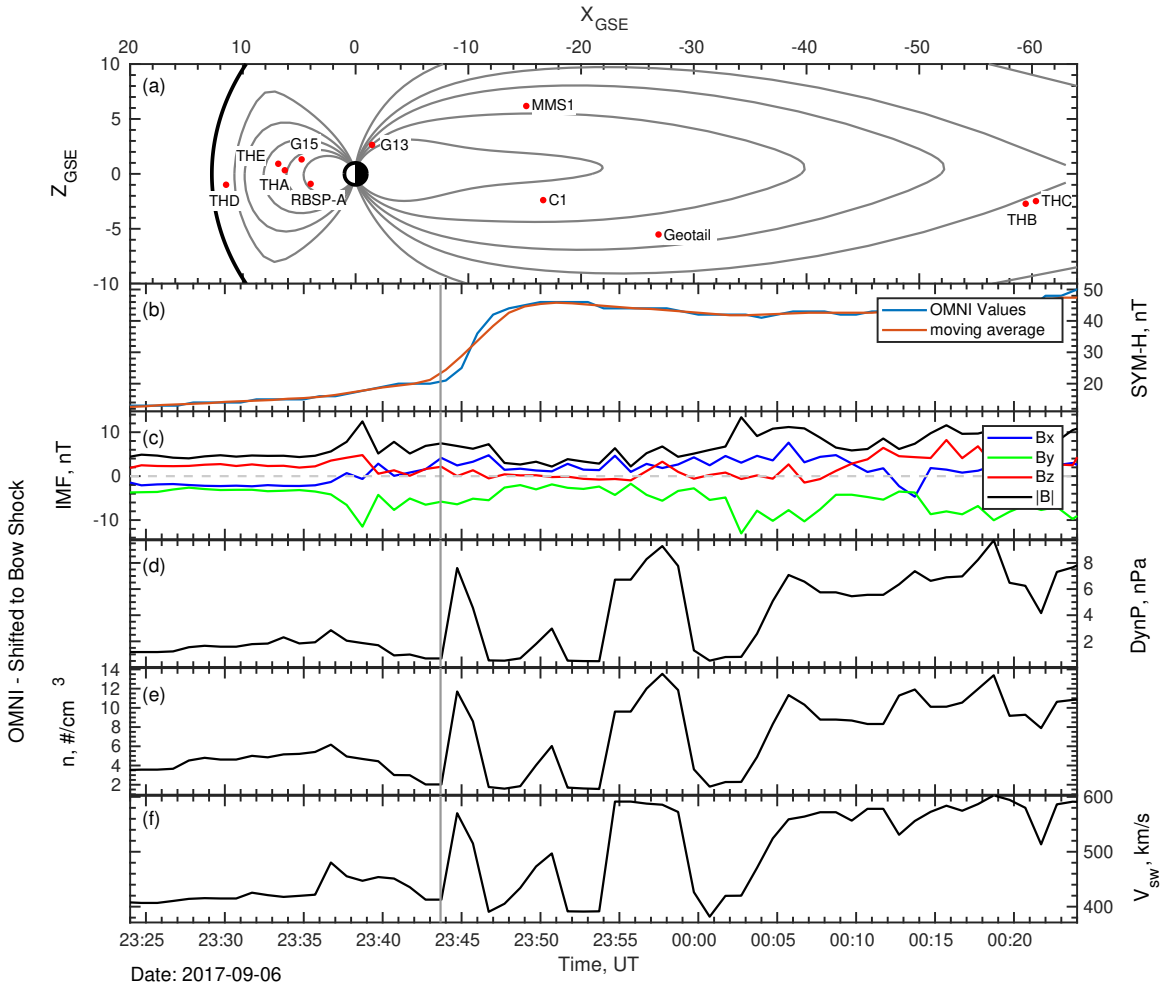

Figure 4.3: (a) XZ-Plane in GSE coordinates with the location of the spacecraft with Tsyganenko T89 as reference. The Magnetopause is drawn using the model provided by *Shue et al.* (1998). (b) SYM-H (nT) increases as result of the compression generated by the increase in the dynamic pressure. (c) IMF (nT) three components: Bx (blue), By (green), Bz (red), B total (black). (d) Solar wind dynamic pressure (nPa) shifted to the bow shock nose. (e) Solar wind number density ($\#/cm^3$). (f) Solar wind flow speed (km/s).

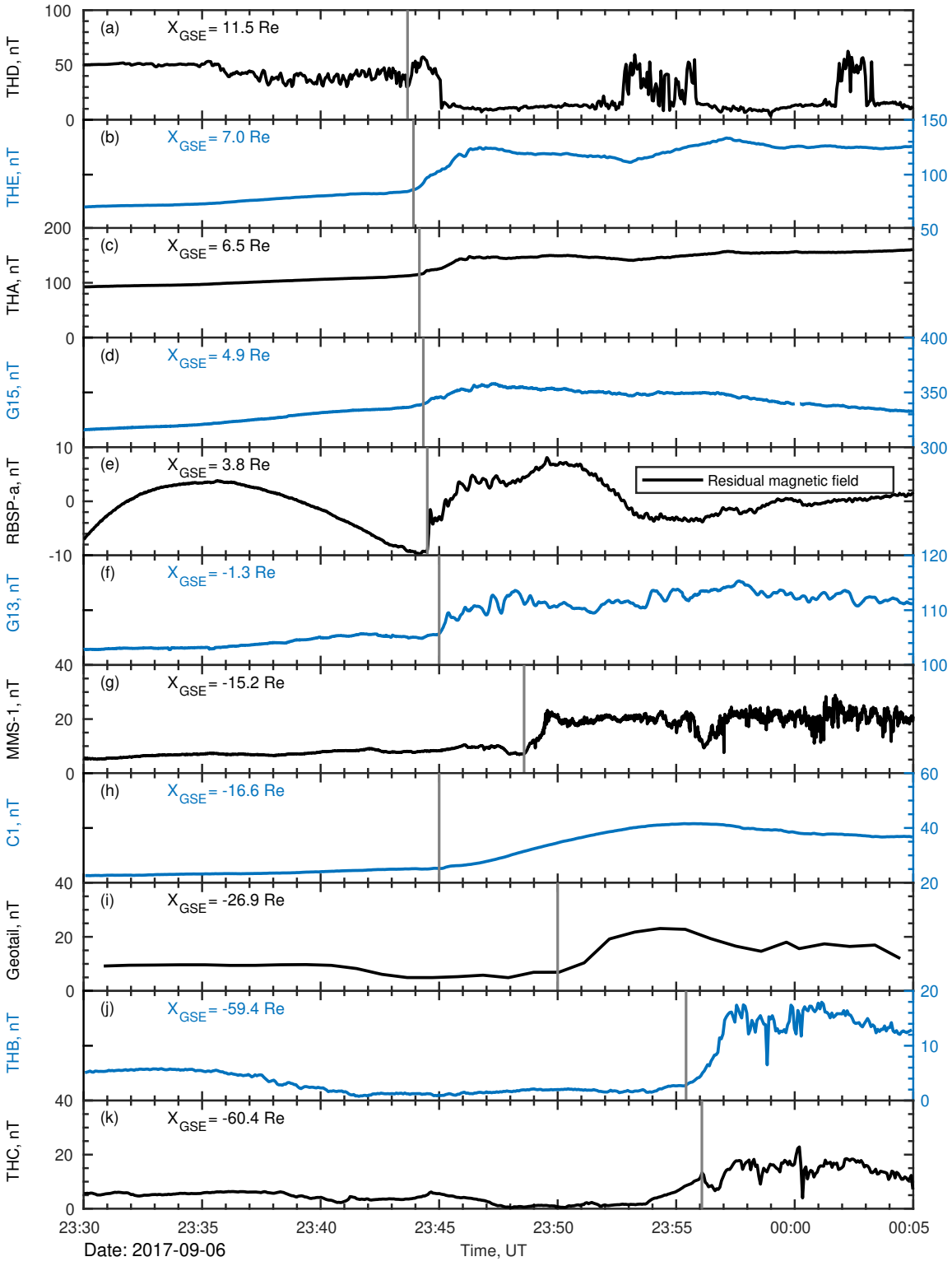

Figure 4.4: Magnetic field magnitude in nanoTesla as measured by multiple satellites. In the case of RBSP-A (plot (e)), the dipole component was subtracted using a fourth degree polynomial fitting.

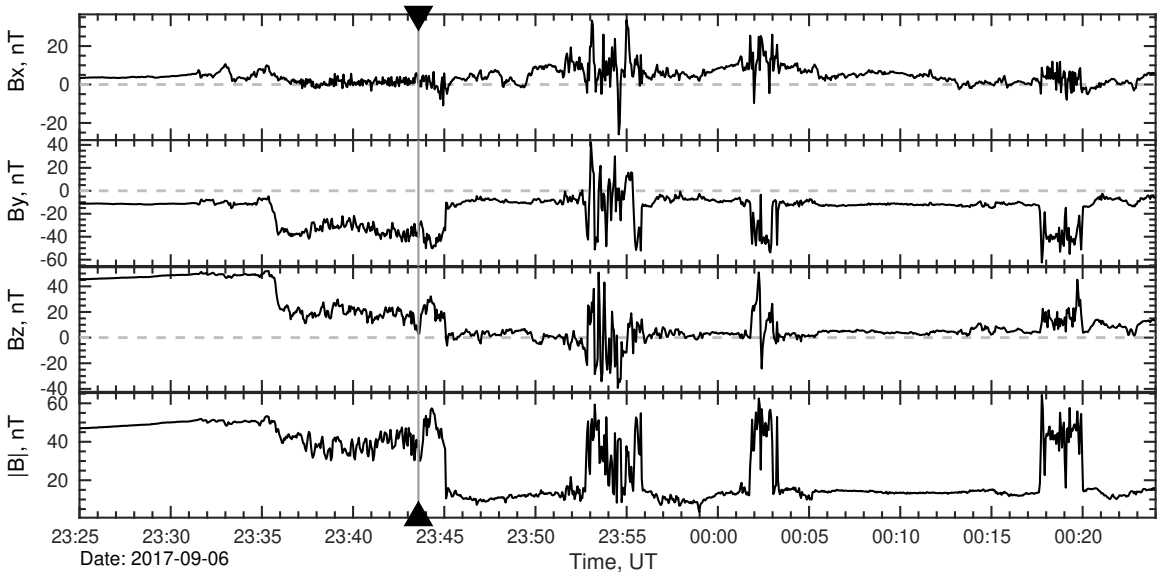

Figure 4.5: THD three magnetic field (nT) components and total magnetic field. THD is located at $(11.5, 0, -1.0)_{GSE}$, it is the first satellite inside the magnetosphere to observe the compression. The inward movement of the magnetopause places THD in the solar wind at 23:43:30 UT. The triangles indicate the first detection of the DPP and the vertical line the DPP arrival, which in this case are the same.

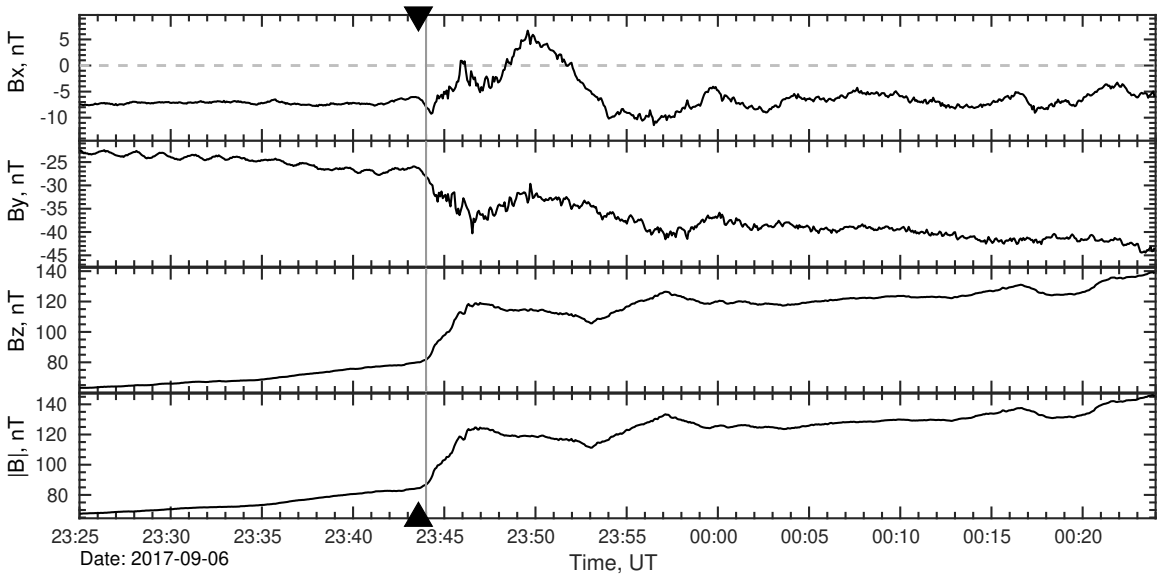

Figure 4.6: THE three magnetic field (nT) components and total magnetic field. THE is located at $(7.0, 3.4, 0.9)_{GSE}$ in the dayside magnetosphere, it observes a compression driven by the increase in the Bz. The triangles indicate the first detection of the DPP and the vertical line the DPP arrival to THE.

THEMIS-D $(11.5, 0, -1.0)_{GSE}$ is initially located on the magnetosphere side of the magnetopause and observes the compression as a couple of outbound discontinuity crossings. First, the spacecraft (Figure 4.5 crosses the magnetopause to the magnetosheath at 23:35 UT as result of a small increase in the solar wind dynamic pressure, later at 23:43:30 UT the spacecraft observes the compression of the magnetosheath and crosses the bow shock to enter the solar wind environment. Meanwhile, THEMIS-A $(6.5, 2.4, 0.3)_{GSE}$, THEMIS-E $(7.0, 3.4, 0.9)_{GSE}$ (shown in Figure 4.6), GOES-15 $(4.9, 4.3, 1.3)_{GSE}$, RBSP-A $(3.8, -1.0, -1.0)_{GSE}$ and RBSP-B $(5.6, 1.4, 0.2)_{GSE}$ are all located deeper in the magnetosphere. They observe similar compression signatures within 1 minute of each other: an increase in the total magnetic field driven by the increase of the Bz component.

Nightside: The nightside response is observed by Geotail, THEMIS-B, THEMIS-C, and the four Cluster spacecraft. The magnetic signature observed by Geotail $(-26.9, -12.8, -5.5)_{GSE}$ shows (see Figure 4.7) the DPP arrival as a tilt in the Bz

component coinciding with a compression driven by By and Bz components. Further in the tail, THEMIS-B $(-59.4, -10.3, -2.7)_{GSE}$ shown in Figure 4.8 observes a signature proposed by *Moldwin et al.* (2001) as a Bz South-then-North turning previous to crossing the current sheet. THEMIS-C $(-60.4, -9.0, -2.5)_{GSE}$ shows an almost identical signature to THEMIS-B. Both signatures are also similar with Geotail despite the more than 33 Earth radii of separation. The average speed of the signal is computed using RBSP-B located on the dayside as reference point for the arrival of the DPP and the compression observed later by each satellite. The speed is computed by calculating the TOF, after identifying the DPP in the solar wind (start time) when possible and the compression observed by each one of the satellites available (end time). The computed speeds are 608, 623, 600 km/s for Geotail, THEMIS-B, and THEMIS-C respectively. These values are consistent with the solar wind speed observed by ACE (600 km/s) and WIND (580 km/s) during the DPP. Meanwhile, the Cluster spacecraft (Figure 4.9) located at $(-16.6, 0.5, -2.5)_{GSE}$ observe a compression that is likely related to a previous process in the tail. This signature is probably result of a previous dynamic pressure increase such as the observed in Figure 4.3 at 23:37 UT, or to another process in the dynamics of the magnetosphere. The TOF computed speed for the signature is 1991 km/s, while the TOF computed by cross correlation of the magnetic field magnitude measured by Cluster 2 and 3, show a tailward movement of 675 km/s in the X_{GSE}.

Dusk: While there are no satellites located in the inner magnetosphere dawn sector, there are five located in the dusk sector during this event. MMS spacecraft $(-15.2, 16.6, 6.2)_{GSE}$ magnetic field data are shown in Figure 4.10. The constellation travel in close formation and are considered a single observation. GOES-13 $(-1.3, 5.9, 2.6)_{GSE}$ shown in Figure 4.11 is located at the edge of dusk and night sectors of the inner magnetosphere, observed the compression driven by an increase in the Bz component, and also ULF wave activity in all components. The MMS

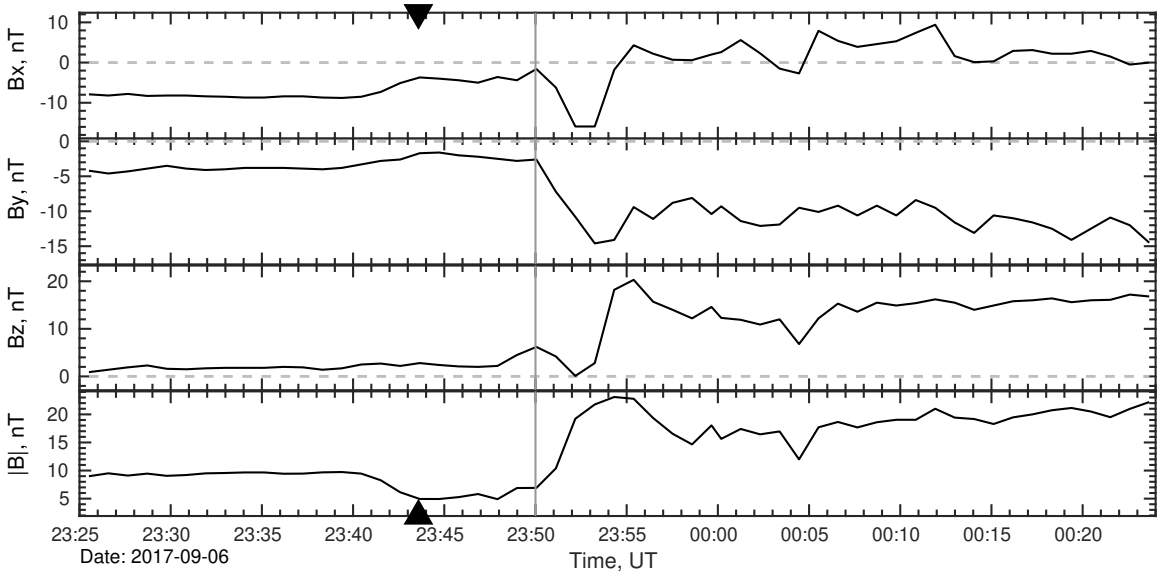

Figure 4.7: Geotail three magnetic field (nT) components and total magnetic field. Geotail is located at $(-26.9, -12.8, -5.5)_{GSE}$ near the neutral sheet, it observes a compression around 23:50 UT. The triangles indicate the first detection of the DPP and the vertical line the DPP arrival to Geotail. Data has 1 minute resolution.

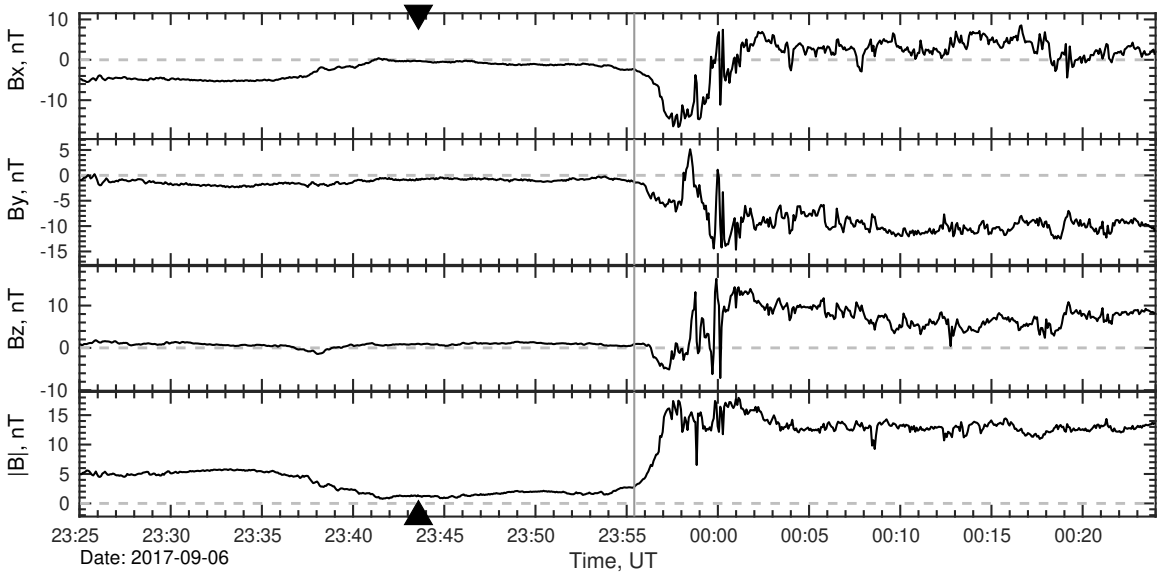

Figure 4.8: THB three magnetic field (nT) components and total magnetic field. THB is located at $(-59.4, -10.3, -2.7)_{GSE}$ very close to the neutral sheet. The triangles indicate the first detection of the DPP and the vertical line the DPP arrival to THB.

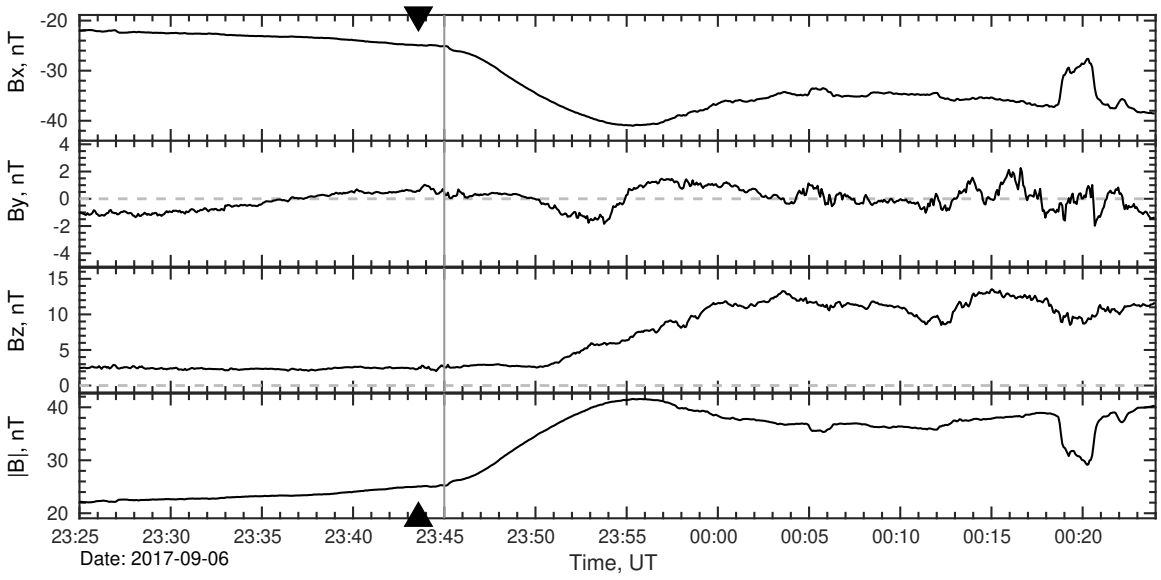

Figure 4.9: Cluster-1 three magnetic field (nT) components and total magnetic field. Cluster-1 is located at $(-16.6, 0.5, -2.5)_{GSE}$ in the southern tail lobe, at these locations the compressions are commonly driven Bx. The triangles indicate the first detection of the DPP and the vertical line the DPP arrival to Cluster-1.

spacecraft located in the solar wind at dusk observed the DPP as outbound movement of the magnetopause and crossing to the magnetosheath. This is similar to the magnetopause motion proposed by *Sibeck* (1990) resulting from the magnetopause compression and generates a steep fast-mode wave in the magnetosphere that causes the magnetopause to flare outward.

Ground-Based Magnetometers: We observed the magnetic field variations between the periods before and after the DPP arrival. The top panel of Figure 4.12 shows Ministik Lake magnetometer station as example. In average, the magnetic field magnitude increase 33 nT after the DPP arrival, which is also observed by the SYM-H index increase. We also performed a magnetic field variability analysis to examine the effect of the DPP as observed on the ground. We adjusted third degree polynomials for the periods of time before and after the DPP arrival (see Figure 4.12). We computed the RMSD to obtain a measurement of the variability of the signal.

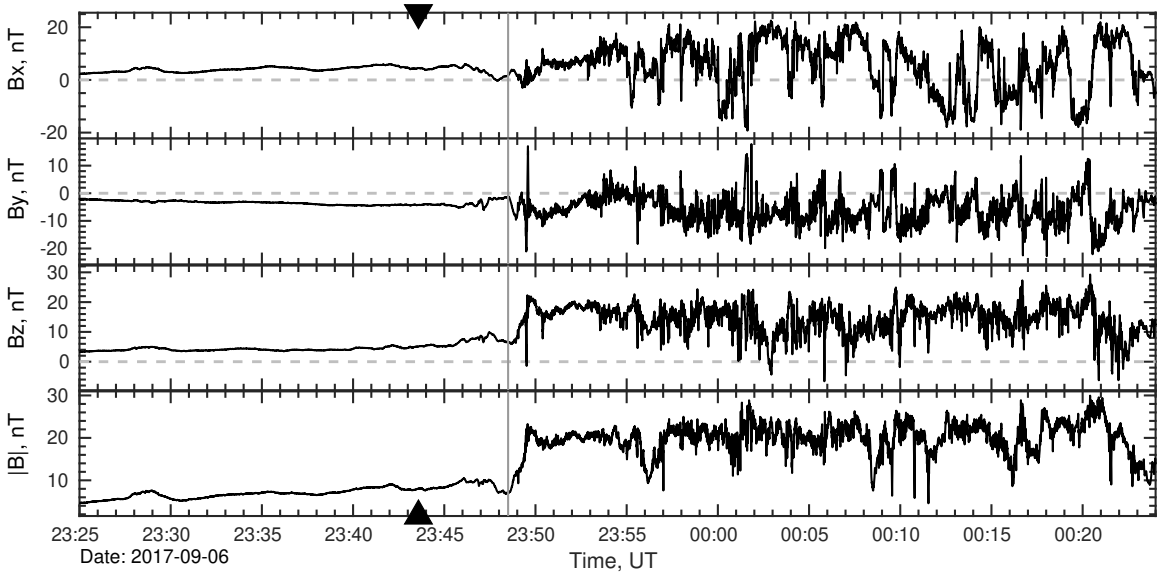

Figure 4.10: MMS-1 three magnetic field (nT) components and total magnetic field. MMS-1 is located at $(-15.2, 16.6, 6.2)_{GSE}$ near the plasmasheet in the dusk flank of the magnetotail. An increase in the magnetic field magnitude is observed at 23:48:30 UT. The triangles indicate the first detection of the DPP and the vertical line the DPP arrival to MMS-1.

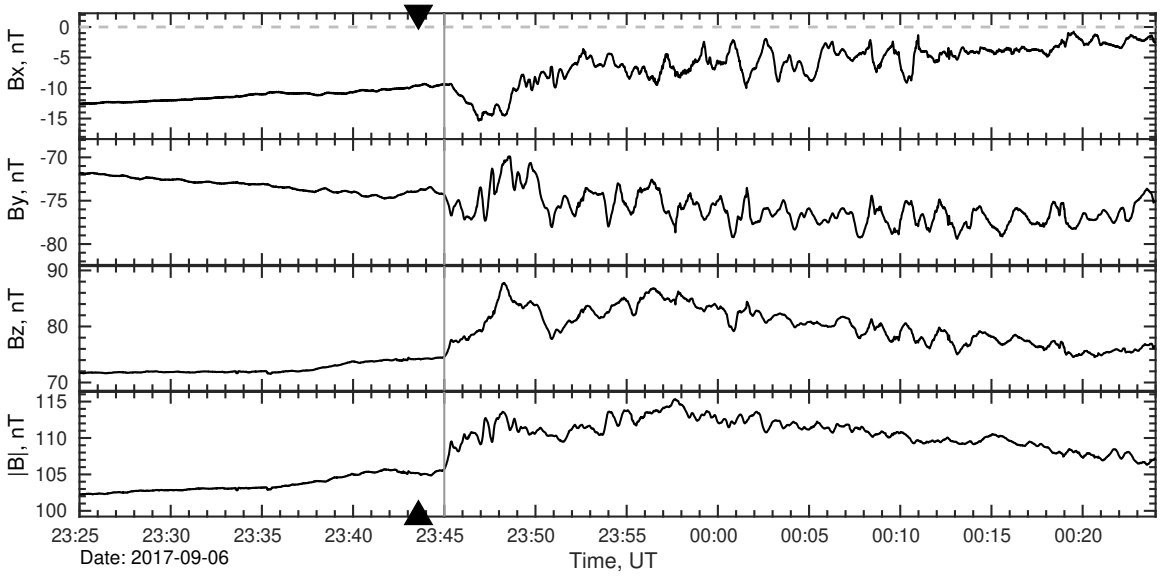

Figure 4.11: G13 three magnetic field (nT) components and total magnetic field. GOES-13 is located at $(-1.3, 5.9, 2.6)_{GSE}$. The triangles indicate the first detection of the DPP and the vertical line the DPP arrival to GOES-13.

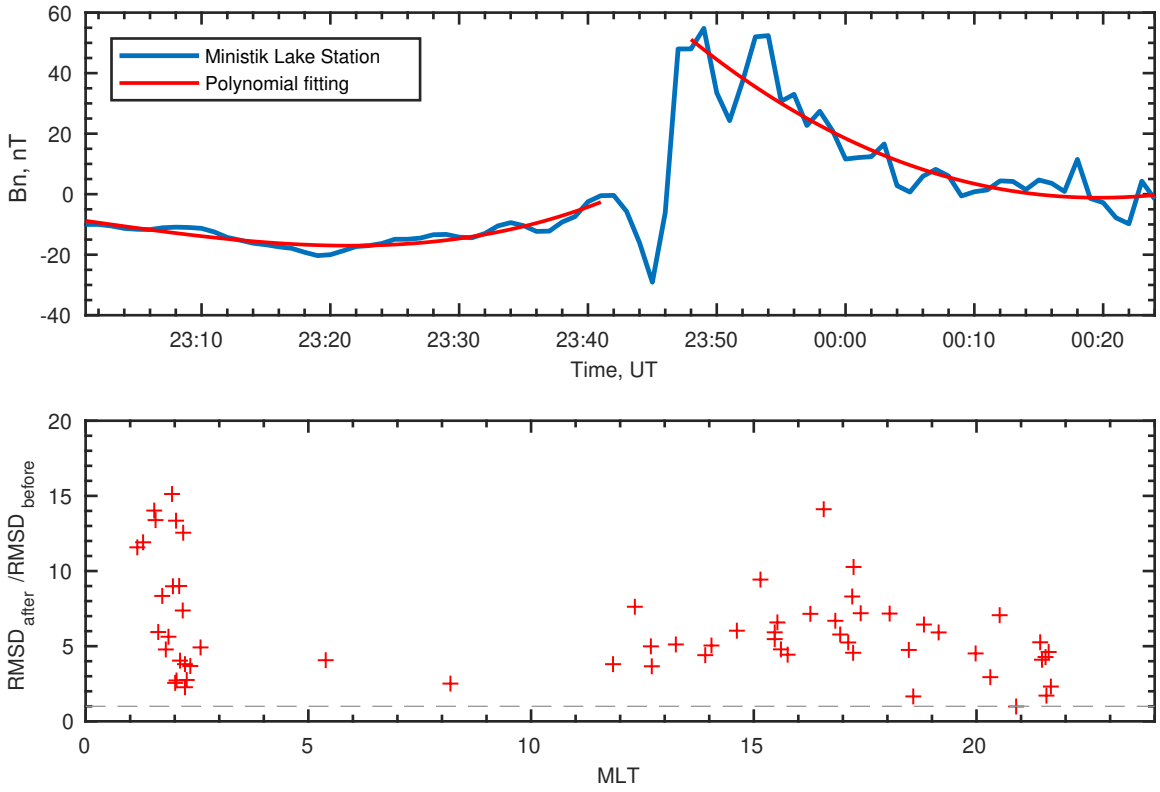

Figure 4.12: (Top) As example, Ministik Lake station magnetogram after removing daily baseline in blue. Polynomial fitting by least squares for times before and after the DPP disturbance arrival. (Bottom) Ratio of the root-mean-square-deviation after and before the DPP disturbance arrival as function of magnetic local time for all stations.

For this event, 61 of 62 stations observed an increase of the magnetic field variability after the DPP arrival. The mean RMSD before the DPP arrival was 9.72 nT, the mean RMSD after the DPP arrival was 48.7 nT.

4.6 Results

The events detected in this chapter show systematic behavior of the magnetosphere perturbation due to the antisunward movement of the DPPs outside the magnetosphere. We are able to follow the tailward propagation using different satellites at multiple locations of the magnetosphere. In 27 of the events, there are observations

available near or inside geostationary orbit, in 25 of the events there is at least one satellite observing signatures corresponding to the onset of the ULF waves, probably related to the magnetospheric oscillation modes triggered by the DPP. However, in most of the cases the signatures detected are a direct result of the DPP compression through the boundaries of the magnetosphere, which impact the magnetosphere in different ways depending on the region and local time sector.

We are able to identify these signatures using different spacecraft that observe a magnetic compression. In Figure 4.13 the TOF $V_{x_{GSE}}$ speed of tracked signatures is shown with respect to the X_{GSE} coordinate. The arrival time is obtained by visual inspection and the error bars correspond to uncertainties due to the data time resolution and noise that can compromise the correct identification of the exact arrival time. Figure 4.13 shows that the speed computed in 209 of 229 observations was between the standard deviation of the distribution of TOF and the respective solar wind speed of each event. The reason why higher than solar wind speeds are observed in the dayside is probably due to the compressional fast-mode wave generated by the DPP as described by *Tamao* (1964), which could be easily mistaken with the compression generated by the propagating DPP moving tailward. We suggest that the dispersion of the perturbation speeds (specially those outside the standard deviation) is mainly due to the inclination of the DPP front, as we observed in six events where multi-spacecraft timing was available in the solar wind. When the inclination in one dimension of the DPP front is considerably larger in relation to the separation of the satellites in the same dimension, the separation becomes important and explains the discrepancies between the perturbation speed expected and computed by TOF. For example, if two satellites have a separation of 10 Re only in the Y_{GSE} component, a DPP front traveling at 400 km/s and an inclination of 45° with respect to dawn and dusk, the two satellites will observe a delay between them of 160 seconds equivalent to 10 Re. The computed speeds of the DPP are outside realistic propagation wave

speeds in several of the observations: in 3.5% of observations the computed speed is higher than the Alfvénic speed at any region of the magnetosphere, and in a 7% of the observations there were negatives values (i.e. implying moving sunward) were found.

A survey of the type of response observed was made for all in space observations collected during the 37 events. The response analysis at geostationary orbit was made using GOES-13 and GOES-15. The results show, the magnetic compression is mainly driven by the Bz component of the local magnetic field, and the compression is observed in all local time sectors. We used Fast Fourier Transform (FFT) analysis to study the Pc4-5 waves power. We separated the observations into before and after the compression, in order to avoid the power generated by the step-like function due to the compression. The results show an increase in power in at least one of the magnetic field components in 86% of the observations and in 73% of the events. The increase in Pc4-5 wave power in at least one of the magnetic field components was observed in all the dayside (09-15 LT) observations, 81% in the dawn (03-09 LT) sector, 80% in the dusk (15-21 LT) sector, and 86% in the night (21-03) sector. From the point of view of the ground-based magnetometers. Due to their low time resolution (1-minute), it is not possible to track the signal between different stations, or perform an FFT analysis for the Pc4-Pc5 range, but it is possible to observe the compression generated by the DPP, and the increase in the variability generated by the DPP. Counting all the ground-based magnetometer stations available during the 37 events, the magnetometers performed 2486 time series of observations. In 2071 time series there was an increase in the magnetic field after the arrival of the DPP, equivalent to the 83% of all observations. A total of 2194, equivalent to a 88% showed an increase in the magnetic field RMSD. On average, the RMSD increase significantly (5.8 times) after the DPP arrival.

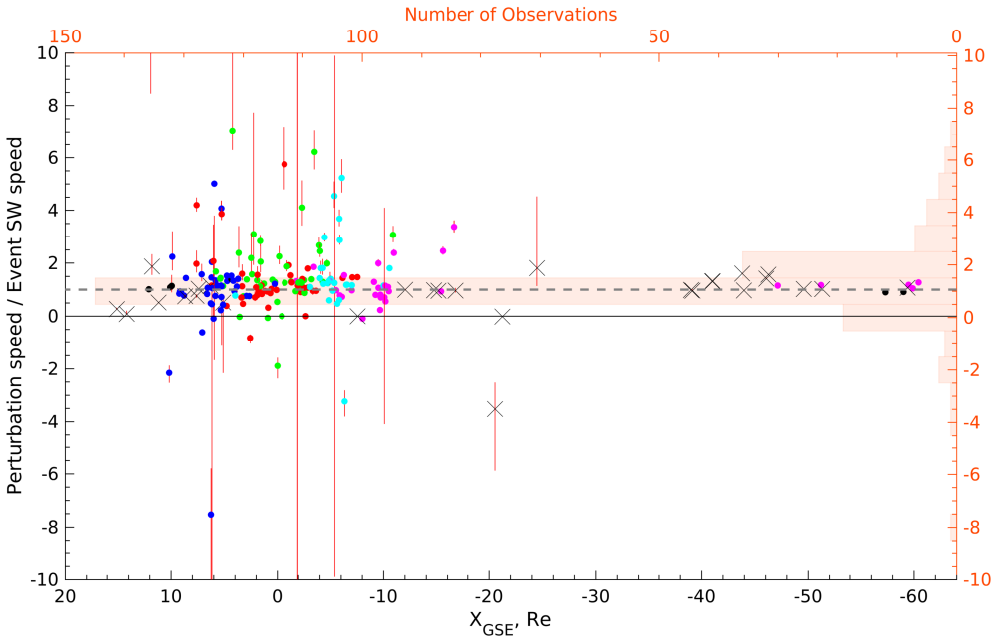

Figure 4.13: Transient speed measured by Time-Of-Flight between several spacecraft for each event as function of the solar wind speed during that event. Error bars are defined as the error generated during the identification of the time of a magnetic perturbation that can be associated to the DPP propagation. The color of the dots represent the region where the satellite was located. (Black crosses) Solar wind; (Blue) days sector magnetosphere; (Green) dawn sector magnetosphere; (Red) dusk sector magnetosphere; (Cyan) night sector magnetosphere; (Magenta) tail lobes; (Black dots) magnetosheath (around any region).

4.7 Discussion

We use the HSO to perform a global view of the magnetospheric response to sudden increases in the solar wind dynamic pressure during northward IMF. The conditions set for event detection, favored the detection of events with of large DPP during quiet conditions. The current capabilities of the HSO make possible simultaneous observation and tracking of DPPs from the solar wind through most of the magnetospheric cavity. The tracking of perturbation can offer a more complete explanation to many single event studies or statistical studies from single satellite missions made in the past especially enabling the observation of propagating signatures.

The results show the importance of observing the magnetosphere from multiple satellites throughout the magnetosphere. The analyzed events show different types of magnetic signals, such as dayside compressions, ULF waves at dawn, dusk and night sectors, and in the magnetotail. There was also observations of South-then-North compression signatures in the magnetotail. This work examined the DPP signatures traveling with the solar wind while compressing the magnetosphere from upstream to the magnetotail. While the initial impact of the DPP into the magnetosphere triggers fast-mode waves that propagate faster than the solar wind, the main transients observed travel at solar wind speed around the magnetopause and generate new ULF signatures.

We found that the tracking becomes very complicated to perform when the satellites are located in the outer magnetosphere. MHD waves resulting from the compression move faster and along different paths. However, in the case of the tail the situation is more clear. The magnetic lobe field pressure increases as it balances with the static and dynamic pressure as stated by *Fairfield and Jones* (1996) and *Collier et al.* (1998). Our results are in agreement with *Huttunen et al.* (2005) that SIs in the tail move at solar wind speed. *Moldwin et al.* (2001) showed that a short period (1-10 min) DPP traveling tailward through the magnetosphere can be seen

as South-then-North Bz signatures. However, the DPPs involved in our study have longer duration (above 20 minutes) and therefore we observed only the first half of the south-then-north Bz signature.

We found that the magnetic response at geosynchronous orbit is a sudden increase in the magnetic field magnitude. This is in agreement with observations reported by *Borodkova et al.* (2005), *Borodkova et al.* (2008), and *Zuo et al.* (2015). It is also found that the perturbation is moving at solar wind speed, which is in agreement with the SIs speed reported by *Huttunen et al.* (2005) using Cluster observations in the tail. Our study using the HSO is able to clearly observe the propagation of the DPP signatures throughout the magnetosphere essentially knitting together the earlier studies that were limited to specific regions of the magnetosphere.

In relation to the unrealistic inferred velocities (such as negatives propagation speed), *Oliveira et al.* (2018) and *Oliveira and Raeder* (2015), found fast moving shocks tend to have smaller inclination angle than slower shocks. When comparing the computed DPP speeds with the solar wind speed of each event, it was found that the outlier values correspond mainly to slow solar wind, which would suggest that those values were from DPP fronts with high inclination with respect to the X_{GSE} coordinate.

4.8 Conclusion

Large DPP give rise to systematic signatures through all regions and sectors of the magnetosphere. In addition to the waves propagating inside the magnetospheric cavity, the increase in the dynamic pressure in the solar wind creates a disturbance that propagates tailward through the magnetosphere at speeds close to the solar wind speed, the disturbance can be tracked using the satellites that form the HSO. The assumption of a planar solar wind disturbance explains the majority of the events studied here. However, the differences in plasma density in different regions, and the

angle of the disturbance front generates discrepancies in the calculated propagation velocities. The analysis of the disturbance angle explained the differences in six of the events where multi-spacecraft timing was possible to perform due to the Cluster mission location in the solar wind.

Many of the events identified in this chapter lend themselves to deeper analysis due to having multiple observations in specific regions (opposed to distributed in multiple regions as focused upon here) enabling studies examining smaller scales. In the next chapters are included in the analysis recently available 1 second resolution ground-based magnetometer data from SuperMag, and Intermagnet. We selected some of the events studied here to observe the DPPs' propagation effects in the inner magnetosphere. We will focus in the propagation of the preliminary impulse from geostationary orbit altitude to the Earth's surface, including its speed and polarity dependence with latitude and local time, to evaluate the different theories about its propagation, which we expect will contribute to improved understanding of the global dynamics of the magnetosphere.

CHAPTER V

Shock Inclination Effects in Preliminary Impulse Propagation

5.1 Introduction

In the previous chapter we perform a tracking of the effect of solar wind dynamic pressure through the magnetosphere using distributed spacecraft from the dayside to the magnetotail. In this chapter, we focus on events with DPP resulting from interplanetary shocks. In addition to the HSO spacecraft, observations from ground-based magnetometers are used to study the preliminary impulse in the dayside magnetosphere.

Fast interplanetary shocks give rise to SSCs or SIs in the geomagnetic field, and are ideal to study wave propagation through the magnetosphere. SSCs/SIs are sudden changes in the magnetic field resulting from dynamic pressure disturbances traveling with the solar wind. Since the balance between the solar wind dynamic pressure and the magnetosphere dynamic pressure determines the shape of the magnetosphere, SSCs/SIs often generate large compressional waves that can be used for probing the

Parts of this chapter were submitted in: Vidal-Luengo, S. E., & Moldwin, M. B. (Under Review). Shock Inclination Effects in Preliminary Impulse Propagation Observed by Ground-Based Magnetometers and the Heliophysics System Observatory. Journal of Geophysical Research: Space Physics

structure of the magnetosphere (*Chi et al.*, 2001; *Chi and Russell*, 2005; *Maeda et al.*, 2009; *Menk and Waters*, 2013).

Sudden changes in the solar wind dynamic pressure induce perturbations that propagate throughout the entire magnetosphere (*Collier et al.*, 1998; *Slavin et al.*, 2005; *Vidal-Luengo and Moldwin*, 2021). The perturbations in the solar wind are likely to trigger ULF waves observed in the magnetosphere (*Archer et al.*, 2019). The higher frequency component of these waves become filtered while traveling to inner regions of the magnetosphere as compressional mode energy is converted to transverse wave energy, but the low frequency component propagates throughout the entire magnetosphere (*Archer et al.*, 2013). *Tamao* (1964) formulated a three-dimensional model of hydromagnetic waves in a cold plasma. Despite not considering important factors that affect the propagation of waves in the magnetosphere, such as density variations; magnetospheric and ionospheric currents; magnetospheric modes of oscillation; particle-wave interactions; and many other processes (most discovered decades later), the hydromagnetic model provides the fundamentals for magnetoseismology. *Tamao* (1964) proposed that perturbations propagate isotropically through the fast mode and also along the magnetic field lines through the Alfvén mode. Figure 5.1 shows the path of both perturbations and the source of the maximum amplitude observed on the ground. Considering a cold plasma, the fast mode wave has the same speed as the Alfvén mode wave. Since fast mode waves travel in all directions, for each L-shell the ground station on that L-shell observes a train of disturbances. The magnetic disturbances traveled along the field line through the Alvén mode wave, whose maximum observed deviation in the H-component corresponds to the region where the fast mode perpendicularly compressed the magnetic field. The travel time it takes the perturbation from the source to reach the ground-based station by traveling first in straight line with the fast mode speed (v_f) and then mode coupling to Alfvén waves (v_A) and following a determined field line path is known as "Tamao Travel time"

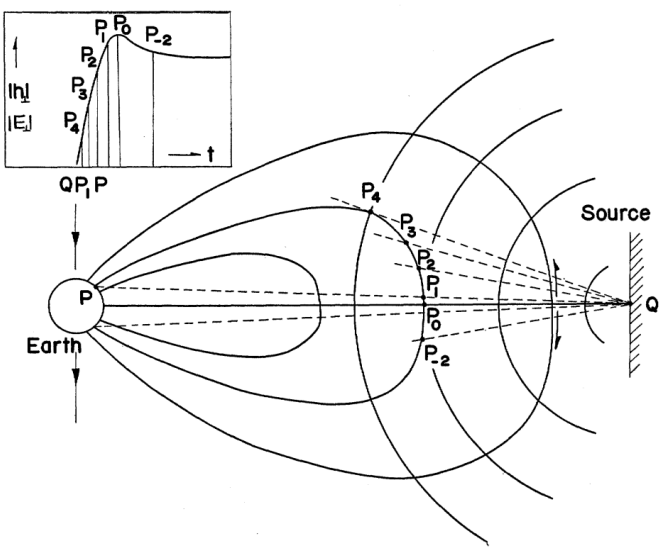

Figure 5.1: Schematic illustration of the propagation of Alfvén and fast mode based in Tamao's hydromagnetic wave theory. The original disturbance propagates as a fast mode wave, but dissipates energy by coupling into Alfvén waves that travel parallel to the magnetic field. Alfvén waves do not dissipate while traveling along the magnetic field, which explains why the preliminary impulse has a larger amplitude at higher latitudes (*Tamao*, 1964).

which can be written as:

$$t_{Tamao} = \int_{l_1} \frac{ds}{v_f(\mathbf{r})} + \int_{l_1} \frac{ds}{v_A(\mathbf{r})} \tag{5.1}$$

in which l_1 and l_2 correspond to the path of the fast mode and Alfvén mode, respectively.

The response observed by ground observatories has been described by *Araki* (1977, 1994) and *Kubota et al.* (2015). They decomposed the main disturbance field (D_{sc}) into three parts ($D_{sc} = DL + DP_{pi} + DP_{mi}$). The DL represents the step-like function of the increase of the H-component, the DP_{pi} corresponds to the preliminary impulse (positive in the morning and negative in the afternoon), and the main impulse DP_{mi}. When examining different magnetograms, they noticed that the first observed deflection appeared to show that the perturbation arrived at the same time for all latitudes

for a given local time. *Kikuchi and Araki* (1979a,b) and *Araki* (1994) proposed the Earth-ionosphere waveguide model, where the polar electric field is transmitted almost instantaneously to low latitudes via an electromagnetic signal. For a wave moving at the speed of light from high-latitudes to the equatorial region, the preliminary impulse should arrive essentially simultaneously at all latitudes for a given local time. In contrast, *Chi et al.* (2001) suggested that such a process is not needed to explain the timing of the preliminary impulse, and that a small delay between stations at low and high latitudes should be noticeable when using synchronized 1 second ground-based magnetometer data, and that the delay in the maximum deflection is the result of the Alfvén waves taking different paths, and the conversion of fast mode waves into Alfvén mode waves while traveling through L-shells (*Tamao*, 1964). The shock inclination with respect to the dayside magnetosphere has effects on the arrival time of the magnetic perturbation. The magnetospheric effects of the shock inclination in the XY plane have been addressed in the past (*Takeuchi et al.*, 2002; *Oliveira and Raeder*, 2015; *Shi et al.*, 2019). *Xu et al.* (2020) used polar ground-based stations showed that the first response in $\partial B/\partial t$ is observed first and in larger magnitude in the local time hemisphere where the shock hit first.

Takeuchi et al. (2002) observed one event that occurred during northward IMF that had an extremely long rise time ($\sim$30 min), showing that the inclination in the XY plane is important to predict the speed of the magnetospheric response. For this purpose, the accuracy in the calculation of the shock parameters is essential for analysis of the interaction of shocks with different inclinations with the magnetosphere. Currently, the most popular methods are the modified RH08, RH09, and RH10 equations. These methods have shown to be more effective than other more simple methods that have important limitations such as magnetic coplanarity, velocity coplanarity, and the mixed data methods of Abraham-Shrauner (*Abraham-Shrauner and Yun*, 1976; *Koval and Szabo*, 2008).

In this chapter we explore the impact of interplanetary shock angle on the propagation of the fast and Alfvén waves that give rise to the preliminary impulse, by timing their arrival to ground-based magnetometer stations at different magnetic latitudes and local time. For this purpose we use a subset of the database of SIs during northward IMF conditions developed by *Vidal-Luengo and Moldwin* (2021) that were driven by fast interplanetary shocks. The shocks were identified from the CfA shock catalogue (https://www.cfa.harvard.edu/shocks/). The catalogue was compared with observations made by the HSO from inside the magnetosphere, to obtain information about the disturbance speed and inclination using multi-spacecraft timing. The observations were also compared with 1 second resolution ground-based magnetometers observations.

5.2 Data

5.2.1 Spacecraft Overview

The GOES provide magnetic field observations in the magnetosphere at 6.6 Re (*Singer et al.*, 1996). Van Allen Mission probes consist of two spacecraft for the study of the Van Allen radiation belts. They have elliptic orbits with apogee around 6 Re and perigee 0.1 Re (*Spence et al.*, 2013). The Cluster mission consists of four spacecraft traveling in tetrahedral formation. Due to the proximity to each other, sometimes their observations are considered as a single point measurement. However, sometimes two of the spacecraft are far enough apart to distinguish arrival times from traveling perturbations. Cluster spacecraft have highly elliptical and nearly polar orbits with an apogee around 20 Re. The THEMIS mission consists of five identical spacecraft. In 2011, two of the five spacecraft were put in orbit around the Moon, while the other three stayed orbiting Earth in an highly elliptical close formation (*Angelopoulos*, 2009, 2010). The MMS mission consists of four spacecraft

orbiting Earth in a very close formation. Due to the extreme proximity between the spacecraft, we consider the constellation as a single observation. The ACE and WIND are located in the Sun-Earth L_1 Lagrange point, at around 200 Re from Earth. ACE and WIND are the main contributors to the OMNI data, and also the spacecraft used by the CfA to build the shock database. The data used and generated for this chapter was deposited in the University of Michigan Deep Blue database (https://doi.org/10.7302/9zwy-zs82).

5.2.2 Ground Magnetometers Overview

The ground-based magnetometers consist of multiple arrays collected, processed, and standardized by SuperMag (*Gjerloev*, 2012), and Intermagnet (*Kerridge*, 2001). The data have a time resolution of 1 second, and Intermagnet data were rotated to the local North-East-Zenith magnetic coordinates when necessary to match with the coordinates used by SuperMag. All the ground-based stations are located between 0 and 90° of AACGM latitude and in the dayside sector (6 - 18 LT). In consequence that only in North America there are enough stations with 1 second time resolution data available to cover north and south of the ground footprint of the plasmasphere, all the events studied correspond to events when the North American sector was in the dayside. The data for low latitudes and the southern hemisphere are limited and cannot be included in the analysis.

5.2.3 Shocks Database

The CfA catalogue provides shock parameters computed by eight different methods. Currently, the most popular methods are based in the solution of MHD RH08, RH09, RH10 equations that minimizes the χ^2 merit function (*Viñas and Scudder*, 1986; *Szabo*, 1994; *Koval and Szabo*, 2008; *Wilson III et al.*, 2017). While these methods have been constantly improving during the last decades, they still face chal-

lenges to accurately compute the shock inclination angles in some circumstances. The accuracy of the shock speed and the distribution of density points on both sides of the shock can generate important differences in the calculation of the shock parameters. In some of the events analyzed in this chapter we observed important differences in the shock parameters even when they are computed with similar methodologies such as RH08, RH09, and RH10.

5.3 Methodology

We previously developed an algorithm to automatically detect potential DPPs events (*Vidal-Luengo and Moldwin*, 2021). We added two new conditions to the original three conditions used to identify the events for this chapter. The conditions are: (1) the increase of the SYM-H index must be larger than 6 nT; (2) the rise time must be in less than 3 minutes; (3) the SYM-H increase must occur during northward IMF that lasts for at least 3 minutes; (4) Shock information available in the Interplanetary Shock Database of the CfA, and (5) the preliminary impulse must be recognizable from the ground-based station data in at least 3 stations between a 2 hour local time window (the dayside is sub-divided into 6 LT bins two hours wide). Since the SuperMag 1 second time resolution data are available between 2012-2017, we search for events during this interval of time. Using these conditions we found 12 events for analysis, from the 84 DPPs events found using the SYM-H index between 2012 and 2017. The list of events with the interplanetary shock inclination angles in GSE, and $\frac{\Delta P}{P}$ are shown in Table 4.1. The HSO provides observations from different regions depending on the location of each spacecraft during each event studied. In the situation where more than four spacecraft are located in the solar wind, or dayside magnetosphere, we verify the spacecraft are not too far apart from each other, or are coplanar. Assuming a planar front, we perform multi-spacecraft timing to determine the front of the perturbation generated by the shock impact and

compare the results with the shock information from CfA database, and with the ground-based observations.

The data from the stations are classified by AACGM coordinates (*Baker and Wing*, 1989) and local time. We extract the north component, and filter with a 30 second low-pass Gaussian filter in order to remove small variations from the data. We removed the time distortion resulting from the application of the filter and compared it with the unfiltered signal to verify the filter does not add other distortions. Using the filtered data, we visually identify the arrival time by identifying the preliminary impulse (positive at morning, and negative at afternoon) as the maximum deviation after the arrival of the perturbation. The ground-based stations are arranged in bins of 2 hours of local time, and between latitudes of 0-90° of AACGM Latitude.

For the latitudinal study, the arrival time of the preliminary impulse is used to calculate the latitudinal arrival delay. The latitudinal propagation is then classified into four categories of apparent propagation direction: Equator-to-North, North-to-Equator, simultaneous at all latitudes, or undetermined. The results of this classification are compared with the angle of the shock with respect to the geomagnetic dipole in GSE coordinates. In Figure 5.2 the path taken by the fast mode and Alfvén modes waves when the shock has an inclination relative to the magnetosphere. The angle of the shocks are obtained from the CfA interplanetary shock database that provides shock parameters using multiple methods *Wilson III et al.* (2017) (supplement) based on ACE, and WIND, observations. The geomagnetic dipole inclination in the XZ plane is computed using Tsyganenko T89 model (*Tsyganenko*, 1987), by computing complementary angle of the vector that describe the maximum radial distance of L-shell value L = 6.6. Hence, if the shock front is parallel to the dayside Earth's magnetic field, the angle would be 0°, and 90° in the case of a perpendicular impact.

For the study of the local time propagation of the preliminary impulse, we used

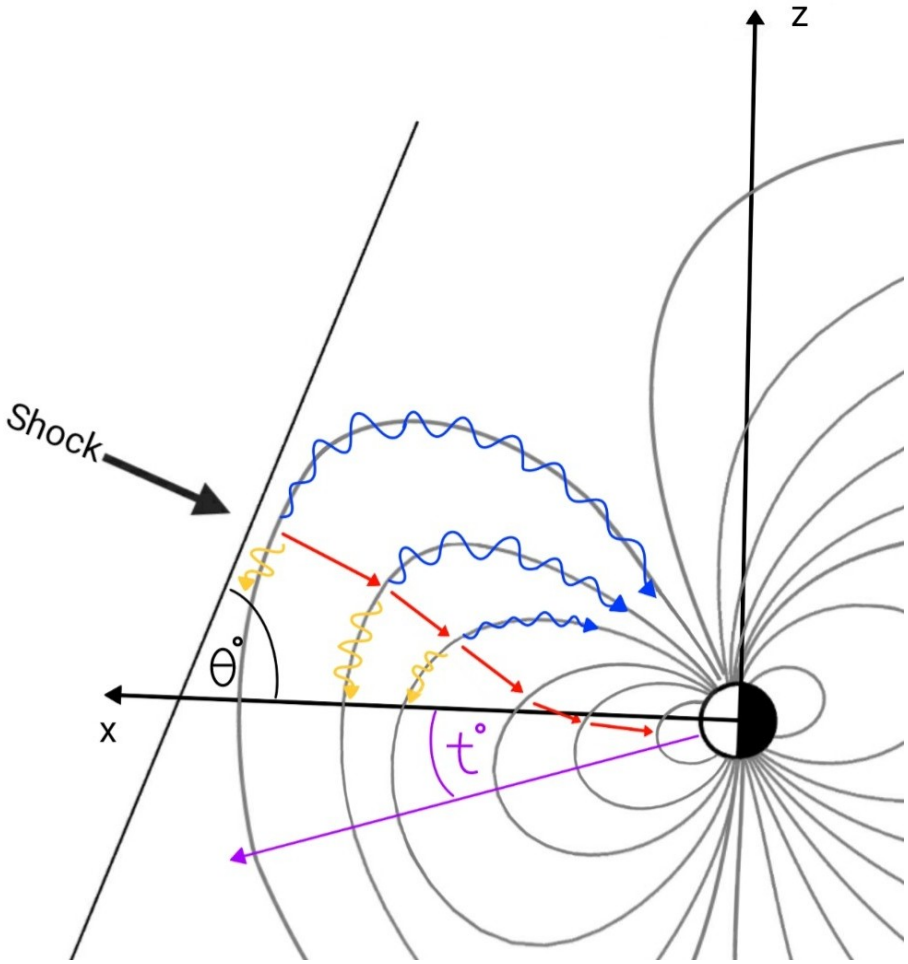

Figure 5.2: Example of the path taken by fast and Alfvén waves after an inclined shock impinges the magnetosphere north of the equator. Fast mode propagation path in red, Alfvén path to the northern hemisphere blue, and Alfvén path to the southern hemisphere in yellow. θ is the angle between the shock plane and t is the tilt angle in the XZ plane. Figure in GSE coordinates.

ID	Date	By	Bz	$\frac{\Delta P}{P}$	ϕ	θ	Dipole	λ	NE/EN	Method
1	2012/01/24 15:03	-22.0	15.8	7.6	272.8	-28.6	9.7	18.7	EN	RH10
2	2012/05/21 19:35	-0.7	1.2	3.2	167.5	-6.1	-27.8	33.8	EN	RH08
3	2012/06/16 20:19	6.6	10.5	1.8	163.5	9.3	-28.6	19.3	EN	RH08
4	2013/01/19 17:32	2.3	2.9	2.1	202.6	9.3	9.5	-18.8	NE	RH08
5	2013/07/09 20:51	5.5	8.6	3.4	111.3	-29.1	-29.8	58.9	EN	RH08
6	2013/12/13 13:23	-2.5	0.4	2.8	113.3	67.2	19.9	-87.1	Unclear	RH08
7	2014/01/09 20:10	-5.5	4.1	3.2	353.0	81.4	14.4	-95.8	Unclear	RH08
8	2014/02/07 17:05	5.9	6.9	NaN	184.5	-8.7	4.1	4.6	NE	RH08
9	2014/04/19 18:36	2.6	6.1	0.9	190.5	2.2	-18.0	15.7	EN	RH08
10	2014/06/07 16:51	5.6	10.3	4.7	88.3	22.8	-33.7	-7.3	NE	MX3
11	2015/06/21 16:44	2.1	0.8	3.6	218.6	-23.4	-39.4	62.7	EN	RH08
12	2017/09/06 23:43	-0.4	2.5	6.9	177.5	2.9	-4.2	1.3	EN	RH08

Table 5.1: Events list and shock propagation angles. The second column indicates the time where the compression was observed by the SYM-H index. By, Bz are the components of the IMF. $\frac{\Delta P}{P}$ is the solar wind dynamic compression. ϕ is the shock inclination in the XY plane. θ is the shock inclination in the XZ plane. Dipole is the Earth's dipole inclination angle in the XZ plane. λ is the magnetic latitude where the shock first impacted the magnetosphere. All values are in GSE coordinates. The last column tells if at ground the wave propagation was observed equator-to-north, north-to-equator, simultaneous, or unclear.

the positive and negative preliminary impulse to determine, when possible, which local time sector is affected first by the shock impact.

5.4 Event Analysis

There are a total of 12 events selected for analysis. The list of events with the dates, solar wind IMF, and shock parameters used are given in Table 4.1. All the SIs analyzed are the result of fast forward shocks. In this section we share two events that represent the two kinds of events found.

5.4.1 Event N°2: May 21, 2012

Figure 5.3 shows the event on May 21, 2012. The interplanetary shock detected by WIND $(293, 149, 48)_{GSE}$ at 1831 UT gave rise to a magnetospheric compression

that was later detected at 1935 UT by the stations that generate the SYM-H index. The solar wind conditions previous to the shock were very calm. The shock has an inclination (θ) in the XZ plane of -6.09°± 1.36, meanwhile the dayside magnetosphere computed with the T89 model shows tilt of -27.75°, this suggests that the shock impacts at 33.84°± 1.36 north of the magnetic equator. For this event there are two spacecraft located in the dayside magnetosphere. GOES-15 $(5.8, -2.7, -1.6)_{GSE}$ in the morning sector is the first spacecraft to detect the compression resulting from the interplanetary shock (see Figure 5.3e). GOES-13 $(4.7, 3.9, -2.6)_{GSE}$ in the afternoon sector observed the compression around 15-30 seconds later, this observation suggests that fast mode speed is 311 km/s ± 100. Assuming a cold plasma, the fast mode speed is equal to the Alfvén speed. The power model law for plasma density of *Lee and Lysak* (1989) suggests that the Alfvén speed in this region is around 440 km/s.

The response of the horizontal component observed by the ground-based stations is shown in Figure 5.3f, g and h. The preliminary reverse impulse is observed from 1100 LT. Sectors 11-13 LT and 13-15 LT show systematic observations of the arrival delay at different latitudes of the preliminary reverse impulse. The preliminary reverse impulse arrives first at mid-latitudes and later at sub-auroral latitudes of the northern hemisphere. The preliminary reverse impulse is observed in all stations in the 11-13 LT sector, which implies that the shock impacted in a local time sector between dawn and noon.

The shock observation made by WIND, and the ground-based magnetometers are in agreement for a shock/magnetopause impact north of the equator, but it is difficult to obtain directional information of the perturbation generated inside the magnetosphere using only the GOES spacecraft.

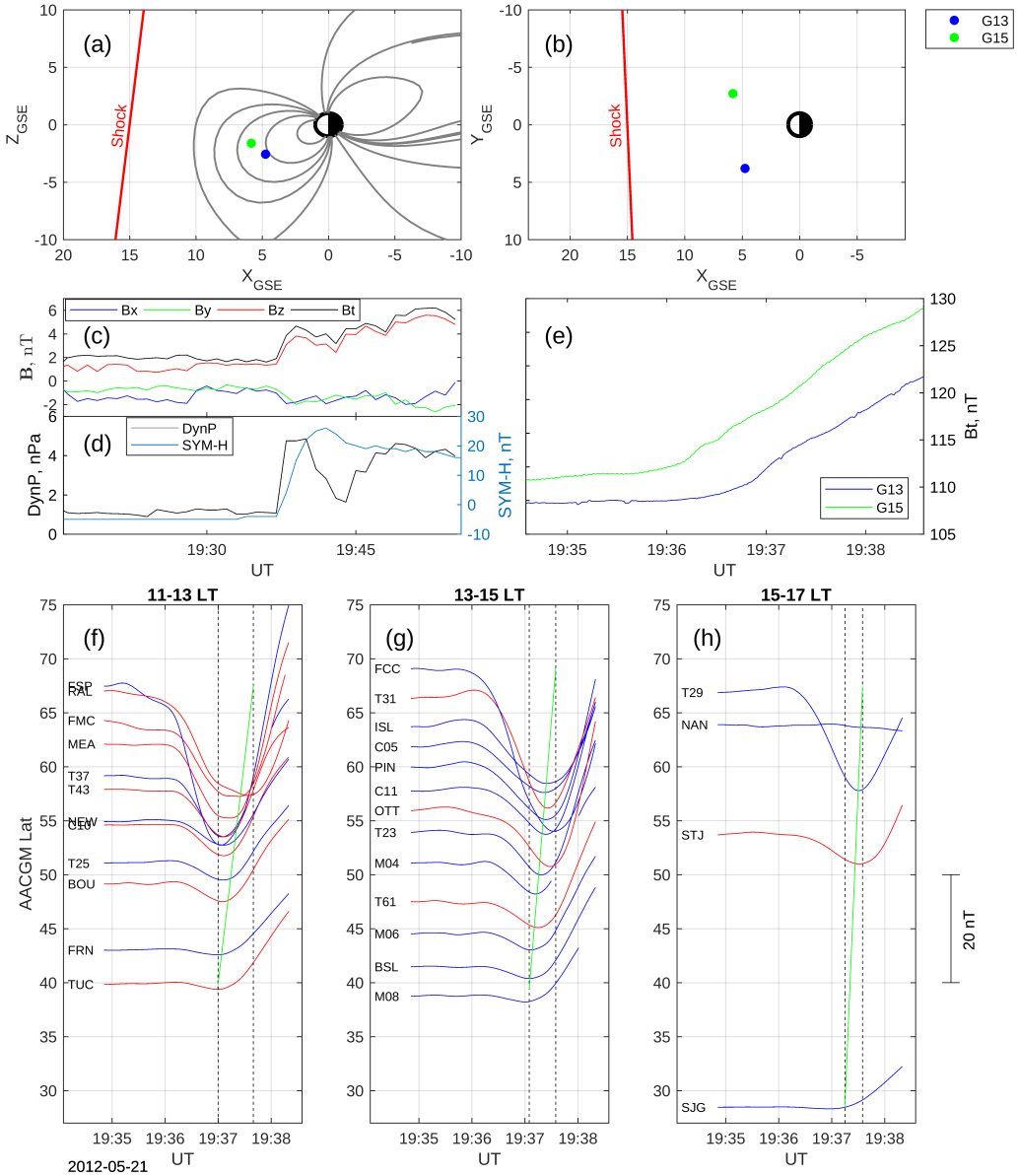

Figure 5.3: Event N°2. May 21, 2012. (a) Spacecraft location in XZ plane, reference magnetosphere computed with T89 mode. (b) XY plane. (c) IMF, (d) Left y-axis: Dynamic pressure; right y-axis: SYM-H index. (e) Total magnetic field field GOES-13 and GOES-15. (f-g-h) H-component ground-based magnetometers in the northern hemisphere and three local times. In blue the stations with a local time before the middle of the interval, in red the stations with a local time after the middle of the interval. The green line shows the delay of the preliminary reverse impulse at different latitudes.

5.4.2 Event N°10: June 7, 2014

The SI due to the interplanetary shock detected by WIND $(214, -95, 1)_{GSE}$ at 1611 UT. The disturbance was later detected at 1651 UT by the stations that generate the SYM-H index. The solar wind conditions previous to the shock were very quiet. The shock has an inclination (θ) in the XZ plane of 41.00°± 2.83, while the dayside magnetosphere computed with the T89 model has a tilt of -33.69°, suggesting that the shock impacted around 7° degrees south of the equator.

For this event there are six spacecraft located in the dayside magnetosphere (see Figure 5.4a,b). GOES-13 $(6.1, -0.5, -2.5)_{GSE}$ is located at noon. THEMIS-A $(5.4, -8.9, -1.0)_{GSE}$, RBSP-A $(4.2, -3.6, -0.5)_{GSE}$, GOES-15 $(2.9, -5.9, -0.6)_{GSE}$, THEMIS-D $(2.0, -10.8, 0.5)_{GSE}$, and RBSP-B $(0.3, -4.4, 0.4)_{GSE}$ are all located in the morning sector. They all observe the compression generated by the shock. Using THEMIS-A, RBSP-A, and GOES-13, and GOES-15, we performed multi-spacecraft timing and obtained that the front of the disturbance in the dayside has a normal vector $\hat{\mathbf{n}} = (-0.38, 0.7, 0.6)$ in agreement with a perturbation originated south of the equator. However, since all the spacecraft are near the equatorial plane, and close to be in the same plane, this value has been observed carefully.

The response of the horizontal component observed by the ground-based station is shown in Figure 5.4f, g, and h. The sudden increase resulting from the combination of a positive preliminary impulse and the main impulse dominates at all magnetic latitude before the 11 LT. Meanwhile, the preliminary reverse impulse is observed for the first time in the 11-13 LT sector. In Figure 5.4g, it is observed how the signal arrives first at high-latitudes and later at sub-auroral and mid-latitudes stations. We consider that two factors contribute to these observations, the first is that stations mapping the outer magnetosphere will observe the signals arriving earlier because in this region the Alfvén propagation speed is faster than in the region immediately inside the plasmasphere, but also the shocks that hit near the equator will generate

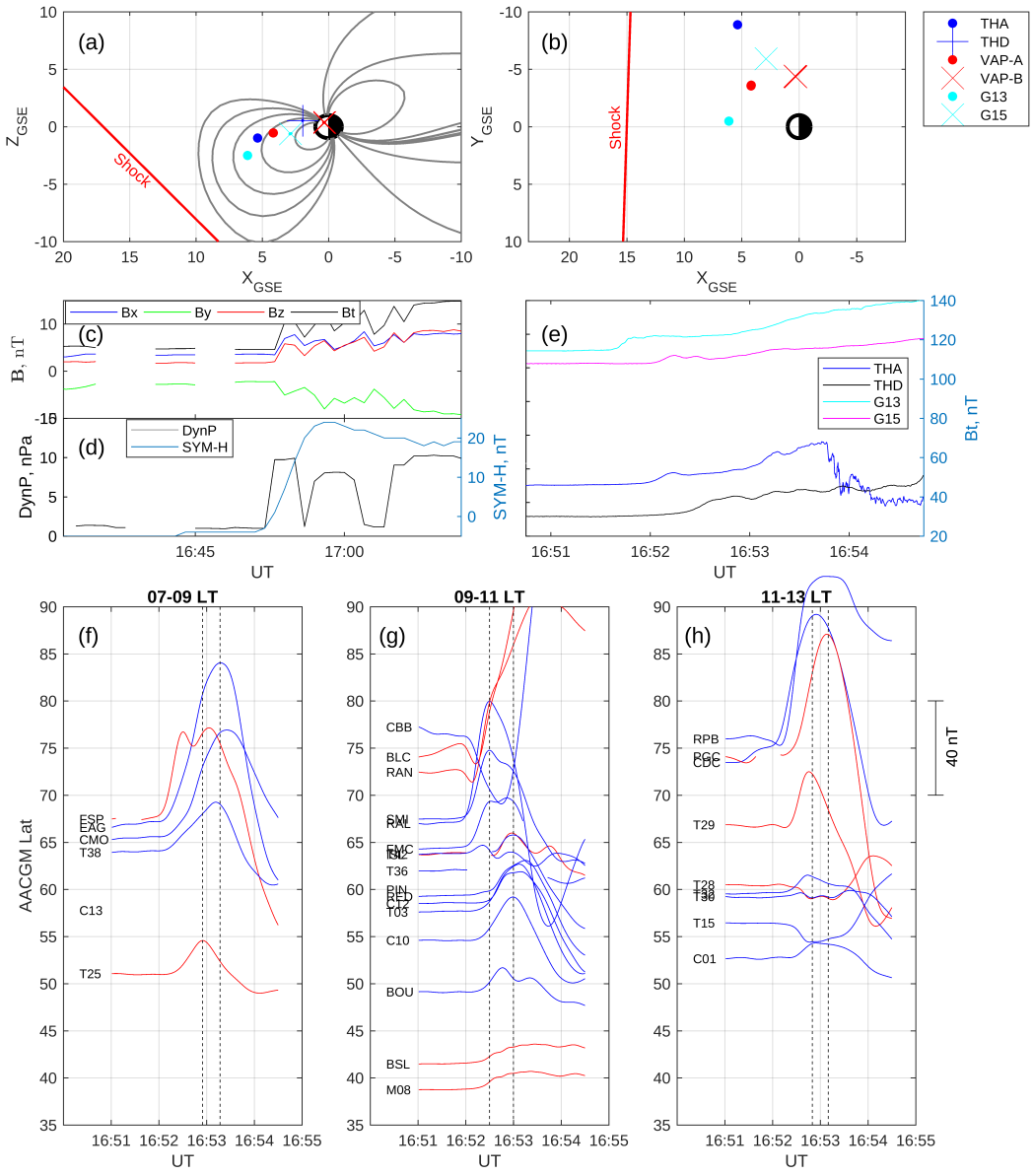

Figure 5.4: Event N°10. June 7, 2014. (a) Spacecraft location in XZ plane, reference magnetosphere computed with T89 mode. (b) XY plane. (c) IMF, (d) Left y-axis: Dynamic pressure; right y-axis: SYM-H index. (e) Left y-axis: Total magnetic field field for THEMIS-A and THEMIS-D; right y-axis: RBSP-A, GOES-13, GOES-15. (f-g-h) H-component ground-based magnetometers in the northern hemisphere and three local times. In blue the stations with a local time before the middle of the interval, in red the stations with a local time after the middle of the interval.

fast mode waves that propagate slower than the Alfvén waves following the field path line to higher latitude stations.

The shock observation made by WIND suggests that the shock hit the magnetosphere south of the equator, and near noon. The multi-spacecraft timing confirms the observations of WIND about the inclination of the shock impacting the magnetosphere south of the equator. However, the ground-based observations clearly show the perturbation arrived first at sub-auroral latitudes and later at mid-latitudes (see Figure 5.4e).

5.5 Results

From the 12 events analyzed in this chapter, six of them the shock impacted north of the magnetic equator. In these events, the sum of the preliminary impulse and the main impulse reach its maximum first at mid-latitudes and later at sub-auroral latitudes. Event N°2 shown in Figure 5.3 is an example of these types of events. In four events, the shock impacted at the magnetic equator or slightly south of the magnetic equator. Event N°10 shown in Figure 5.4 is an example of these types of events. In one of these events the preliminary reverse impulse was observed to arrive first at mid-latitudes than at higher latitudes. In the other three events, the disturbance arrives first at auroral latitudes, then at sub-auroral latitudes, and finally to mid-latitudes. Finally, in two events, the data shows the shock is impacting the magnetosphere at very high latitudes in the southern hemisphere (below -85°). In these events there is no observed pattern for the arrival of the disturbance.

All the events occurred during positive Bz and $\frac{\Delta P}{P} \geq 0.9$. The IMF positive Bz conditions are more common during quiet solar wind, which implies lower magnetospheric convection and in general stable magnetospheric conditions, including the plasma mass density radial profile. Under these conditions the decrease of the influence of equatorial magnetic reconnection on the dayside magnetopause allows a

better observation of the traveling disturbances generated by the shock compression. In this context, the results suggest that the inclination of the shock in the XZ plane affects how the ground-based magnetometers observe the disturbances, but this connection is not always observed as the Tamao's hydromagnetic model does not consider inhomogeneities in the magnetosphere, especially in the plasmapause, but helps to support the basis of magnetoseismology.

5.6 Discussion

The impact of shock angle on the propagation of MHD waves through the Earth's magnetosphere has been studied in a number of papers (e.g., (*Oliveira and Raeder*, 2015)). However, most of those studies only cover the shock inclination in the XY plane. (*Xu et al.*, 2020) compares the shock angle in the XZ plane with the time the dB/dt function is observed in stations at similar latitudes, but in opposite hemisphere. In this chapter we focus on the shock inclination relative to the dayside magnetosphere in the XZ plane, and the arrival time of stations located at different latitudes and local times of the northern hemisphere.

In the cases where the shock impacts the magnetosphere at mid-latitudes the explanation is straightforward from Tamao's theory. The disturbance travels first as a fast mode wave and then transforms into Alfvén waves that follow a shorter path line for mid-latitudes stations than for sub-auroral latitude stations. In the cases the shock impacts first near the equator, the disturbance arrives first at higher latitudes. This situation is harder to explain, as the Alfvén speed variation with latitude, L-shell and station location may play an important factor. When the shock first impact in the opposite hemisphere, the Alfvén waves generated have to travel through the equatorial magnetic field where the speed is slower, then the resulting disturbance generated north of the equator travels faster and reach the stations first at auroral latitudes, then sub-auroral and finally mid-latitudes.

In this study we did not focus on the onset of the fluctuations observed by the ground-based stations, since in many cases it is almost impossible to determine the true onset of a fluctuation. However, it is important to notice that in Event 2 (Figure 5.3), and Event 10 (Figure 5.4), the time difference between low latitude and sub-auroral latitude of the onset fluctuation generated by the shock is around 15 seconds. This is in contradiction with the theory that the PRI propagates through a Earth-ionosphere waveguide (*Kikuchi and Araki*, 1979a,b; *Araki*, 1994), in which case the propagation would be almost instantaneous.

The findings of this study are that the inclination of the shock in the XZ and the season of the year are equally important to the inclination in the XY plane when studying the propagation of Alfvén waves from the magnetopause to the Earth's surface. Subsequently, understanding the propagation of Alfvén wave through ground-based stations and how to differentiate it from the compressional fast-mode is essential for the remote sensing of the magnetosphere. *Chi and Russell* (2005) successfully showed the density distribution can be estimated using Tamao's time, the addition of the shock inclination effect in the time would improve the quality of such estimations.

5.7 Conclusion

This study reviewed 12 shocks impacting the Earth's magnetosphere with different angles, during Northward IMF Bz intervals. The CfA database provided information from the shocks, the HSO provided data from inside the magnetosphere, and SuperMag and Intermagnet provided the ground-based magnetometer observations.

We found that the inclination of the shock relative to the dayside magnetosphere must be considered as a factor of the preliminary impulse arrival delay observed at different latitudes. In effect, the addition of the shock inclination to future analysis should significantly improve the quality remote imaging of the magnetosphere performed from ground-based magnetometers.

Simultaneously, ground-based observations can be used to infer the characteristics of the shocks that generated SSCs/SIs. Eventually, with an appropriate global network of magnetometers and understanding of the magnetosphere, shock information can be extracted from ground-based magnetometers. Indeed, similar studies would benefit from 1 second resolution arrays of ground-based magnetometers located in South America and the Antarctic Peninsula that are not available in SuperMag or Intermagnet databases.

CHAPTER VI

Remote Sensing of the Equatorial Density by Travel-Time Propagation of the Preliminary Reverse Impulse

6.1 Introduction

In the previous chapter we explored the effects of interplanetary shock inclination relative to the dayside magnetosphere on the travel time of the preliminary impulse. In this chapter we study a single event with radially distributed spacecraft and ground-based magnetometers stations that allow the tracking of magnetic disturbances from the magnetopause to ground. During this event there are several latitudinally arranged ground-based stations in the afternoon sector, two spacecraft located in the noon sector, and four in the afternoon sector. This event has several similarities with the event studied by *Chi and Russell* (2005). Both events occurred close to the equinox, and during northward IMF conditions. The major difference between these two events is the inclination of the shock relative to the dayside magnetosphere. In the event reported by *Chi and Russell* (2005) the shock impinges the magnetosphere 19.9° above the magnetic equator while in the event analyzed in this chapter the shock impacted at the magnetic equator (see Table 5.1). The convenient distribution of space and ground-based observations during an interplanetary shock

event provides information about the propagation of energy and waves in the dayside magnetosphere.

The plasmasphere is the inner region of the magnetosphere, it has a toroidal shape around Earth and extends from the ionosphere until approximately 2 - 7 Re (*Carpenter and Anderson*, 1992; *O'Brien and Moldwin*, 2003; *Spasojević et al.*, 2003). The plasma density in this region is typically from ionospheric origin and decreases with altitude. The plasmasphere often has a sharp boundary called the plasmapause where the electron density decreases a factor of five to over an order of magnitude (*Carpenter*, 1963; *Moldwin et al.*, 2002). A popular explanation for the existence of the plasmapause is the result of the combination of the corotation and magnetospheric convection, and plasma refilling processes. The plasmasphere corotates with the Earth and the flux tubes inside of it are continuously refilled with ionospheric plasma, meanwhile in the outer magnetosphere, magnetospheric convection drains the plasma towards the magnetopause, generating a region with a significantly lower plasma density (*Goldstein*, 2006).

Previous studies have obtained values for the magnetospheric electron density. The Imager for Magnetopause-to-Aurora Global Exploration (IMAGE) spacecraft used Extreme Ultraviolet (EUV) instrument to remotely sense images of the plasmasphere, and also the Radio Plasma Imager (RPI) to measure the electron density in situ plasma wave observations (*Burch*, 2000; *Goldstein et al.*, 2003; *Ozhogin et al.*, 2012). Similarly, THEMIS and the Van Allen Probes also performed in situ measurements of the electron density (*Kurth et al.*, 2015; *Kwon et al.*, 2015; *Liu et al.*, 2015). However, the spacecraft potential restrains the capabilities of the instrumentation to measure low energy ions that make up the majority of the plasmasphere and that are essential to estimate the plasma mass density (*Nosé et al.*, 2020; *Menk and Waters*, 2013). In order to compute the plasma mass density, remote sensing techniques have been developed based in the properties of ULF waves (*Berube et al.*, 2003, 2005;

Chi and Russell, 2005; *Menk and Waters*, 2013; *Vellante and Förster*, 2006). These techniques are often referred to as magnetoseismic techniques because they are able to remotely map the plasma mass density in the magnetosphere similarly to how earthquakes are used to study the Earth's interior structure.

When an interplanetary shock impacts the magnetopause, it creates a compressional disturbance that propagates through the fast mode wave that loses energy at a $1/r$ rate while it couples with the Alfvén mode wave that propagates without energy loss along the L-shells. The Tamao Travel Time corresponds to the total time taken by a magnetic disturbance in the magnetopause to reach the Earth's surface (*Chi et al.*, 2001, 2006). Initially, the disturbance travels in all directions through the fast mode. Nevertheless, the wave that follows the shortest path will conserve most of the energy before coupling with the Alfvén mode waves that propagate without energy loss. After the fast mode disturbance couples with the Alfvén mode, the disturbance travels along the magnetic field until it reaches the Earth's surface. The most efficient energy transfer from the magnetopause to any ground-based magnetometer station follows this path. Under the assumptions of the hydromagnetic wave propagation model of Tamao, the travel time of the disturbance between the magnetopause and ground-based observations of the preliminary impulse depends mainly on the field line length, the magnetic field strength, and the plasma mass density of the path taken by the magnetic perturbation between the magnetopause and ground.

Since the magnetic field strength and path length taken by the disturbance can be estimated using numerical models for the magnetic field, the time from the source of the disturbance and the ground-based magnetometers provides information about the plasma density along the path. Direct and remote observations have shown the electron density has a sharp drop at the plasmapause (*Carpenter*, 1963). This density profile has been observed by multiple techniques and instruments: *Moldwin et al.* (2002) analyzed 1000 orbits of the Combined Release and Radiation Effects (CRRES)

finding that nearly 73% of the plasmapause crossings show sharp decrease in electron density outside the plasmapause, *Carpenter and Anderson* (1992) used ISEE-1 spacecraft to develop an empirical model of equatorial density in the magnetopshere, which also observes different types of profiles including the sharp decreases in electron density. However, a significant fraction of CRRES orbits analyzed by *Moldwin et al.* (2002), and IMAGE RPI observations analyzed by *Tu et al.* (2007) showed smoother density transitions between the plasmasphere and outer magnetosphere. Similar observations have been made in other studies (*Carpenter and Anderson*, 1992; *Chappell*, 1972; *Tu et al.*, 2006). *Chen et al.* (2012) modeled the properties of plasmaspheric hiss and analyzed its dependence on the plasma distribution. Their model provides (among other values) the equatorial plasma density for different plasmapause inner locations and also plasmapause thicknesses. Their results show that multiple radial density profiles are possible, in addition to the sharply decreasing density profile including smoother profiles suggesting a "thick" plasmapause.

The assumption of quasi-neutrality of the magnetospheric plasma allows the estimation of the ion number density, but not the plasma mass density. This means the composition and distribution of ions in the magnetosphere are essential to determine the plasma mass density distribution. Early experiments have shown the most abundant ions in the plasmasphere are hydrogen, helium, and atomic oxygen ions (*Shelley*, 1979). The first observations of thermal ions were made by the Dynamic Explorer (DE) 1 satellite and reported by *Chappell* (1982), suggesting the existence of a torus of O^+. The DE satellite also showed the presence of H^+ and He^+ inside the plasmasphere. The importance of the O^+ torus is its mass being 16 times heavier than the H^+, leading to the plasma mass radial profile being different than the electron density radial profile in order to keep the quasi-neutrality of the plasma. The O^+ torus has an important impact in the plasma mass distribution considering that it has been observed at all local times, with enhancement ratios up to 100 (*Goldstein*

et al., 2018). In effect, the radial distribution of the O^+ and to a more minor level the He^+ distribution are an important factor in the radial plasma mass profile in the magnetosphere.

In this chapter we use the arrival time of the preliminary impulse to ground-based stations, RBSP-A electron density and ion rates, and GOES-15 magnetic field observations to estimate the radial profile of the plasma mass density. We compare the results with simultaneous observations of electron density made by RBSP-B and THEMIS-A. The event is compared with another RBSP plasmapause crossing where density of the O^+ torus is higher and the preliminary impulse arrives first at higher latitudes.

6.2 Data and Methodology

The event analyzed in this chapter was selected from the catalogue of events of dynamic pressure pulses during northward IMF conditions built in Chapter IV. The event occurred on September 6, 2017 at 23:44 UT. The details concerning the data such as their source and format are available in Chapter II.

The spacecraft observations used to compute the mass density profile are obtained from RBSP-A and GOES-15 spacecraft. RBSPs spacecraft measure the electron number density using the EMFISIS instrument (*Kletzing et al.*, 2013). Since in the magnetosphere we can assume quasi-neutrality, the ion number density is similar to the electron number density. However, the magnetospheric ion composition is not homogeneous, and besides hydrogen ions there are also heavier ions. These ions are mainly helium and atomic oxygen. The HOPE mass spectrometer from RBSP spacecraft measures electrons and ions between 1 eV and 50 keV (*Funsten et al.*, 2013), but the data found in the CDAWeb only consider energies above 30 eV. Due to the bulk of the plasmaspheric ions being below the spacecraft potential, HOPE cannot measure the total ion density, but is able to provide the ion ratios (*Nosé et al.*,

Spacecraft	R	X	Y	Z	L-Value	LT	MLat	MLon	B_t	Δ B_t	N_e
THD	11.5	11.5	-0.1	-1.0	-	12.0	-	-	30	27	25
THE	7.9	7.0	3.4	0.9	13.1	13.7	74.0	272.3	90	40	4.2
THA	6.9	6.5	2.4	0.3	9.0	13.4	70.5	272.7	115	32	4
G15	6.6	4.9	4.2	1.2	8.1	14.7	69.4	292.4	340	24	-
RBSP-B	5.8	5.6	1.3	0.2	6.5	12.9	66.9	267.7	172	25	9
RBSP-A	4.0	3.8	-1.0	-1.0	4.3	11.3	61.2	240.3	490	9.2	20

Table 6.1: Summarized information of spacecraft location and observations. R is the radial distance in Re; X, Y and Z are the spacecraft location in GSE coordinates in Re. L-value, Altitude Adjusted Magnetic Latitude, and Altitude Adjusted Magnetic Longitude were traced from spacecraft to ground using the T96 model. B_t is the magnetic field strength in nanoTesla, and ΔB_t is the magnetic field compression observed by every spacecraft in nanoTesla units. N_e is the electron number density in cm^{-3} units.

2020). Under the assumption that the ion ratios do not change much with energy, these values in addition to the electron number density can be used to estimate the local plasma mass density.

During this event there are six spacecraft from the Heliophysics System Observatory. The location of the spacecraft and their conjugate footprint in the northern hemisphere are shown in Table 6.1.

The time taken by the disturbance to travel from the dayside magnetopause to each one of the ground-based stations depends on the magnetic field, the length of the path taken, and the plasma density along the path. We use a piecewise plasma density profile from *Lee and Lysak* (1989) and find the best parameters that minimize the difference between the observations and the time computed using Tamao's methodology. The piecewise density profile is defined as follows:

$$\begin{aligned} \rho &= \rho_{pp} \left(\frac{L_{pp}}{r} \right)^{m_2}, \text{if } L \leq L_{pp} \\ \rho &= \rho_{mp} \left(\frac{L_{mp}}{r} \right)^{m_1}, \text{if } L > L_{pp} \end{aligned} \tag{6.1}$$

where r is the radius in Re, ρ_{mp} and ρ_{pp} are the equatorial mass plasma density

at the magnetopause, and plasmapause. L_{mp} and L_{pp} are the L-values of the magnetopause and plasmapause, respectively. The m_1 and m_2 parameters define the radial density fall-off.

The optimum parameters of the density power law are the ones that minimize the square of the difference between the observed time and the computed Tamao's time. This is achieved through minimizing the χ^2 function:

$$\chi^2 = \sum_i \left(\frac{t_{obs,i} - t_0 - t_{Tamao,i}}{\sigma_i} \right)^2 \tag{6.2}$$

where $t_{obs,i}$ is the time each station observes the preliminary impulse. t_0 is the time the compression impacts the magnetopause, $t_{Tamao,i}$ is the computed Tamao's time, and σ_i is the measurement uncertainty when determining the arrival of the preliminary reverse impulse maximum deviation, which correspond to 1 second.

The estimation of the density profile problem has more variables than equations. In order to find the best solution, it is necessary to reduce the number of variables and bound their possible values by using the spacecraft observations.

6.3 Event Description

On September 6, 2017 at 23:02 UT the WIND spacecraft $(262, 13, 11)_{GSE}$ observed a fast forward shock as described by the CfA database [1]. The solar wind conditions previous to the arrival of the shock were very quiet as shown in Figure 6.1. The IMF Bz remained positive for a period of 1 hour before the event began and the last geomagnetic storm was observed 7 days before, when the SYM-H index peaked -51 nT. After the shock impinges on the magnetosphere, the SYM-H observes an increase of nearly 30 nT. The event occurs close to equinox, and the dipole tilt computed by T96 is -4.2 °. Meanwhile, the shock inclination computed by the CfA using the RH8 method

[1] https://lweb.cfa.harvard.edu/shocks/wi_data/00735/wi_00735.html, reviewed on July, 2021.

is 2.88 ± 2.11. This means that the shock front impacted quasi-perpendicularly to the dayside magnetopause near the magnetic equator.

At 23:43:30 UT THEMIS-D is located in the dayside magnetosheath and crosses the bow shock due to the shock compression. Using WIND and THEMIS-D observations the speed of the interplanetary shock propagation is 618 km/s, which is slightly higher than the solar wind speed observed by WIND (590 km/s), the error associated to the propagation time from WIND to THEMIS-D makes impossible to assure if the solar wind increases its speed after crossing the bow shock. During this event THEMIS-A, THEMIS-E, GOES-15, RBSP-A, and RBSP-B are located in the outer dayside magnetosphere, and as expected they observe low electron density values. RBSP-A is moving outwards and crosses the plasmapause at 23:39 UT at L = 4, the electron density observed is shown in Figure 6.2a.

On ground, the magnetometer stations available are mainly located in the 15-17 LT sector, but to improve accuracy we only used stations in the 16-17 LT sector for the calculations in order to reduce the impact of longitudinal propagation. The stations are located between 40° and 70° of AACGM latitude; they all observed the preliminary reverse impulse after 23:45 UT. As explained by the hydromagnetic model, the amplitude of the preliminary inverse impulse increased with latitude, which is also in congruence with the decrease of the ΔB_t observed by the spacecraft as they are closer to the Earth (shown in Table 6.1). The arrival time of the preliminary reverse impulse monotonically increases with latitude.

We used RBSP-A and GOES-15 observations to determine the parameters of the density equation (6.1) and equation (6.2). Equation (6.1) does not require values of density and location of the magnetopause, it only requires at least one plasma density observation at a known L-value on both sides of the plasmapause. Using RBSP-A that crosses the plasmapause five minutes earlier than the event, we obtained electron density values immediately inside and outside the plasmapause. These values are used

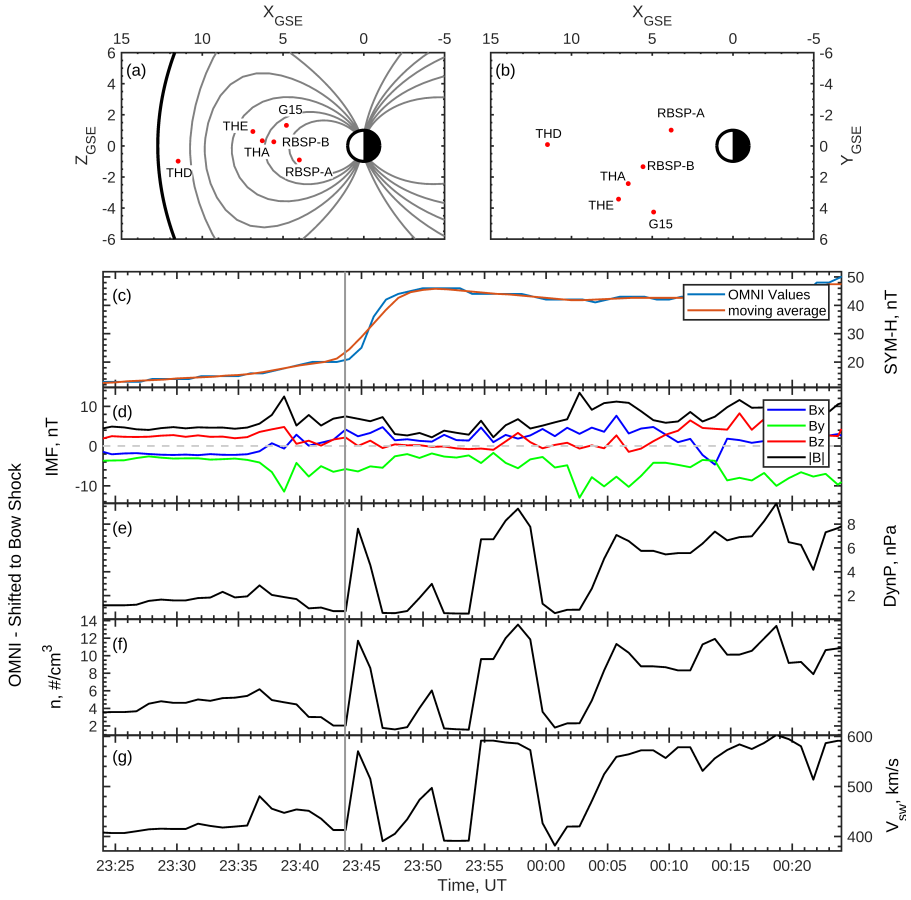

Figure 6.1: Spacecraft location and solar wind conditions. (a) Spacecraft location in the XZ plane. Magnetopause drawn as reference using *Shue et al.* (1998), and field-lines drawn using Tsyganenko T96. (b) Spacecraft location in the XY plane. (c) SYM-H index in nanoTesla. (d) IMF in nanoTesla. (e) Solar wind dynamic pressure is in nanoPascal. (f) Plasma density in cm^{-3}. (g) Solar wind flow speed in km/s.

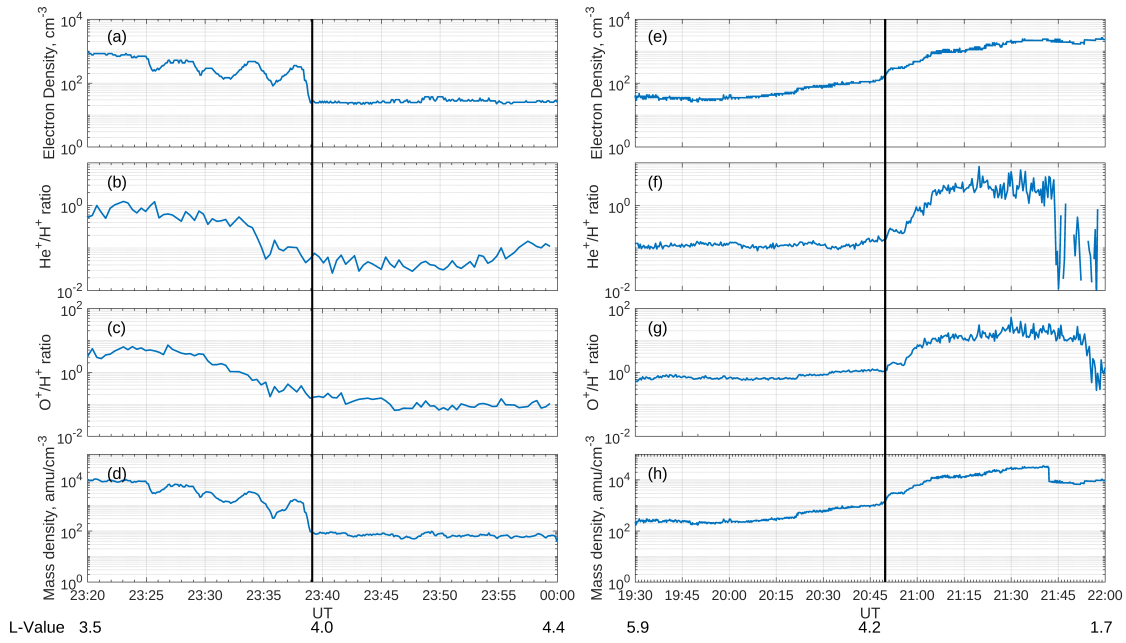

Figure 6.2: (a-d) Subplots correspond to observations made by RBSP-A magnetopause crossing while moving outwards on September 6, 2017. (a) The electron number density measured by the EMFISIS instrument. (b) He^+/H^+ observed by HOPE instrument. (c) O^+/H^+ ratios observed by HOPE instrument. (d) Plasma mass density estimated from electron number density and ion ratios when assuming quasi-neutrality. (e-h) same but for an event on January 19, 2013.

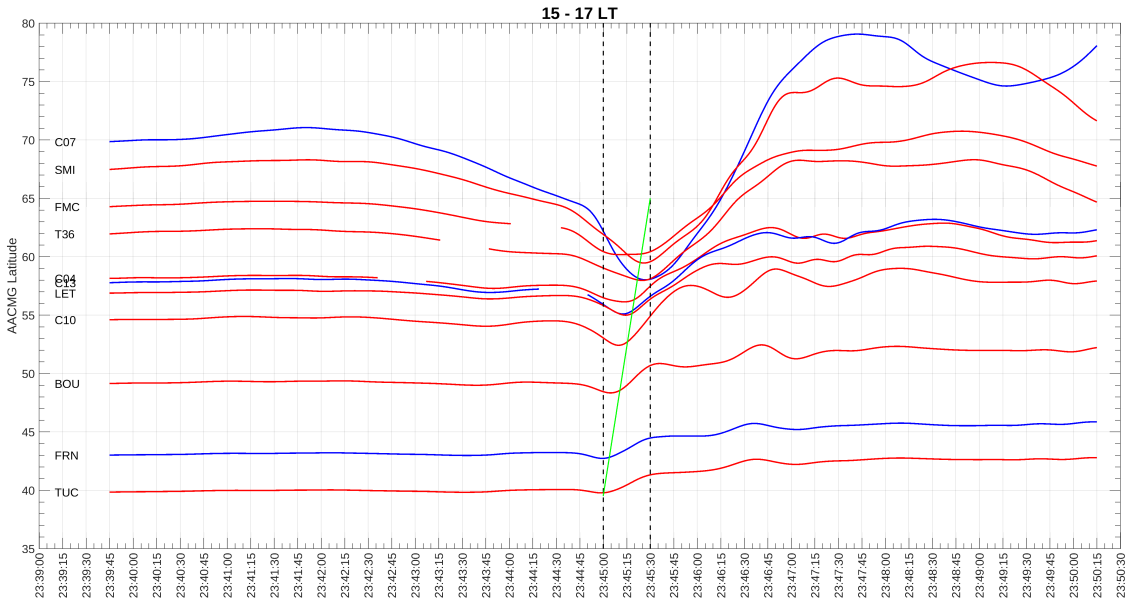

Figure 6.3: Horizontal component ground-based stations on September 6, 2017. The stations in blue are located in the 15-16 LT sector while the stations in red are located in the 16-17 LT. The green line shows the delay between the preliminary reverse impulse observed at mid latitudes and the preliminary reverse impulse observed at higher latitudes.

to reduce the number of variables from equations (6.1) and (6.2). In consequence, we can rewrite the piecewise plasma mass density function as:

$$\begin{aligned} \rho &= \rho_{pp_i} \left(\frac{L_{pp_i}}{r} \right)^{m_2}, \text{if } L \leq L_{pp} \\ \rho &= \rho_{pp_o} \left(\frac{L_{pp_o}}{r} \right)^{m_1}, \text{if } L > L_{pp} \end{aligned} \tag{6.3}$$

where ρ_{pp_i} and ρ_{pp_o} represent the mass plasma density immediately inside and outside the plasmapause boundary layer. This means the quality of this fitting is better near the plasmapause and worse near the ionosphere, and the magnetopause. Since RBSP-A measures the electron number density and not the mass plasma density that depends of the amount of He^+ and O^+, these values are estimated using the electron density and averaged ion ratios measured by HOPE instrument. Meanwhile L_{pp_i} and L_{pp_o} provide an estimation of the thickness of the plasmapause boundary layer and are easily obtained by computing the L-value of RBSP-A before and after the crossing. Since GOES-15 magnetic field conjugates very close to Fort Smith station (SMI, MLat: 67.7°, LT: 16.5) it provides a value for the Alfvén wave propagation time from the spacecraft to the station, which is helpful to calibrate the arrival time of the shock to the magnetopause (t_0, in equation 6.2) that was set at 23:43:49 UT, 19 seconds later than the first observation of the compression observed by THEMIS-D spacecraft located in the dayside magnetosheath. Using this methodology, the number of free variables is reduced to only m_1 and m_2. The number of free variables is now less than the number of ground-based stations; these parameters are estimated by solving equation (6.2).

6.4 Results

Using the methodology described, the values obtained for the mass density that best match the observed preliminary impulse arrival times are: $\rho_{pp_i} = 604\ amu/cm^3$, $\rho_{pp_o} = 167$, $L_{pp_i} = 3.9$, $L_{pp_o} = 4$, $m_1 = 5.5$ and $m_2 = 3.3$. We compare our results with the event analyzed by *Chi and Russell* (2005) because both occurred after quiet conditions and northward IMF, and in both cases the arrival of the preliminary inverse impulse is observed by ground-based magnetometers located in the afternoon sector. The m_1 value for the outer magnetosphere is larger than the value found by *Chi and Russell* (2005), but the m_2 is smaller. The plasma density profile that best adjusts to the propagation times observed is shown in Figure 6.5.

The plasma mass density immediately inside the plasmapause is 54% of the observed by *Chi and Russell* (2005), but the plasma mass density immediately outside is 2.8 times larger. Two spacecraft observations were used to verify the accuracy of the results. These two spacecraft are located in the outer magnetosphere. RBSP-B spacecraft (L-value = 6.5) observes a plasma mass density very close to the one computed using the travel time technique. THEMIS-A (L-value = 9) does not have ion composition instruments so the ratios used are an extrapolation of the ratios observed by RBSP-B. Naturally, the error generated can be large, but still inside acceptable ranges between the observations and the computed plasma mass density.

The plasma mass density difference between both sides of the plasmapause boundary layer is smaller than observed by *Chi and Russell* (2005). As consequence, the magnetic field and path length dominates over the plasma mass density in the determination of the travel time taken by the disturbance between the magnetopause and the ground-based stations. While plasma mass density inhomogeneities can explain differences in the travel-time of the preliminary impulse, the systemic response over latitude suggest the smaller density gap observed in the event of September 6, 2017 is the main reason the preliminary impulse arrives first at ground-based magnetometers

Station	MLat	LT	PRI Arrival (UT)
TUC	39.8	16.6	23:45:00
BOU	49.1	17.0	23:45:07
C10	54.9	16.4	23:45:11
LET	57.2	16.5	23:45:16
C06	60.9	16.5	23:45:24
SMI	67.7	16.5	23:45:28
YKC	69.5	16.4	23:45:33

Table 6.2: Arrival time of the preliminary reverse impulse to ground-based magnetometer stations in the 16-17 LT interval.

at lower latitudes and later at higher latitudes.

The difference between the preliminary reverse impulse observed by the ground-based magnetometer stations and the computed by magnetoseismology is shown in Figure 6.4. The preliminary reverse impulse observed by the ground-based stations is shown in Table 6.2.

In order to put these results in context, we compared with event n°4 from Table 5.1. In this event HOPE and EMFISIS instruments are operating, and also there are ground-based stations at L-values above and below the plasmapause, but there are no spacecraft observations conjugate to ground-based magnetometers that would allow the estimate of t_0. The event corresponds to the disturbance generated by an interplanetary shock at 20:49 UT on January 19, 2013. For this event, there is a complete array of ground-based magnetometer stations located at 09-11 LT sector. Figure 6.6 shows the horizontal magnetic field component for 09-11 LT sector. The stations observe the preliminary impulse to arrive first to stations that correspond to L-shells located in the outer magnetosphere and later to stations that correspond to L-shells located inside the plasmasphere.

We use EMFISIS to find RBSP's plasmapause crossings in the nearby hours to the event and observe the O^+/H^+ ratio at the same instant. At 20:49 UT the spacecraft made an inbound crossing into the plasmasphere. Figure 6.2e shows the electron density measured by RBSP-A (L=4.2, LT=13.4) which observes the crossing as a

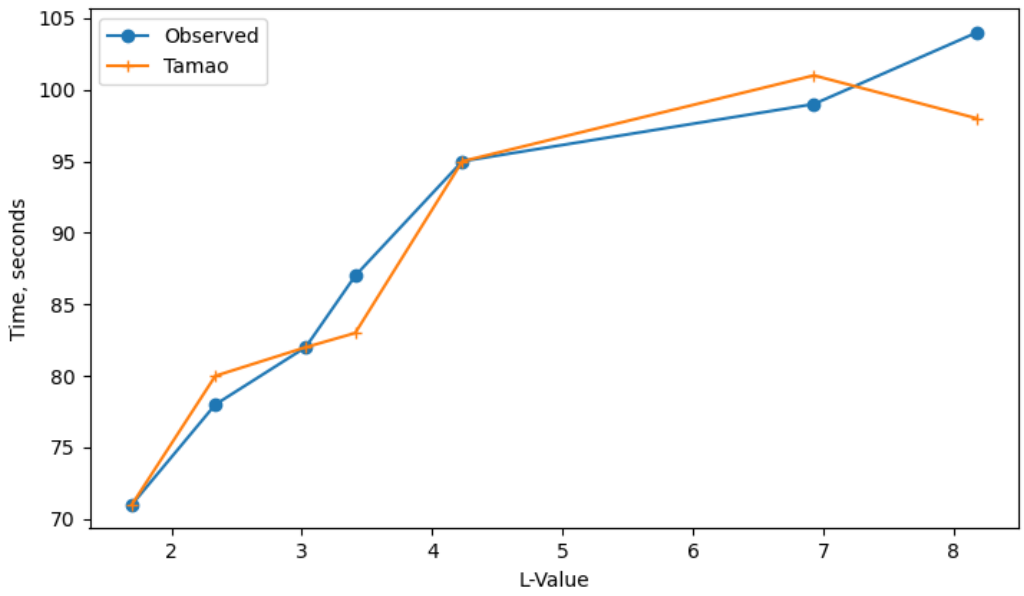

Figure 6.4: (Blue) observed preliminary reverse impulse arrival time to the ground-based magnetometer stations after the shock impacts the magnetopause. (Orange) estimated Tamao's travel time of preliminary reverse impulse arrival time to the ground-based magnetometer stations. In both cases only stations in the 16-17 LT interval are considered.

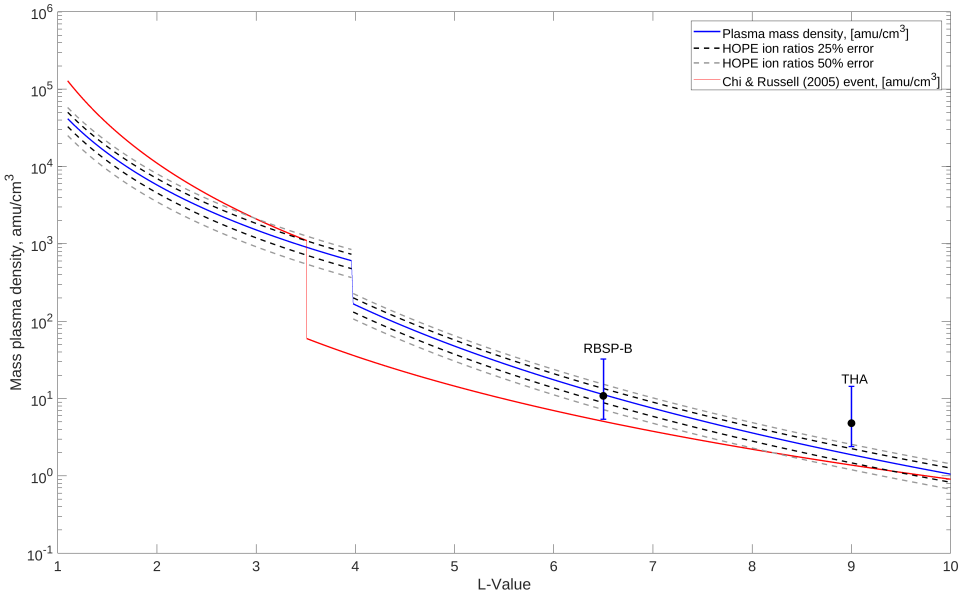

Figure 6.5: (Blue) Plasma mass density computed using RBSP-A, and ground-based stations for this event. (Red) Plasma density profile computed by *Chi and Russell* (2005).

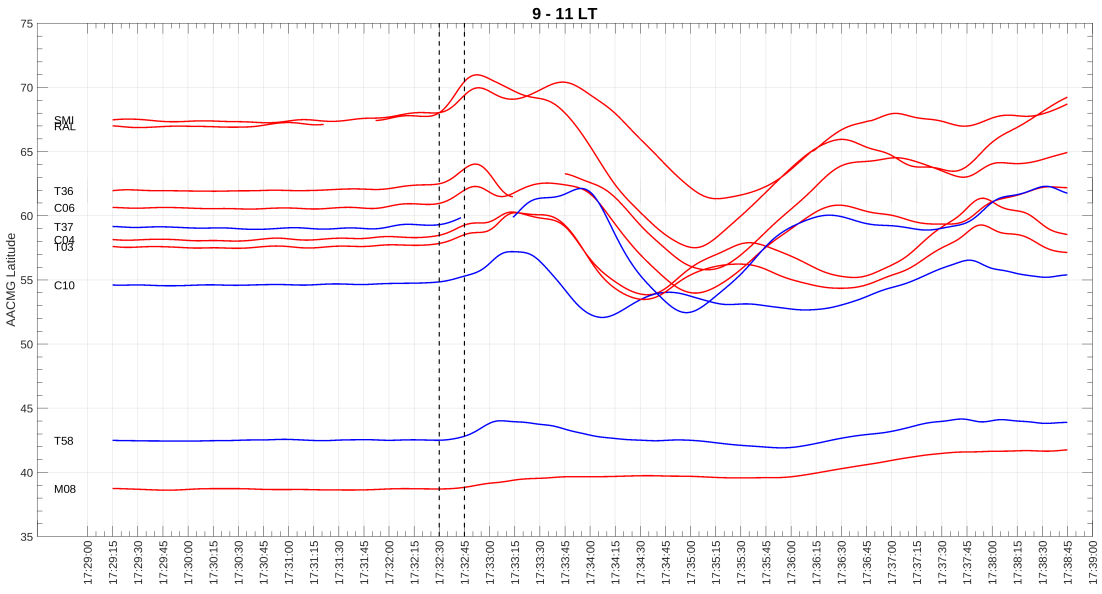

Figure 6.6: Horizontal component of magnetic field observed by ground-based magnetometers stations on January 19, 2013.

sudden increase from 40 cm^{-3} outside the plasmasphere to more than 2000 cm^{-3} inside the plasmasphere. Figure 6.2g shows the ratio O^+/H^+ at the plasmapause, these values are between 10 and 100 times larger than the observed at the plasmapause during the main event analyzed in this chapter.

6.5 Discussion

The results show that the difference between the plasma mass density inside and outside the plasmapause boundary layer is smaller than the one observed on *Chi and Russell* (2005) and the event on January 19, 2013 from our catalogue. This can explain why the preliminary reverse impulse still arrives later at ground stations that map to the outer magnetosphere than the stations that map inside the plasmasphere. The radial decrease of the mass density on the outer magnetosphere is not large enough to compensate for the decrease in the magnetic field and increase in the length of the path taken by the disturbance at larger L-shells.

The density variation is mainly modulated by He^+ and especially O^+ that has a mass 16 times larger than the H^+. For cases like this where O^+ is appreciable, the plasma mass density radial profile mainly depends on the O^+ radial distribution. The O^+ torus observed during the main and recovery phases of geomagnetic storms has an impact in the mass density distribution. This torus is not observed in the main event analyzed here, but it is observed during the mild geomagnetic activity during event n°4 of Table 5.1. *Goldstein et al.* (2018) shows that the O^+ torus density can increase by almost 2 orders of magnitude in the outer plasmasphere during or after storms.

The TCVs are generated by the MHD waves from the subsolar point in the magnetopause and are observed at high latitudes. The simulation made by *Chi et al.* (2006) shows that two other independent TCVs should develop at lower latitudes, but not observations have been made yet. However, events where the plasma mass

density drop in the plasmapause is well defined, keep open the possibility that such low latitude TCVs could actually develop.

6.6 Conclusions

We used a plasmapause crossing made by RBSP-A, magnetic observations made by GOES-15, and ground-based observations to determine the equatorial mass density profile of the dayside magnetosphere. This technique uses the electron density observations and ion ratio composition observations made by RBSP-A spacecraft as estimators for the mass plasma density. These values were used to find the parameters of a piecewise mass density function that minimized the difference of disturbance propagation time between observations and theory. The magnetic field strength and path was computed using the Tsyganenko T96 model.

The results show that the lower O^+/H^+ mass ratio is likely to be the main reason for the arrival time difference at stations above or below the plasmapause. Therefore, it is possible to estimate the ion density radial profile by observing the arrival time of the preliminary impulse at different latitudes.

These results contribute to the development of magnetoseismology techniques to study the magnetosphere. The simplicity of the hydromagnetic model with respect to more sophisticated models for the magnetospheric environment dynamics allows clear tracking of magnetic perturbations observed after an interplanetary disturbance through the magnetopause. The effective tracking of perturbations provides information about the structure of the magnetosphere that can be compared with the known solar wind conditions.

The implications of the different profiles of plasma mass density observed in the magnetosphere in the MHD wave propagation, and also the relation with the O^+ torus have been scarcely explored. Similarly, more studies are required to understand how the large or small plasma mass density drop at the plasmaspause affect the generation

of TCVs, including the possible existence of low latitudes vortices.

CHAPTER VII

Summary and Future Work

7.1 Summary

In this thesis I exploit the capabilities of the HSO to observe the dynamics of the magnetosphere after the impact of solar wind dynamic pressure pulses. First I built a catalogue of events that occurred during advantageous conditions for the study of the dynamics of the magnetosphere, which in summary are: (1) Dynamic pressure pulses; (2) northward IMF; (3) availability of spacecraft observations. In the case of Chapters V and VI, the availability of ground-based magnetometer stations was added as a condition. In Chapter IV, I analyzed the magnetospheric global response to dynamic pressure pulses using the Heliophysics System Observatory and the ground magnetometers. The methodology identified 37 events of solar wind dynamic pressure pulses during northward IMF conditions. The events were examined to study the global response of each event and identify systematic behavior of the magnetosphere due to DPPs compression, such as MHD wave propagation, sudden impulses, and Ultra Low Frequency waves in the Pc5 range. Our results confirm statistical studies with a more limited coverage that have been performed at different sectors and/or regions of the magnetosphere. In this study we presented observations of the different signatures generated in different regions that propagate through the magnetosphere. The signature of the tailward traveling DPP is observed to move at solar wind speed,

and in superposition of other known magnetospheric perturbations. It is observed that the dynamic pressure pulses also generate increases in the amplitude of Pc4-5 waves observed in the inner magnetosphere, while similar waves are observed on the ground.

In Chapter V, I studied the effects of shock inclination in the preliminary impulse propagation in the dayside magnetosphere. I used the Center for Astrophysics Shock database, and compared the shock parameters with the observations inside the magnetosphere made by the Heliophysics System Observatory, and ground-based magnetometers obtained from SuperMag and InterMagnet databases. For the first time, I demonstrated that the inclination of the shock in the XZ plane often explains the latitude time difference observed in the arrival of the preliminary impulse at ground-based magnetometers, which could be the result of the different path lengths the Alfvén waves follow when the shock impacts above or below the magnetic equator. These results are consistent with previous studies related to local time effects of arrival time of preliminary impulse in the magnetosphere due to shock inclination in the XY plane. I also found clear evidence in three of the events that even if we consider the arrival onset of the preliminary impulse as the first magnetic fluctuation, the time delay between sub-auroral and low latitude takes several seconds. This is in contradiction with the Earth-ionosphere waveguide theory that suggests an almost instantaneous propagation.

Chapter VI consist of a magnetoseismology study applied to a single case event using the Heliophysics System Observatory and ground-based magnetometers on the afternoon sector to make the most well-constrained global ion mass density estimations of the dayside magnetosphere to date. The event is also compared with data from a second event in order to contrast the observations. This demonstrates the potential of remote sensing of the magnetosphere during the era of the HSO. The results show that the propagation time of disturbances from their source at the mag-

netopause to ground provides information about the radial distribution of the plasma mass density. Specifically, the results show that the plasma mass density in the plasmasphere which is associated with the amount of O^+ is connected to the preliminary impulse arrival time between ground-based stations that are conjugated with regions inside and outside the plasmasphere.

7.2 Relevance and Future Work

The influence of the solar wind over the magnetosphere creates a complex dynamic system due to the large number of coupled processes involved which operate at multiple spatial scales (*Balikhin et al.*, 2010). *Shepherd et al.* (2002) analyzed the polar cap potential drop (PCPD) measured by Super Dual Auroral Radar Network (SuperDARN). They use the PCPD as a proxy for reconnection efficiency and found that under northward IMF the energy coupling between the solar wind and the magnetosphere is only 10%-30% of the energy coupling for southward IMF. This difference suggests the necessity of detailed studies about the mechanical (plasma flow direction $\mathbf{V}$) and electromagnetic ($\mathbf{E} \times \mathbf{B}$) energy transfer under different IMF, especially when most of the studies focus in southward IMF and make not distinction between the mechanical and electromagnetic energy inputs (*Lu et al.*, 2013). During southward IMF the magnetic flux opening during dayside magnetic reconnection is the main source of mechanical energy transfer into the magnetosphere followed by the electromagnetic energy input. Meanwhile, during northward IMF the electromagnetic energy input becomes more important than the mechanical energy transfer due to the reduced magnetic reconnection.

This thesis contributes to the study of the magnetosphere during northward IMF when the main transfer of energy between the solar wind and the magnetosphere is due to magnetic waves, which is accomplished by using magnetic field observations from the HSO. The HSO is a powerful tool for space physics exploration, as this

thesis demonstrates. However, the weak magnetic field in regions far from Earth, the fast speed of propagation of magnetic waves, and the complexity of analyzing data from different spacecraft missions presents a big challenge for global studies of magnetospheric dynamics. In this thesis I address the complexity of this problem by developing a systematic search and analysis of simultaneous observations under specific solar wind conditions. Similar studies could use a similar methodology for southward IMF conditions to study the global dynamics of the magnetosphere when magnetic reconnection dominates the transfer of energy from the solar wind into the magnetosphere. While in several cases the large amplitude of the magnetic field variations during times of high geomagnetic activity complicate the application of travel-time magnetoseismology, very large DPP events should still provide distinguishable magnetic signatures. The application of magnetoseismology techniques during southward IMF can help with the study of plasma mass density profile during southward IMF, and also to better understand the electromagnetic coupling between the solar wind and the magnetosphere.

During the last few years the availability of spacecraft and high resolution ground-based magnetometer stations have increased. Using the same methodology presented in this thesis, new events of high interest can be found providing an opportunity for new understanding in the study of energy transfer from the solar wind into the magnetosphere. For this purpose, spacecraft with both electric and magnetic field instruments can be used to determine the direction of the energy carried by the magnetic disturbance that gives origin to preliminary impulse observed at ground. Multi-spacecraft observations of the Poynting will also contribute for a better understanding of the direction of the magnetic disturbances after the impact of inclined shocks.

The amount of O^+ in the inner magnetosphere can significantly modify the propagation time of disturbances generated by DPPs. The exploration of different profiles

of O^+ in comparison with the preliminary impulse travel-time can help to understand the propagation of waves during southward IMF when the amount of O^+ is larger.

New events found using this methodology would also improve our knowledge about the capabilities of magnetoseismology. The advances on magnetoseismology are important for the space physics community. The effects of the inclination of interplanetary shock relative to the dayside magnetosphere, in addition to the behaviour of the O^+ and the plasmaspheric plume from the point of view of magnetoseismology, can eventually open the door to the remote sensing of the near interplanetary environment from ground-based magnetometer stations.

APPENDICES

APPENDIX A

Events Catalogue: Chapter IV

Table A.1: Events found between 2007 and 2018 that meet the three first criteria conditions described in the methodology section (Chapter III). IMF values are in nanoTesla and DPP speed in km/s.

Event ID	Event date	IMF By	IMF Bz	IMF Bt	DPP speed	$\frac{\Delta P}{P}$
1	2007/04/08 22:53:00	-1.1	7.8	10.4	348	1.24
2	2007/04/09 00:22:00	-8.1	11.6	14.8	371	1.22
3	2007/04/09 00:43:00	-2.3	8.7	10.0	395	1.05
4	2007/04/09 05:21:00	0.5	4.1	4.3	354	0.39
5	2007/05/18 11:35:00	10.6	6.8	16.4	493	0.28
6	2007/06/02 06:21:00	-1.8	7.9	8.2	377	2.66
7	2007/07/20 06:15:00	-2.7	9.0	11.3	349	0.33
8	2007/09/06 22:57:00	6.1	1.1	7.3	550	0.31
9	2007/09/20 10:11:00	3.6	2.9	5.0	344	2.84

Continued on next page

Table A.1 – *Continued from previous page*

10	2007/09/27 11:49:00	-0.3	1.3	3.1	408	4.03
11	2007/11/19 18:08:00	1.4	4.2	6.2	415	3.84
12	2007/12/17 02:52:00	-1.9	2.6	3.3	405	2.44
13	2008/01/04 22:48:00	-0.5	0.4	1.7	NaN	1.44
14	2009/05/20 20:25:00	1	5.8	6.7	323	1.07
15	2009/06/24 11:01:00	4.6	2.0	5.0	309	1.17
16	2009/09/03 15:52:00	-3.3	2.9	4.8	NaN	NaN
17	2009/10/24 16:49:00	-0.3	3.2	3.5	392	NaN
18	2010/04/02 07:14:00	-4	1.4	4.3	548	3.04
19	2010/04/05 11:53:00	-4.5	17.8	19.4	733	0.54
20	2010/04/05 17:43:00	-7.8	2.8	8.4	713	NaN
21	2010/04/05 17:49:00	-6.5	2.3	7.1	714	1.02
22	2010/04/11 13:02:00	NaN	NaN	NaN	449	NaN
23	2010/04/12 16:12:00	-3	4.3	5.4	435	2.6
24	2010/05/19 13:11:00	11.7	4.5	14.3	430	0.52
25	2010/07/14 21:22:00	4.3	13.4	14.1	395	0.48
26	2010/07/23 20:45:00	-4	3.7	5.5	370	0.27
27	2010/08/04 08:13:00	2.6	12.3	13.8	561	0.35
28	2011/02/18 01:31:00	0.9	4.0	5.7	448	10.64
29	2011/02/18 01:50:00	8	5.8	11.4	498	2.08
30	2011/02/18 05:58:00	19.6	16.6	29.1	560	1.65
31	2011/02/18 06:06:00	21.6	14.4	29.2	532	1.35
32	2011/04/02 21:37:00	-2.3	2.4	6.2	648	NaN
33	2011/04/18 06:53:00	4.4	2.4	5.7	375	NaN
34	2011/06/05 02:48:00	-11	14.3	18.3	549	0.42

Continued on next page

Table A.1 – *Continued from previous page*

35	2011/06/05 03:50:00	-7.7	14.6	16.5	563	0.95
36	2011/06/05 05:06:00	-2.3	16.8	17.6	528	1.23
37	2011/06/05 05:31:00	-6.6	17.5	18.7	544	2.34
38	2011/06/05 05:55:00	-6.5	15.6	16.9	544	2.77
39	2011/06/05 06:49:00	0	13.3	15.7	520	0.63
40	2011/06/05 08:13:00	9.9	10.1	14.4	522	2.22
41	2011/06/05 08:21:00	11.6	7.4	14.4	522	1.91
42	2011/06/05 08:30:00	2.4	5.8	9.9	522	1.3
43	2011/06/05 20:19:00	-4.6	2.0	5.1	594	1.14
44	2011/06/11 09:14:00	-4.5	6.0	7.6	401	2.6
45	2011/06/17 02:38:00	0.4	0.7	3.0	545	2.61
46	2011/07/31 23:57:00	-5.2	2.3	5.8	720	0.31
47	2011/08/04 21:53:00	-2.9	2.3	4.3	398	4.03
48	2011/08/05 23:32:00	-10	17.2	27.8	561	1.34
49	2011/08/05 23:52:00	-12.3	6.8	22.8	565	1.3
50	2011/09/26 13:03:00	-19.2	13.6	23.8	495	0.97
51	2011/09/29 02:34:00	7.3	5.5	10.2	570	0.22
52	2011/09/29 03:41:00	-4.6	3.7	5.9	555	5.11
53	2011/09/29 04:09:00	-6.4	3.9	7.7	535	0.56
54	2011/09/30 18:35:00	-0.4	3.7	4.7	558	11.96
55	2011/10/05 07:36:00	3.8	3.4	5.2	445	2.63
56	2011/10/05 19:59:00	1.2	9.6	11.3	447	1.97
57	2011/10/06 04:05:00	2.9	6.3	10.1	392	0.56
58	2011/10/25 02:01:00	20.3	3.8	20.7	513	1.55
59	2011/11/30 01:45:00	-3.2	5.8	6.9	458	3.26

Continued on next page

Table A.1 – *Continued from previous page*

60	2012/01/22 06:13:00	1.9	11.5	11.7	380	3.21
61	2012/01/24 15:04:00	-22	15.8	27.6	625	7.56
62	2012/03/08 11:02:00	-0.3	9.2	10.4	790	5.9
63	2012/03/09 01:04:00	0.1	10.4	11.7	748	8.19
64	2012/03/15 13:05:00	0.8	5.4	5.7	730	3.19
65	2012/04/23 03:21:00	5.8	1.3	5.9	387	4.62
66	2012/05/21 19:36:00	-0.7	1.2	1.8	388	3.16
67	2012/06/16 20:19:00	6.6	10.5	12.5	457	1.79
68	2012/06/16 21:42:00	2	27.7	28.3	520	1.11
69	2012/06/16 22:07:00	14.8	22.3	29.3	526	0.22
70	2012/06/16 23:05:00	-20.6	32.5	38.5	532	0.9
71	2012/06/16 23:41:00	12.9	34.0	37.6	506	0.94
72	2012/06/17 00:21:00	27.3	25.7	39.5	538	0.54
73	2012/06/17 00:27:00	22.8	29.2	38.1	517	0.48
74	2012/07/01 04:27:00	-3.6	1.7	5.5	652	0.11
75	2012/07/05 10:45:00	4	1.6	4.4	496	2.05
76	2012/07/05 12:10:00	3.3	2.2	4.8	480	1.12
77	2012/07/05 13:41:00	2.2	6.0	6.9	478	1.59
78	2012/07/06 22:36:00	3.4	6.8	7.6	465	9.99
79	2012/07/21 20:03:00	-0.8	6.5	7.0	520	1.8
80	2012/08/18 21:57:00	10.5	5.8	12.1	397	0.68
81	2012/09/03 23:16:00	12.8	9.2	15.8	459	0.84
82	2012/09/05 09:42:00	5.5	8.4	12.6	528	2.59
83	2012/09/20 06:22:00	-2.4	3.4	4.2	465	0.32
84	2012/11/13 09:12:00	0.2	14.4	19.3	428	0.53

Continued on next page

Table A.1 – *Continued from previous page*

85	2012/12/31 23:57:00	-0.9	0.4	2.7	353	0.12
86	2013/01/17 01:53:00	-7.8	6.4	10.2	420	0.89
87	2013/01/18 12:38:00	3.2	12.6	13.8	430	11.63
88	2013/01/18 12:46:00	-3.2	8.8	11.1	440	5.99
89	2013/01/19 00:37:00	0	4.8	4.8	438	0.71
90	2013/01/19 17:32:00	2.3	2.9	4.6	430	2.1
91	2013/02/16 12:09:00	9.4	4.0	10.2	388	1.98
92	2013/03/18 06:11:00	-1.9	5.7	8.0	572	1.57
93	2013/04/14 09:16:00	7.2	6.9	11.0	520	1.31
94	2013/04/14 09:51:00	7.7	8.8	13.5	518	0.3
95	2013/04/14 17:40:00	9.1	1.5	10.6	463	0.92
96	2013/04/15 19:33:00	-0.9	5.6	5.7	388	5.53
97	2013/05/01 08:22:00	-5.5	4.8	7.9	412	1.25
98	2013/05/16 15:52:00	2	1.1	3.5	410	1.41
99	2013/05/18 04:17:00	NaN	NaN	NaN	NaN	NaN
100	2013/05/25 21:45:00	-0.9	9.2	10.5	800	0.6
101	2013/05/26 00:33:00	-5.1	8.7	10.9	725	2.5
102	2013/05/31 23:37:00	-8.7	6.2	11.1	402	0.13
103	2013/06/01 00:33:00	-6	13.1	14.4	400	0.21
104	2013/06/08 08:22:00	0.7	3.0	3.9	440	0.73
105	2013/06/10 05:55:00	NaN	NaN	NaN	NaN	NaN
106	2013/07/09 20:51:00	5.5	8.6	10.2	415	3.41
107	2013/08/20 22:27:00	1.4	3.6	5.7	388	1.03
108	2013/10/02 04:15:00	NaN	NaN	NaN	NaN	NaN
109	2013/10/08 22:52:00	9.3	20.2	23.4	500	1.11

Continued on next page

Table A.1 – *Continued from previous page*

110	2013/10/09 04:51:00	11.6	1.7	11.8	635	0.63
111	2013/10/09 06:08:00	10.9	3.4	11.5	640	0.58
112	2013/10/09 08:25:00	10.3	6.2	12.1	585	0.32
113	2013/12/01 13:07:00	1.8	7.2	8.2	479	2.75
114	2013/12/08 01:48:00	-9.9	2.5	10.2	450	0.98
115	2013/12/13 13:22:00	-2.5	0.4	2.7	320	2.84
116	2014/01/09 20:10:00	-5.4	4.0	7.5	460	3.22
117	2014/02/07 17:05:00	5.9	6.9	10.6	NaN	NaN
118	2014/02/08 02:42:00	NaN	NaN	NaN	NaN	NaN
119	2014/02/15 22:01:00	-0.1	12.6	12.8	436	0.22
120	2014/02/16 05:27:00	-4.2	14.5	15.8	392	1.16
121	2014/03/20 10:19:00	-7.7	3.1	8.7	347	1.65
122	2014/03/29 22:56:00	-3.3	1.4	3.6	455	0.59
123	2014/04/19 18:35:00	2.6	6.1	7.7	506	0.93
124	2014/04/20 10:57:00	-0.6	8.2	8.3	554	5.7
125	2014/04/20 12:39:00	1.9	8.6	8.9	675	1.09
126	2014/05/03 17:46:00	-2.3	2.1	3.4	330	1.37
127	2014/06/07 16:52:00	-6.1	5.6	10.3	420	4.73
128	2014/06/08 06:03:00	-23.4	3.7	23.7	545	1.21
129	2014/06/08 06:54:00	-14.1	17.2	27.7	495	1.43
130	2014/06/08 07:15:00	-11.5	16.2	28.8	495	1.64
131	2014/06/08 07:31:00	-12.2	15.9	28.9	540	3.74
132	2014/06/08 09:11:00	6.7	7.0	13.2	500	0.33
133	2014/06/08 11:51:00	10.3	7.0	14.5	520	0.41
134	2014/07/03 00:41:00	-0.1	1.8	2.2	340	1.8

Continued on next page

Table A.1 – *Continued from previous page*

135	2014/07/14 14:30:00	-1.9	8.3	8.9	365	1.25
136	2014/08/31 23:57:00	4.4	1.6	6.0	448	0.33
137	2014/09/12 15:53:00	7.6	3.0	8.2	600	9.09
138	2014/09/12 18:59:00	-4.4	25.2	28.5	618	0.38
139	2014/09/13 06:11:00	NaN	NaN	NaN	NaN	NaN
140	2014/09/13 06:56:00	-10.2	15.6	29.1	670	0.19
141	2014/09/13 18:31:00	-6.7	6.5	13.3	560	0.5
142	2014/12/23 11:14:00	-11.5	3.3	13.5	410	4.72
143	2015/01/06 20:21:00	-3.8	7.7	8.6	485	1.93
144	2015/01/07 06:15:00	1.8	7.4	7.9	480	1.75
145	2015/01/07 21:08:00	-0.2	6.3	8.5	474	1.13
146	2015/02/23 17:43:00	10.4	5.9	11.9	432	NaN
147	2015/03/04 10:48:00	1.3	4.2	4.5	466	0.19
148	2015/03/16 10:43:00	-11.4	10.8	16.5	380	0.59
149	2015/03/16 17:22:00	-2.8	9.5	10.9	400	1.27
150	2015/03/17 04:44:00	10.7	15.6	19.0	551	3.49
151	2015/03/22 08:12:00	NaN	NaN	NaN	NaN	NaN
152	2015/03/22 10:04:00	3.8	2.2	6.4	695	0.71
153	2015/03/25 13:21:00	-0.8	3.4	3.5	572	2.87
154	2015/03/28 17:40:00	-3.9	8.9	10.1	423	0.61
155	2015/03/31 08:32:00	-5.8	2.1	7.2	360	2.34
156	2015/04/10 11:24:00	0.3	16.7	16.7	400	0.49
157	2015/04/10 12:33:00	10.4	9.8	14.6	417	2
158	2015/05/06 01:41:00	5.2	2.4	5.9	430	3.12
159	2015/05/06 07:19:00	-11.2	10.1	17.0	477	0.96

Continued on next page

Table A.1 – *Continued from previous page*

160	2015/06/21 16:46:00	2.1	0.8	3.4	320	3.6
161	2015/06/22 20:23:00	21.1	20.7	36.7	630	0.31
162	2015/06/22 20:32:00	15.8	26.4	35.8	620	0.15
163	2015/06/22 23:07:00	4.5	20.1	20.7	675	0.32
164	2015/06/22 23:57:00	9.6	20.6	22.8	671	0.16
165	2015/06/23 19:25:00	0.9	4.5	4.6	555	1.44
166	2015/06/25 05:29:00	-1.3	4.9	6.6	652	1.43
167	2015/06/27 02:57:00	3.2	1.8	7.5	513	2.86
168	2015/08/15 08:29:00	7.7	4.9	10.5	450	2.24
169	2015/09/08 05:49:00	NaN	NaN	NaN	NaN	0.13
170	2015/09/08 07:10:00	-15.3	7.2	19.6	528	0.18
171	2015/09/20 06:03:00	8.7	3.4	9.5	498	2.27
172	2015/11/04 03:52:00	0.8	2.6	5.4	700	2.81
173	2015/11/20 06:50:00	-4.6	2.2	5.3	382	4.57
174	2015/12/19 20:51:00	10.3	2.8	10.7	502	0.41
175	2016/01/19 10:53:00	3.7	10.3	10.9	395	1.18
176	2016/03/06 07:09:00	-3.3	10.8	11.4	365	0.38
177	2016/03/11 05:33:00	-2.4	3.3	5.6	342	1.85
178	2016/03/11 11:43:00	9.4	6.2	12.0	360	0.21
179	2016/04/17 20:03:00	-8.1	6.1	10.5	405	0.23
180	2016/06/22 20:09:00	-8.3	2.1	8.9	379	1.01
181	2016/06/22 22:02:00	0.4	4.8	11.1	400	1.28
182	2016/07/24 22:14:00	-1	7.7	7.8	NaN	0.6
183	2016/08/02 16:25:00	-1.9	14.0	14.5	430	0.92
184	2016/08/02 16:55:00	-2.6	15.0	16.5	430	0.7

Continued on next page

Table A.1 – *Continued from previous page*

185	2016/08/02 19:27:00	0.4	14.4	16.8	447	1.21
186	2016/11/09 06:43:00	NaN	NaN	NaN	NaN	NaN
187	2017/03/31 02:53:00	-3.8	1.3	4.7	687	0.16
188	2017/05/19 05:23:00	-1.8	6.2	9.8	455	1.25
189	2017/07/02 20:54:00	-2.1	3.9	6.7	435	1.12
190	2017/07/02 22:44:00	5.5	3.5	7.4	440	2.27
191	2017/07/16 06:00:00	NaN	NaN	NaN	NaN	10.77
192	2017/07/16 11:26:00	NaN	NaN	NaN	NaN	0.98
193	2017/08/04 03:33:00	-0.1	16.2	16.2	408	1.37
194	2017/08/04 05:02:00	1.8	16.8	17.0	438	0.53
195	2017/09/06 23:44:00	-3.4	2.5	4.7	590	6.92
196	2017/09/08 06:13:00	8	11.5	15.3	700	0.54
197	2017/09/11 00:15:00	NaN	NaN	NaN	NaN	NaN
198	2017/11/25 00:36:00	2.5	4.4	5.4	440	1.9

BIBLIOGRAPHY

BIBLIOGRAPHY

Ables, S. T., and B. J. Fraser (2005), Observing the open-closed boundary using cusp-latitude magnetometers, *Geophysical research letters*, *32*(10), doi: https://doi.org/10.1029/2005GL022824.

Abraham-Shrauner, B., and S. Yun (1976), Interplanetary shocks seen by ames plasma probe on pioneer 6 and 7, *Journal of Geophysical Research*, *81*(13), 2097–2102.

Allen, R., S. Livi, S. Vines, and J. Goldstein (2016), Magnetic latitude dependence of oxygen charge states in the global magnetosphere: Insights into solar wind-originating ion injection, *Journal of Geophysical Research: Space Physics*, *121*(10), 9888–9912.

Angelopoulos, V. (2009), The themis mission, in *The THEMIS mission*, pp. 5–34, Springer, doi:https://doi.org/10.1007/978-0-387-89820-9_2.

Angelopoulos, V. (2010), The artemis mission, *The ARTEMIS mission*, pp. 3–25.

Araki, T. (1977), Global structure of geomagnetic sudden commencements, *Planetary and Space Science*, *25*(4), 373–384.

Araki, T. (1994), A physical model of the geomagnetic sudden commencement, *GEOPHYSICAL MONOGRAPH-AMERICAN GEOPHYSICAL UNION*, *81*, 183–183.

Archer, M., T. Horbury, J. Eastwood, J. Weygand, and T. Yeoman (2013), Magnetospheric response to magnetosheath pressure pulses: A low-pass filter effect, *Journal of Geophysical Research: Space Physics*, *118*(9), 5454–5466, doi: https://doi.org/10.1002/jgra.50519.

Archer, M., H. Hietala, M. D. Hartinger, F. Plaschke, and V. Angelopoulos (2019), Direct observations of a surface eigenmode of the dayside magnetopause, *Nature communications*, *10*(1), 1–11.

Baker, K., and S. Wing (1989), A new magnetic coordinate system for conjugate studies at high latitudes, *Journal of Geophysical Research: Space Physics*, *94*(A7), 9139–9143.

Balikhin, M., R. Boynton, S. Billings, M. Gedalin, N. Ganushkina, D. Coca, and H. Wei (2010), Data based quest for solar wind-magnetosphere coupling function, *Geophysical Research Letters*, *37*(24).

Berchem, J., and C. Russell (1982), The thickness of the magnetopause current layer: Isee 1 and 2 observations, *Journal of Geophysical Research: Space Physics*, *87*(A4), 2108–2114.

Berube, D., M. Moldwin, and J. Weygand (2003), An automated method for the detection of field line resonance frequencies using ground magnetometer techniques, *Journal of Geophysical Research: Space Physics*, *108*(A9).

Berube, D., M. Moldwin, S. Fung, and J. Green (2005), A plasmaspheric mass density model and constraints on its heavy ion concentration, *Journal of Geophysical Research: Space Physics*, *110*(A4).

Borodkova, N., G. Zastenker, M. Riazantseva, and J. Richardson (2005), Large and sharp solar wind dynamic pressure variations as a source of geomagnetic field disturbances at the geosynchronous orbit, *Planetary and Space Science*, *53*(1-3), 25–32, doi:https://doi.org/10.1016/j.pss.2004.09.025.

Borodkova, N., J. Liu, Z. Huang, and G. Zastenker (2008), Geosynchronous magnetic field response to the large and fast solar wind dynamic pressure change, *Advances in Space Research*, *41*(8), 1220–1225, doi:https://doi.org/10.1016/j.asr.2007.05.075.

Burch, J. (2000), Image mission overview, *The IMAGE mission*, pp. 1–14.

Burch, J., T. Moore, R. Torbert, and B. Giles (2016), Magnetospheric multiscale overview and science objectives, *Space Science Reviews*, *199*(1-4), 5–21.

Carpenter, D., and R. Anderson (1992), An isee/whistler model of equatorial electron density in the magnetosphere, *Journal of Geophysical Research: Space Physics*, *97*(A2), 1097–1108.

Carpenter, D. L. (1963), Whistler evidence of a 'knee'in the magnetospheric ionization density profile, *Journal of Geophysical Research*, *68*(6), 1675–1682.

Chapman, S., and V. C. Ferraro (1930), A new theory of magnetic storms, *Nature*, *126*(3169), 129–130.

Chappell, C. (1972), Recent satellite measurements of the morphology and dynamics of the plasmasphere, *Reviews of Geophysics*, *10*(4), 951–979.

Chappell, C. (1982), Initial observations of thermal plasma composition and energetics from dynamics explorer-1, *Geophysical Research Letters*, *9*(9), 929–932.

Chen, L., J. Bortnik, W. Li, R. M. Thorne, and R. B. Horne (2012), Modeling the properties of plasmaspheric hiss: 2. dependence on the plasma density distribution, *Journal of Geophysical Research: Space Physics*, *117*(A5).

Chi, P., and C. Russell (2005), Travel-time magnetoseismology: Magnetospheric sounding by timing the tremors in space, *Geophysical research letters*, *32*(18), doi: https://doi.org/10.1029/2005GL023441.

Chi, P., D.-H. Lee, and C. Russell (2006), Tamao travel time of sudden impulses and its relationship to ionospheric convection vortices, *Journal of Geophysical Research: Space Physics*, *111*(A8).

Chi, P., et al. (2001), Propagation of the preliminary reverse impulse of sudden commencements to low latitudes, *Journal of Geophysical Research: Space Physics*, *106*(A9), 18,857–18,864, doi:https://doi.org/10.1029/2001JA900071.

Claudepierre, S., M. Hudson, W. Lotko, J. Lyon, and R. Denton (2010), Solar wind driving of magnetospheric ulf waves: Field line resonances driven by dynamic pressure fluctuations, *Journal of Geophysical Research: Space Physics*, *115*(A11), doi: https://doi.org/10.1029/2010JA015399.

Collier, M., J. Slavin, R. Lepping, K. Ogilvie, A. Szabo, H. Laakso, and S. Taguchi (1998), Multispacecraft observations of sudden impulses in the magnetotail caused by solar wind pressure discontinuities: Wind and imp 8, *Journal of Geophysical Research: Space Physics*, *103*(A8), 17,293–17,305, doi: https://doi.org/10.1029/97JA02870.

Dungey, J. W. (1961), Interplanetary magnetic field and the auroral zones, *Physical Review Letters*, *6*(2), 47, doi:https://doi.org/10.1103/PhysRevLett.6.47.

Echer, E., W. Gonzalez, A. Dal Lago, L. Vieira, F. Guarnieri, A. Gonzalez, and N. Schuch (2005), Interplanetary shocks and sudden impulses during solar maximum (2000) and solar minimum (1995–1996), *Advances in Space Research*, *36*(12), 2313–2317.

Elkington, S. R., M. K. Hudson, and A. A. Chan (1999), Acceleration of relativistic electrons via drift-resonant interaction with toroidal-mode pc-5 ulf oscillations, *Geophysical research letters*, *26*(21), 3273–3276, doi: https://doi.org/10.1029/1999GL003659.

Fairfield, D., and J. Jones (1996), Variability of the tail lobe field strength, *Journal of Geophysical Research: Space Physics*, *101*(A4), 7785–7791, doi: https://doi.org/10.1029/95JA03713.

Fox, N., and J. L. Burch (2014), *The Van allen probes mission*, Springer Science & Business Media.

Frey, S., V. Angelopoulos, M. Bester, J. Bonnell, T. Phan, and D. Rummel (2008), Orbit design for the themis mission, *Space science reviews*, *141*(1-4), 61–89.

Frey, S., V. Angelopoulos, and M. Bester (2014), Innovative themis extended mission design and implementation to achieve cross-scale magnetospheric constellation, in *Proceedings 24th International Symposium on Space Flight Dynamics–24th ISSFD, Laurel, USA*.

Funsten, H., et al. (2013), Helium, oxygen, proton, and electron (hope) mass spectrometer for the radiation belt storm probes mission, *Space Science Reviews*, *179*(1-4), 423–484.

Georgescu, E., et al. (2005), Use of edi time-of-flight data for fgm calibration check on cluster, in *Cluster and Double Star Symposium*, vol. 598.

Gjerloev, J. (2012), The supermag data processing technique, *Journal of Geophysical Research: Space Physics*, *117*(A9).

Goldstein, J. (2006), Plasmasphere response: Tutorial and review of recent imaging results, *Solar Dynamics and Its Effects on the Heliosphere and Earth*, pp. 203–216.

Goldstein, J., M. Spasojević, P. Reiff, B. Sandel, W. Forrester, D. Gallagher, and B. Reinisch (2003), Identifying the plasmapause in image euv data using image rpi in situ steep density gradients, *Journal of Geophysical Research: Space Physics*, *108*(A4).

Goldstein, J., et al. (2018), Imaging the global distribution of plasmaspheric oxygen, *Journal of Geophysical Research: Space Physics*, *123*(3), 2078–2103.

Gosling, J., G. Borrini, J. Asbridge, S. Bame, W. Feldman, and R. Hansen (1981), Coronal streamers in the solar wind at 1 au, *Journal of Geophysical Research: Space Physics*, *86*(A7), 5438–5448.

Gosling, J. T., J. Asbridge, S. Bame, and W. Feldman (1978), Solar wind stream interfaces, *Journal of Geophysical Research: Space Physics*, *83*(A4), 1401–1412.

Howe Jr, H. C., and J. H. Binsack (1972), Explorer 33 and 35 plasma observations of magnetosheath flow, *Journal of Geophysical Research*, *77*(19), 3334–3344.

Huttunen, K. E. J., J. Slavin, M. Collier, H. E. J. Koskinen, A. Szabo, E. Tanskanen, A. Balogh, E. Lucek, and H. Rème (2005), Cluster observations of sudden impulses in the magnetotail caused by interplanetary shocks and pressure increases, *Annales Geophysicae*, *23*(2), 609–624.

Kataoka, R., H. Fukunishi, L. Lanzerotti, T. Rosenberg, A. Weatherwax, M. Engebretson, and J. Watermann (2002), Traveling convection vortices induced by solar wind tangential discontinuities, *Journal of Geophysical Research: Space Physics*, *107*(A12), SMP–22, doi:https://doi.org/10.1029/2002JA009459.

Kaymaz, Z., G. L. Siscoe, J. G. Luhmann, R. P. Lepping, and C. T. Russell (1994), Interplanetary magnetic field control of magnetotail magnetic field geometry: Imp 8 observations, *Journal of Geophysical Research: Space Physics*, *99*(A6), 11,113–11,126.

Kerridge, D. (2001), Intermagnet: Worldwide near-real-time geomagnetic observatory data, in *Proceedings of the workshop on space weather, ESTEC*, vol. 34.

Kikuchi, T., and T. Araki (1979a), Transient response of uniform ionosphere and preliminary reverse impulse of geomagnetic storm sudden commencement, *Journal of Atmospheric and Terrestrial Physics*, *41*(9), 917–925.

Kikuchi, T., and T. Araki (1979b), Horizontal transmission of the polar electric field to the equator, *Journal of Atmospheric and Terrestrial Physics*, *41*(9), 927–936.

Kilpua, E., H. E. Koskinen, and T. I. Pulkkinen (2017), Coronal mass ejections and their sheath regions in interplanetary space, *Living Reviews in Solar Physics*, *14*(1), 1–83.

Kivelson, M. G., M. G. Kivelson, and C. T. Russell (1995), *Introduction to space physics*, Cambridge university press.

Kletzing, C., et al. (2013), The electric and magnetic field instrument suite and integrated science (emfisis) on rbsp, *Space Science Reviews*, *179*(1-4), 127–181.

Kokubun, S. (1983), Characteristics of storm sudden commencement at geostationary orbit, *Journal of Geophysical Research: Space Physics*, *88*(A12), 10,025–10,033.

Konik, R., L. Lanzerotti, A. Wolfe, C. Maclennan, and D. Venkatesan (1994), Cusp latitude magnetic impulse events: 2. interplanetary magnetic field and solar wind conditions, *Journal of Geophysical Research: Space Physics*, *99*(A8), 14,831–14,853, doi:https://doi.org/10.1029/93JA03241.

Koval, A., and A. Szabo (2008), Modified "rankine-hugoniot" shock fitting technique: Simultaneous solution for shock normal and speed, *Journal of Geophysical Research: Space Physics*, *113*(A10).

Kubota, Y., R. Kataoka, M. Den, T. Tanaka, T. Nagatsuma, and S. Fujita (2015), Global mhd simulation of magnetospheric response of preliminary impulse to large and sudden enhancement of the solar wind dynamic pressure, *Earth, Planets and Space*, *67*(1), 1–9.

Kurth, W., S. De Pascuale, J. Faden, C. Kletzing, G. Hospodarsky, S. Thaller, and J. Wygant (2015), Electron densities inferred from plasma wave spectra obtained by the waves instrument on van allen probes, *Journal of Geophysical Research: Space Physics*, *120*(2), 904–914.

Kwon, H.-J., K.-H. Kim, G. Jee, J.-S. Park, H. Jin, and Y. Nishimura (2015), Plasmapause location under quiet geomagnetic conditions (kp$\leq$ 1): Themis observations, *Geophysical Research Letters*, *42*(18), 7303–7310.

Lanzerotti, L., A. Wolfe, N. Trivedi, C. Maclennan, and L. Medford (1990), Magnetic impulse events at high latitudes: Magnetopause and boundary layer plasma processes, *Journal of Geophysical Research: Space Physics*, *95*(A1), 97–107, doi: https://doi.org/10.1029/JA095iA01p00097.

Lanzerotti, L., R. Konik, A. Wolfe, D. Venkatesan, and C. Maclennan (1991), Cusp latitude magnetic impulse events: 1. occurrence statistics, *Journal of Geophysical Research: Space Physics*, *96*(A8), 14,009–14,022, doi: https://doi.org/10.1029/91JA00567.

Lee, D.-H., and R. L. Lysak (1989), Magnetospheric ulf wave coupling in the dipole model: The impulsive excitation, *Journal of Geophysical Research: Space Physics*, *94*(A12), 17,097–17,103.

Lee, D.-Y., and L. Lyons (2004), Geosynchronous magnetic field response to solar wind dynamic pressure pulse, *Journal of Geophysical Research: Space Physics*, *109*(A4), doi:https://doi.org/10.1029/2003JA010076.

Lee, L., J. Kan, and S.-I. Akasofu (1982), Ring current energy injection rate and solar wind-magnetosphere energy coupling, *Planetary and Space Science*, *30*(7), 627–634.

Liu, X., W. Liu, J. Cao, H. Fu, J. Yu, and X. Li (2015), Dynamic plasmapause model based on themis measurements, *Journal of Geophysical Research: Space Physics*, *120*(12), 10–543.

Lombardi, M. A., and D. W. Hanson (2005), The goes time code service, 1974–2004: A retrospective, *Journal of research of the National Institute of Standards and Technology*, *110*(2), 79.

Lopez, R., M. Wiltberger, S. Hernandez, and J. Lyon (2004), Solar wind density control of energy transfer to the magnetosphere, *Geophysical research letters*, *31*(8).

Lu, J., H. Jing, Z. Liu, K. Kabin, and Y. Jiang (2013), Energy transfer across the magnetopause for northward and southward interplanetary magnetic fields, *Journal of Geophysical Research: Space Physics*, *118*(5), 2021–2033.

Lubchich, A., and I. Despirak (2005), Magnetohydrodynamic waves within the medium separated by the plane shock wave or rotational discontinuity, in *Annales Geophysicae*, vol. 23, pp. 1889–1908, Copernicus GmbH.

Maeda, N., S. Takasaki, H. Kawano, S. Ohtani, P. Décréau, J.-G. Trotignon, S. Solovyev, D. Baishev, and K. Yumoto (2009), Simultaneous observations of the plasma density on the same field line by the cpmn ground magnetometers and the cluster satellites, *Advances in space research*, *43*(2), 265–272.

Menk, F. W., and C. L. Waters (2013), *Magnetoseismology: Ground-based remote sensing of Earth's magnetosphere*, John Wiley & Sons.

Moldwin, M. B., and W. J. Hughes (1994), Observations of earthward and tailward propagating flux rope plasmoids: Expanding the plasmoid model of geomagnetic substorms, *Journal of Geophysical Research: Space Physics*, *99*(A1), 183–198, doi: https://doi.org/10.1029/93JA02102.

Moldwin, M. B., M. R. Collier, J. A. Slavin, and A. Szabo (2001), On the origin of reverse polarity tcrs, *Geophysical research letters*, *28*(10), 1925–1928, doi: https://doi.org/10.1029/2000GL012485.

Moldwin, M. B., L. Downward, H. Rassoul, R. Amin, and R. Anderson (2002), A new model of the location of the plasmapause: Crres results, *Journal of Geophysical Research: Space Physics*, *107*(A11), SMP–2.

Nishida, A. (1983), Imf control of the earth's magnetosphere, in *Progress in Solar-Terrestrial Physics*, pp. 185–200, Springer, doi:https://doi.org/10.1007/978-94-009-7096-0_14.

Nishida, A. (1994), The geotail mission.

Nosé, M., et al. (2020), Oxygen torus and its coincidence with emic wave in the deep inner magnetosphere: Van allen probe b and arase observations, *Earth, Planets and Space*, *72*(1), 1–17.

O'Brien, T., and M. Moldwin (2003), Empirical plasmapause models from magnetic indices, *Geophysical Research Letters*, *30*(4).

Oliveira, D., and J. Raeder (2015), Impact angle control of interplanetary shock geoeffectiveness: A statistical study, *Journal of Geophysical Research: Space Physics*, *120*(6), 4313–4323, doi:https://doi.org/10.1002/2015JA021147.

Oliveira, D., et al. (2018), Geomagnetically induced currents caused by interplanetary shocks with different impact angles and speeds, *Space Weather*, *16*(6), 636–647, doi:https://doi.org/10.1029/2018SW001880.

Ozhogin, P., J. Tu, P. Song, and B. Reinisch (2012), Field-aligned distribution of the plasmaspheric electron density: An empirical model derived from the image rpi measurements, *Journal of Geophysical Research: Space Physics*, *117*(A6).

Paschmann, G., N. Sckopke, G. Haerendel, J. Papamastorakis, S. Bame, J. Asbridge, J. Gosling, E. Hones, and E. Tech (1978), Isee plasma observations near the subsolar magnetopause, *Advances in Magnetosperic Physics with GEOS-1 and ISEE*, pp. 397–417.

Paschmann, G., et al. (1979), Plasma acceleration at the earth's magnetopause: Evidence for reconnection, *Nature*, *282*(5736), 243–246.

Peredo, M., N. Fox, and B. Thompson (1997), Overview of the istp sun-earth connection event of january 6-11 1997, in *Correlated Phenomena at the Sun, in the Heliosphere and in Geospace*, vol. 415, p. 517.

Petrinec, S., and C. Russell (1993), An empirical model of the size and shape of the near-earth magnetotail, *Geophysical research letters*, *20*(23), 2695–2698, doi: https://doi.org/10.1029/93GL02847.

Pizzo, V. (1978), A three-dimensional model of corotating streams in the solar wind, 1. theoretical foundations, *Journal of Geophysical Research: Space Physics*, *83*(A12), 5563–5572.

Rew, R., and G. Davis (1990), Netcdf: an interface for scientific data access, *IEEE computer graphics and applications*, *10*(4), 76–82, doi: https://doi.org/10.1109/38.56302.

Russell, C., and M. Ginskey (1993), Sudden impulses at low latitudes: Transient response, *Geophysical research letters*, *20*(11), 1015–1018, doi: https://doi.org/10.1029/93GL01257.

Russell, C., and M. Ginskey (1995), Sudden impulses at subauroral latitudes: Response for northward interplanetary magnetic field, *Journal of Geophysical Research: Space Physics*, *100*(A12), 23,695–23,702, doi: https://doi.org/10.1029/95JA02495.

Russell, C., M. Ginskey, and S. Petrinec (1994), Sudden impulses at low-latitude stations: Steady state response for northward interplanetary magnetic field, *Journal of Geophysical Research;(United States)*, *99*(A1), doi: https://doi.org/10.1029/93JA02288.

Sanny, J., J. Tapia, D. Sibeck, and M. Moldwin (2002), Quiet time variability of the geosynchronous magnetic field and its response to the solar wind, *Journal of Geophysical Research: Space Physics*, *107*(A12), doi: https://doi.org/10.1029/2002JA009448.

Scolini, C., et al. (2020), Cme–cme interactions as sources of cme geoeffectiveness: The formation of the complex ejecta and intense geomagnetic storm in 2017 early september, *The Astrophysical Journal Supplement Series*, *247*(1), 21, doi: https://doi.org/10.3847/1538-4365/ab6216.

Shelley, E. G. (1979), Heavy ions in the magnetosphere, *Space Science Reviews*, *23*(3), 465–497.

Shepherd, S. (2014), Altitude-adjusted corrected geomagnetic coordinates: Definition and functional approximations, *Journal of Geophysical Research: Space Physics*, *119*(9), 7501–7521.

Shepherd, S., R. Greenwald, and J. Ruohoniemi (2002), Cross polar cap potentials measured with super dual auroral radar network during quasi-steady solar wind and interplanetary magnetic field conditions, *Journal of Geophysical Research: Space Physics*, *107*(A7), SMP–5.

Shi, Y., D. M. Oliveira, D. J. Knipp, E. Zesta, T. Matsuo, and B. Anderson (2019), Effects of nearly frontal and highly inclined interplanetary shocks on high-latitude field-aligned currents (facs), *Space Weather*, *17*(12), 1659–1673.

Shue, J.-H., et al. (1998), Magnetopause location under extreme solar wind conditions, *Journal of Geophysical Research: Space Physics*, *103*(A8), 17,691–17,700, doi:https://doi.org/10.1029/98JA01103.

Sibeck, D. (1990), A model for the transient magnetospheric response to sudden solar wind dynamic pressure variations, *Journal of Geophysical Research: Space Physics*, *95*(A4), 3755–3771, doi:https://doi.org/10.1029/JA095iA04p03755.

Sibeck, D. G., R. Lopez, and E. Roelof (1991), Solar wind control of the magnetopause shape, location, and motion, *Journal of Geophysical Research: Space Physics*, *96*(A4), 5489–5495, doi:https://doi.org/10.1029/90JA02464.

Singer, H., L. Matheson, R. Grubb, A. Newman, and D. Bouwer (1996), Monitoring space weather with the goes magnetometers, in *GOES-8 and Beyond*, vol. 2812, pp. 299–308, International Society for Optics and Photonics, doi: https://doi.org/10.1117/12.254077.

Slavin, J., B. Tsurutani, E. Smith, D. Jones, and D. Sibeck (1983), Average configuration of the distant (¡ 220 re) magnetotail: Initial isee-3 magnetic field results, *Geophysical research letters*, *10*(10), 973–976.

Slavin, J., E. Tanskanen, M. Hesse, C. Owen, M. Dunlop, S. Imber, E. Lucek, A. Balogh, and K.-H. Glassmeier (2005), Cluster observations of traveling compression regions in the near-tail, *Journal of Geophysical Research: Space Physics*, *110*(A6), doi:https://doi.org/10.1029/2004JA010878.

Slinker, S., J. Fedder, W. Hughes, and J. Lyon (1999), Response of the ionosphere to a density pulse in the solar wind: Simulation of traveling convection vortices, *Geophysical research letters*, *26*(23), 3549–3552, doi: https://doi.org/10.1029/1999GL010688.

Spasojević, M., J. Goldstein, D. Carpenter, U. Inan, B. Sandel, M. Moldwin, and B. Reinisch (2003), Global response of the plasmasphere to a geomagnetic disturbance, *Journal of Geophysical Research: Space Physics*, *108*(A9).

Spence, H. E., et al. (2013), Science goals and overview of the radiation belt storm probes (rbsp) energetic particle, composition, and thermal plasma (ect) suite on nasa's van allen probes mission, *Space Science Reviews*, *179*(1-4), 311–336, doi: https://doi.org/10.1007/s11214-013-0007-5.

Szabo, A. (1994), An improved solution to the "rankine-hugoniot" problem, *Journal of Geophysical Research: Space Physics*, *99*(A8), 14,737–14,746.

Takahashi, K., and A. Y. Ukhorskiy (2007), Solar wind control of pc5 pulsation power at geosynchronous orbit, *Journal of Geophysical Research: Space Physics*, *112*(A11), doi:https://doi.org/10.1029/2007JA012483.

Takeuchi, T., C. Russell, and T. Araki (2002), Effect of the orientation of interplanetary shock on the geomagnetic sudden commencement, *Journal of Geophysical Research: Space Physics*, *107*(A12), SMP–6.

Tamao, T. (1964), The structure of three-dimensional hydromagnetic waves in a uniform cold plasma, *Journal of geomagnetism and geoelectricity*, *16*(2), 89–114, doi: https://doi.org/10.5636/jgg.16.89.

Taylor, H. E. (1969), Sudden commencement associated discontinuities in the interplanetary magnetic field observed by imp 3, *Solar Physics*, *6*(2), 320–334.

Trattner, K., J. Mulcock, S. Petrinec, and S. Fuselier (2007), Probing the boundary between antiparallel and component reconnection during southward interplanetary magnetic field conditions, *Journal of Geophysical Research: Space Physics*, *112*(A8), doi:https://doi.org/10.1029/2007JA012270.

Troitskaya, V., and O. Bolshakova (1988), Diagnostics of the magnetosphere using multipoint measurements of ulf-waves, *Advances in Space Research*, *8*(9-10), 413–425, doi:https://doi.org/10.1016/0273-1177(88)90155-X.

Tsurutani, B. T., and W. Gonzalez (1995), The efficiency of "viscous interaction" between the solar wind and the magnetosphere during intense northward imf events, *Geophysical research letters*, *22*(6), 663–666, doi: https://doi.org/10.1029/95GL00205.

Tsyganenko, N. (1987), Global quantitative models of the geomagnetic field in the cislunar magnetosphere for different disturbance levels, *Planetary and space science*, *35*(11), 1347–1358.

Tu, J., P. Song, B. W. Reinisch, J. L. Green, and X. Huang (2006), Empirical specification of field-aligned plasma density profiles for plasmasphere refilling, *Journal of Geophysical Research: Space Physics*, *111*(A6).

Tu, J., P. Song, B. W. Reinisch, and J. L. Green (2007), Smooth electron density transition from plasmasphere to the subauroral region, *Journal of Geophysical Research: Space Physics*, *112*(A5).

Usanova, M., I. Mann, J. Bortnik, L. Shao, and V. Angelopoulos (2012), Themis observations of electromagnetic ion cyclotron wave occurrence: Dependence on ae, symh, and solar wind dynamic pressure, *Journal of Geophysical Research: Space Physics*, *117*(A10), doi:https://doi.org/10.1029/2012JA018049.

Vellante, M., and M. Förster (2006), Inference of the magnetospheric plasma mass density from field line resonances: A test using a plasmasphere model, *Journal of Geophysical Research: Space Physics*, *111*(A11).

Vidal-Luengo, S., and M. Moldwin (2021), Global magnetosphere response to solar wind dynamic pressure pulses during northward imf using the heliophysics

system observatory, *Journal of Geophysical Research: Space Physics*, *126*(2), e2020JA028,587.

Viñas, A. F., and J. D. Scudder (1986), Fast and optimal solution to the "rankine-hugoniot problem", *Journal of Geophysical Research: Space Physics*, *91*(A1), 39–58.

Wanliss, J. A., and K. M. Showalter (2006), High-resolution global storm index: Dst versus sym-h, *Journal of Geophysical Research: Space Physics*, *111*(A2).

Wilson III, L., A. Koval, A. Szabo, M. Stevens, J. Kasper, C. Cattell, and V. Krasnoselskikh (2017), Revisiting the structure of low-mach number, low-beta, quasi-perpendicular shocks, *Journal of Geophysical Research: Space Physics*, *122*(9), 9115–9133.

Xu, Z., M. Hartinger, D. M. Oliveira, S. Coyle, C. Clauer, D. Weimer, and T. Edwards (2020), Interhemispheric asymmetries in the ground magnetic response to interplanetary shocks: The role of shock impact angle, *Space Weather*, *18*(3), e2019SW002,427.

Yao, L., P. Zuo, X. Feng, and Z. Liu (2010), Responses of the magnetotail plasma sheet to two interplanetary shocks: Tc-1 observations, *Chinese Science Bulletin*, *55*(6), 530–538, doi:https://doi.org/10.1007/s11434-009-0345-6.

Yu, Y., and A. Ridley (2009), The response of the magnetosphere-ionosphere system to a sudden dynamic pressure enhancement under southward imf conditions, in *Annales geophysicae: atmospheres, hydrospheres and space sciences*, 12, p. 4391, doi:https://doi.org/10.5194/angeo-27-4391-2009.

Zhang, X., et al. (2010), Ulf waves excited by negative/positive solar wind dynamic pressure impulses at geosynchronous orbit, *Journal of Geophysical Research: Space Physics*, *115*(A10), doi:https://doi.org/10.1029/2009JA015016.

Zuo, P., X. Feng, Y. Xie, Y. Wang, and X. Xu (2015), Strong solar wind dynamic pressure pulses: Interplanetary sources and their impacts on geosynchronous magnetic fields, *The Astrophysical Journal*, *812*(2), 152, doi:https://doi.org/10.1088/0004-637X/812/2/152.